Sb_2Se_3 ABSORBER LAYERED SOLAR CELL FABRICATION AND CHARACTERIZATION

A Thesis Submitted to
The Graduate School of Engineering and Science of
İzmir Institute of Technology
in Partial Fulfillment of the Requirements for the Degree of

MASTER OF SCIENCE

in Energy Engineering

by
Seher Hazal KURTULDU

December 2021
İZMİR

ACKNOWLEDGMENTS

First and foremost, I would like to express my sincere gratitude to my supervisor Prof. Dr. Gülnur AYGÜN for the perpetual support of research for her encouragement, patience, motivation, enthusiasm, immense knowledge. Her guidance helped me in all time of research and writing of this thesis and so I could not have imagined having a better supervisor and mentor for my master study. Besides my supervisor, I wish to place on records my heartfelt and sincere thanks to Prof. Dr. Lütfi ÖZYÜZER for his contributions of time and ideas to make my work productive and stimulating. His valuable suggestions, comments, and guidance encouraged me to learn more day by day. I would like to thank my Co-Supervisor Assoc. Prof. Enver TARHAN, for his valuable conversations to me.

I would like to thank the rest members of my thesis defence committee Asst. Prof. Dr. Evren ATAMAN and Asst. Prof. Dr. Fulya KÖSEOĞLU for giving suggestions and helpful comments. I would also like to thank Dr. Hasan KÖSEOĞLU for helping me with my analysis.

I also would like to acknowledge that this project is supported by the Scientific and Technological Research Council of Turkey (TUBITAK) with the project number of 118F143. Furthermore, I would like to thank Dr. Ayten CANTAS for her excellent guidance, continuous support, and understanding throughout my thesis. As a project coordinator, she helped me in every way. I am indebted to her in this sense.

I am also very thankful to my colleagues from İzmir Institute of Technology and my fellow labmates in OZYUZER Research Group members for the sleepless days.

I want to thank to my family especially my mother Reyhan Gundogan who makes my life easier with her support. I feel very lucky to have such a nice family. Thank you to my dear, intelligent, and intellectual father, I owe you a debt of gratitude. My dear brother Güney. You were there for me whenever I needed. And my beloved husband, who did his best for me. Thank you very much too. I am grateful that we had one flesh and became a family.

Last but not least, though he is not aware of those yet, I thank my little sweet son Erol Demir for the patience he showed me in the moment when I could not be with him in writing this thesis.

ABSTRACT

Sb_2Se_3 ABSORBER LAYERED SOLAR CELL FABRICATION AND CHARACTERIZATION

Thin-film antimony selenide (Sb_2Se_3) solar cells have gained attention as a high-potential photovoltaic technology around the world. Outstanding features like a high absorption coefficient, a suitable direct bandgap, and good hole mobility make Sb_2Se_3 a promising absorber material for solar cell applications. It has demonstrated a very rapid growth reaching 9.2% power conversion efficiency (PCE) in only 7 years after intensive studies. In the present thesis, first of all Sb_2Se_3 thin films were deposited on soda lime glasses (SLGs) and investigated using energy-dispersive X-ray spectroscopy (EDX), X-ray diffraction (XRD), scanning electron microscopy (SEM), spectrophotometry and Raman spectroscopy. Structural and optical studies were carried out depending on the thickness, used argon (Ar) gas flow rate and post-annealing temperature of the Sb_2Se_3 films in order to optimize the absorber layer to be used in solar cell. This study revealed that key parameters such as band gap energy and crystal structure of the Sb_2Se_3 thin films affected by the thickness, Ar gas flow rate during deposition and post-annealing temperature. In addition, oxide phase formation was also found to be related to these growth parameters. Finally, SLG/ITO/Zn(O,S)/Sb_2Se_3/Ag for superstrate configuration and both SLG/Mo/Sb_2Se_3/CdS/ITO and SLG/Mo/Sb_2Se_3/CdS/ZnS/ITO devices fabricated for substrate configuration solar cells. Since Zn(O,S)/Sb_2Se_3 heterojunction has not been studied before in the literature, this study will be the first. At the end of the electrical analysis, the best conversion efficiency of 3.9% was achieved by the solar cell with the substrate configuration.

ÖZET

Sb_2Se_3 SOĞURUCU KATMANLI GÜNEŞ HÜCRESİ ÜRETİMİ VE KARAKTERİZASYONU

İnce film antimon selenit (Sb_2Se_3) güneş hücreleri, yüksek potansiyele sahip fotovoltaik teknoloji olarak dünya çapında dikkat çekmektedir. Yüksek absorpsiyon katsayısına sahip olması, uygun bir doğrudan geçişli bant aralığına sahip olması ve yeterli düzeyde delik hareketliliğine sahip olması, Sb_2Se_3'ü güneş pili uygulamaları için umut verici bir emici malzeme yapmaktadır. Yoğun çalışmalar sonucunda, sadece 7 yıl içinde %9,2 güç dönüşüm verimliliğine ulaşan çok hızlı bir gelişme göstermiştir. Bu tezde, öncelikle soda kireç camları (SLG'ler) üzerine Sb_2Se_3 ince filmler biriktirilmiş ve enerji dağılımlı X-ışını spektroskopisi (EDX), X-ışını kırınımı (XRD), taramalı elektron mikroskobu (SEM), spektrofotometri ve Raman spektroskopisi kullanılarak incelenmiştir. Güneş hücresinde kullanılacak soğurucu katmanı optimize etmek için Sb_2Se_3 filmler film kalınlığına, büyütme sırasında kullanılan argon (Ar) gaz akış oranına ve tavlama sıcaklığına bağlı olarak yapısal ve optiksel olarak karakterize edilmiştir. Bu çalışma, Sb_2Se_3 ince filmlerin bant aralığı enerjisi ve kristal yapısı gibi anahtar parametrelerinin, film kalınlığından, büyütme sırasında kullanılan Ar gaz akış oranından ve tavlama sıcaklığından etkilendiğini ortaya koymuştur. Ayrıca oksit faz oluşumunun da bu büyütme parametreleri ile ilişkili olduğu bulunmuştur. Son olarak, altlık üstte dizilimde güneş hücresi için SLG/ITO/Zn(O,S)/Sb_2Se_3/Ag ve alttaş dizilimde güneş hücresi için hem SLG/Mo/Sb_2Se_3/CdS/ITO hem de SLG/Mo/Sb_2Se_3/CdS/ZnS/ITO cihazları üretilmiştir. Zn(O,S)/Sb_2Se_3 farklı türden eklemi literatürde daha önce çalışılmamış olduğundan bu çalışma bir ilk olacaktır. Elektriksel analizler sonucunda, %3.9'luk en iyi dönüşüm verimi, alttaş dizilimdeki güneş hücresi tarafından elde edilmiştir.

To my son…

TABLE OF CONTENTS

LIST OF FIGURES

Figure **Page**

Figure **Page**

Figure **Page**

Figure **Page**

LIST OF TABLES

Table **Page**

CHAPTER 1

INTRODUCTION

1.1. Renewable Energy Sources

Renewable energy sources are part of the Earth's natural environment and are the largest constituents of the ecosphere. Renewable energy is considered clean energy and is critically important due to its environmental-friendly nature. Main parameters of the energy consumption are the growth in economy, increase in the populations and structural changes in the world. The demand in energy rises proportionally with development of the countries. At the present time, more than 70% of the world’s energy demand is supplied by fossil fuels (fossil fuels: petroleum, natural gas, coal, etc.). They have a wide range of uses in the industrial field. However, fossil fuels contain hydrocarbons and highly carbon. Correspondingly, most of the CO_2 emission is due to the combustion of fossil fuels threatens global warming. In addition, gasoline, especially derived from petroleum, is becoming the main cause of major conflicts worldwide and regionally. For this reason, non-fossil renewable energy sources are taken into attentions in the long term support. According to IEA (International Energy Agency) the share of renewables in global electricity production reached almost 27% in 2019, even so renewable power still needs to expand. Figure 1.1. shows the projected electricity generation worldwide from 2018 to 2050, by energy source.

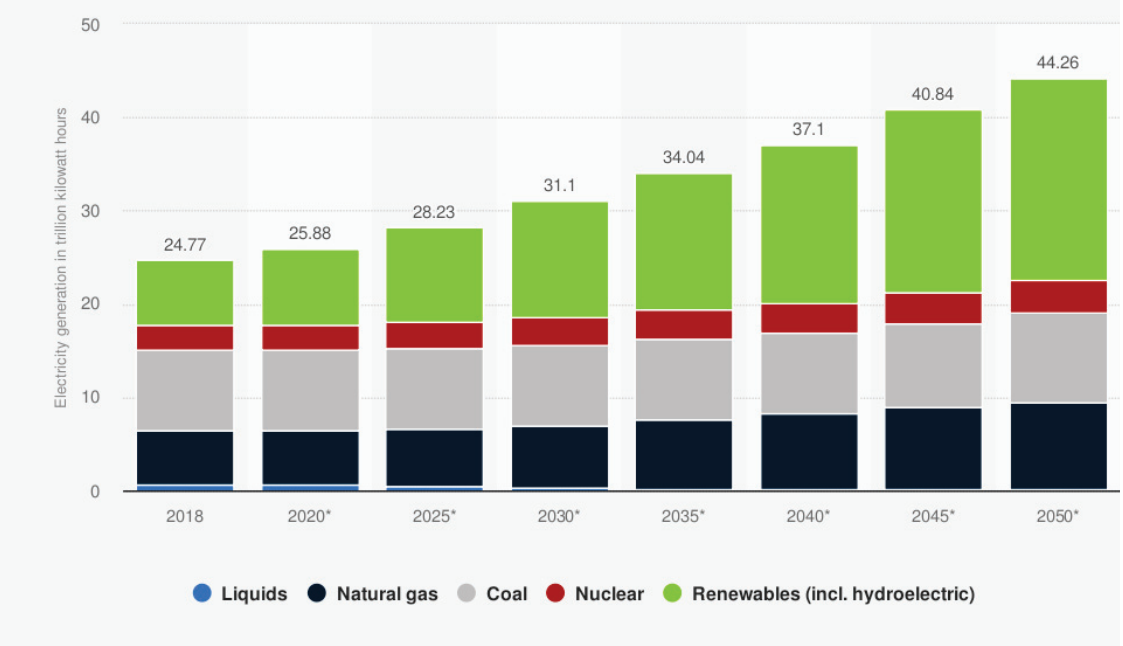

Figure 1. 1. Projected electricity generation worldwide from 2018 to 2050, by energy source (in trillion kilowatt hours)
(Source: "International Energy Outlook 2019 With Projections to 2050," 2018).

Renewable energy is produced from wind, solar, geothermal, biomass, thermal and hydropower which are the natural resources. Wind energy is generated by turbines that are installed in available places that receive wind geographically and convert the kinetic energy of the air into electrical energy. However, since it can be established windy area which is far from the city center, there is limited installation capacity. Geothermal energy can only be installed in regions where there is a geothermal resource. Therefore, it is not applicable for many regions. Biomass energy is obtained from organic wastes (animal manure, agricultural waste/residues, wastewater, energy crops, etc.) by anaerobic fermentation. It is not as clean as the others because it contains methane gas. Hydroelectric power plants supply electricity by using the height difference (potential energy) between two points where water is present. However, hydropower reservoir changes the volume, water quality and flow rate. Consequently, it destroys river systems by confining the nutrient and sediment movement in the cycle of natural life through geomorphological actions. Among these renewable energy sources, solar energy has the highest potential. It has a global potential of 1600 to 49800 exajoules (4.4×10^{14} to 1.4×10^{16} kWh) per year. Solar energy draws attention as it is an unlimited and available energy source everywhere on the planet. It is also advantageous to have large- and small-

scale applicability. On the other hand, with the development of technology, solar energy has become cost effective.

1.2. Solar Energy

Solar energy which sourced from the Sun, is heat and bright light. It is corresponding to the radiation energy released by the physical process “fusion” in the core of the Sun. The intensity of solar radiation on the surface is about 6.33 x 10^7 W/m^2 (Sabbagh 1977). The atmosphere reflects and absorbs some of this energy. Even a small portion of this energy arriving to Earth is so much more than the current energy consumption of humanity. Since ancient times humans have been utilizing from the sun for many different purposes like cooking, heating, cooling, etc. The first evidence suggests that a sunlight used to light a fire in the 7th century BC (Jha et al. 2017).

Solar energy consists of 3 technologies: photovoltaics, solar heating, and cooling, and concentrating solar power. The heat generated by the sun is used to provide space or water heating in solar heating and cooling (SHC) and concentrating solar power (CSP) applications. Among these technologies photovoltaics (PVs) generates electricity directly from the sunlight using the photoelectric effect. The most important invention was attained in 1839 with photovoltaic effect (Becquerel 1839). The photoelectric effect occurs when electromagnetic radiation, such as light, strikes a material. As a result of this collision, electrons emitted which generates photoelectrons. In this way, the photovoltaic effect occurs in solar cells.

The Sun absorbs all kinds of radiation and give out a temperature-dependent black body radiation. The spectrum looks like the blue line in Figure 1.2., which corresponds to the irradiance of the sun at 5900 K. When photons enter the atmosphere, some wavelengths are absorbed by water, oxygen, ozone, and other molecules in the atmosphere. The radiation just outside the earth’s is represented with AM0. AM means Air Mass and indicates the path length of sun light through the atmosphere which is shown in Figure 1.3.

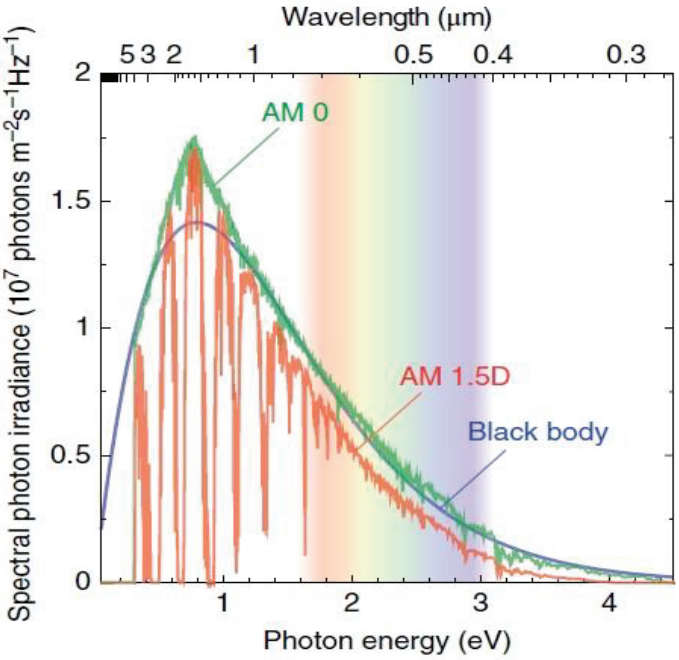

Figure 1.2. Solar Radiation
(Source: Ito 2014)

The Air Mass is described as AM=1/cos (θ), where θ is the angle between the position of sun and the zenith. AM1 represents that the radiation on earth's surface is perpendicular to incident light. The standard spectrum for measurements on solar cells is called AM1.5 (red line in Figure 1.2.), which represents angle of incidence of 48 °.

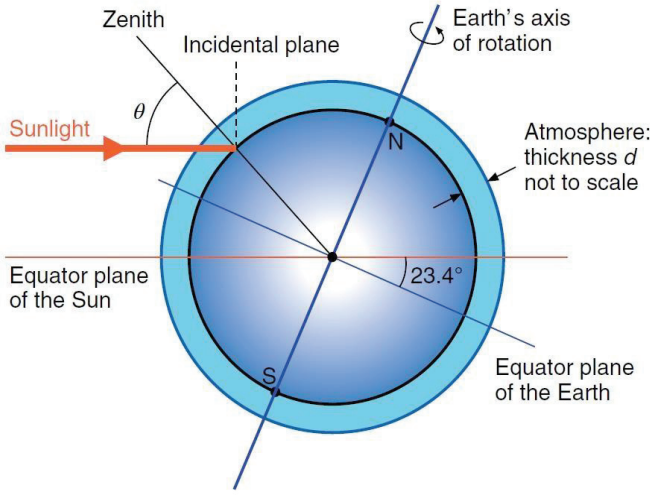

Figure 1.3. The path of sun light through the atmosphere
(Source: Ito 2014)

CHAPTER 2

THIN FILM SOLAR CELLS

2.1. Overview of Photovoltaic Technology

Photovoltaic (PV) is a technology which enables obtaining electricity from the sun through solar cells or solar panels and it is also a general name given to studies on this subject. PV technologies have several benefits in terms of electricity generation over conventional technologies. PV electricity production, for all technologies, is a zero-emission process. A single PV device is called as a cell. These cells are made of different semiconductor materials and are often thin like nanometers to micrometers.

The PV solar systems are divided into three groups based on the used semiconductor. First generation solar cells also assumed as conventionals, are the crystalline silicon (c-Si). More than 80% of the PV industry is covered by Si wafer technologies and c-Si solar cells. They exhibited power conversion efficiencies more than 25%. Until this time, the best real-world silicon solar cell developed by Kaneka Corporation and it has achieved 26.7% photo-conversion efficiency (Green et al. 2018). However, Si technology requires a thick layer to absorb more incident solar radiations since it is based on an indirect band gap absorber material. On the other side, in order to obtain highly efficient solar cell, perfect crystals are necessary, and it is an expensive process.

The second-generation solar cells are also mentioned as thin film solar cells and have attracted increasing attention as an alternative to limitations of c-Si technology. Thin film solar cells have high optical absorption coefficient and contain direct band gap materials. Also, thinner layers absorb more incident solar radiations than c-Si, therefore thin films are low-cost materials. One of the advantages is that they can be flexible, and this makes them suitable for large area applications. According to the absorber material used, there are mainly five types of inorganic solar cells which are amorphous Si (a-Si), copper indium diselenide (CIS), copper indium gallium diselenide (CIGS) cadmium telluride (CdTe), and $Cu_2ZnSnS(e)_4$ (CZTS(e)). Sb_2Se_3 has been used more recently than

others in solar cell structure. Active research on Sb_2Se_3 began in 2014. Detailed investigation of these solar cells will be given in the following section.

Novel thin film solar cells are relying on quantum dots, organic materials, hybrid and perovskite materials and they are termed ‘third generation photovoltaics. Third-generation solar cells are solution processable solar cells and have capable of large-scale solar electricity generation. Also, they have easier fabrication process rather than other two technologies. This group also includes expensive multi-junction solar cells. Their commercial applications are limited due to the high production cost and unstability. Otherwise, third generation perovskite solar cells demonstrate high potential with having efficiencies beyond 20% under the laboratory scale. However, there are some challenges about photogeneration and charge transportation in third-generation solar cells. They are more difficult to understand and needs more complex characterization techniques.

2.2. Thin Film Solar Cells

Thin film solar cells have many advantages over c-Si solar cells. Since silicon has an indirect band gap, a few hundred micrometers in thickness of wafers are necessary to obtain efficient solar cell. Much less material is consumed in thin film solar cells compared to crystalline silicon solar cells. Since the absorption coefficient of typical thin film absorber materials is about 100 times higher than crystalline silicon, 100 times thinner film material is sufficient to absorb the same amount of energy.

Another advantage of thin film solar cells is that the need for crystal quality and purity is less than crystalline silicon solar cells, which reduces the cost (J. V. Li et al. 2013). In addition, flexible materials such as metal foils or polyimides can be used as substrates for thin film applications. These flexible and light solar cells provide completely new applications. However, the use of flexible substrates for silicon cells requires heavy glass protection plates that will restrict residential applications (Kessler and Rudmann 2004).

The thin film technology has been relatively cost effective, but still have less efficiency compared to the traditional c-Si technology and have limited commercial availability. Thin film solar cells have the potential to achieve higher efficiencies than c-

Si solar cells, but this fact has not been reached, yet. For this reason, studies are continuing intensely.

2.2.1. Amorphous Si Solar Cells (a-Si)

Amorphous silicon (a-Si) solar cells are the earliest and most matured type of thin film technology. A-Si is a non-crystalline form of silicon with a direct band gap and since it has an amorphous structure, it absorbs sunlight more strongly than c-Si and poly-Si. On the other hand, a rather thin layer is sufficient to absorb sunlight. Another advantage over crystalline technology solar cells is its low cost and ability to be made at a low temperature. These solar cells have been fabricated in heterojunctions structure, p-i-n junction since thin film silicon is very functional in tandem and triple-junction solar cells like no other thin films compounds. The structure p-i-n photodiode sequence is shown in Figure 2.1.

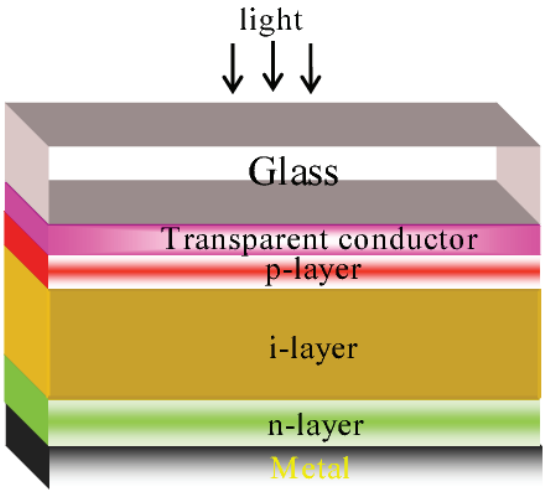

Figure 2.1. a-Si solar cell structure
(Source: Kosarian and Jelodarian 2011)

In this structure excessive electrons are transferred from the n-type material to the p-type material and leaving positively and negatively charged layers behind. Consequently, a sizable electric field created. Unfortunately, the theoretical limit for the efficiency is estimated to be approximately 15 percent (Carlson and Wronski 1976). Considering the literature, recorded highest efficiency is 14.0% for a-Si (Green et al. 2017).

2.2.2. Cadmium Telluride (CdTe) Solar Cell

Cadmium telluride (CdTe) photovoltaic solar cells describe a technology that is relying on the use of cadmium telluride as an absorber layer in solar cell structure. It is a p-type semiconductor with a direct optical band gap of approximately 1.5 eV which presents a suitable match to the distribution of photons in the solar spectrum regarding the electricity conversion. In addition, its absorption coefficient is high ($>10^5$ cm^{-1} at λ= 700 nm) in the visible region. It allows most of the photons to be absorbed in a narrow depth. A basic heterojunction design in which p-type CdTe was compatible with n-type cadmium sulfide (CdS) as shown in Figure 2.2. appears as the most used combination. To complete the cell, top and bottom contacts are added.

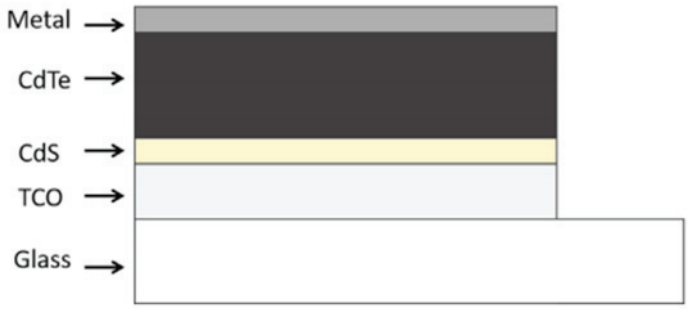

Figure 2.2. Typical CdTe solar cell structure.
(Source: Baines et al. 2018)

First Solar Company declared the highest efficiency for a laboratory CdTe solar cell as 22.1% in 2015 (Kartopu et al. 2019). However, cadmium (Cd), a toxic heavy metal considered a hazardous substance and tellurium (Te) is a rare, mildly toxic metalloid which has relatively high cost. These drawbacks limit the use of CdTe.

2.2.3. Copper Indium Gallium Diselenide (CIGS) Solar Cell

Copper indium gallium diselenide (CIGS), is another p-type semiconductor absorber layer thoroughly studied for thin film photovoltaics. It has gained considerable attention due to its favorable properties such as direct band gap (1.0 – 1.12 eV), high absorption coefficient (10^5 cm^{-1}) and less material wastage (Guillemoles 2002). Like CdTe, it can be coated on rigid as well as flexible substrates. The CIGS solar cell

efficiency of 22.8% set a world record as the highest of any thin-film technology (Ramanujam and Singh 2017). However, precise control of the film stoichiometry is difficult and due to the complicated process, CIGS module manufacturing is lagging behind other thin film modules. These are some limitations in commercialization of this material. Other obstacles are indium (In) and gallium (Ga) are expensive materials. Hence, production cost rises for large area applications.

2.2.4. Copper Zinc Tin Sulfide (CZTS) Solar Cell

CdTe and CIGS inorganic semiconductor compounds are involved in the commercial production of thin film solar cells as an absorber layer but the fact that they contain poisonous heavy metals such as Cd, In and Cd and Te elements have very high costs due to limited underground reserves, the use of these solar cells are limited. In addition, In, Cd, Te elements require high cost to become operable (Kumar et al. 2015). Considering the drawbacks, studies on other materials are focused. Copper zinc tin sulfide (CZTS) p-type semiconductor compound has low cost and contains Cu, Zn, Sn and S elements with high earth reserves and non-toxic elements. It has a direct bandgap energy range between of 1.45-1.60 eV and a high optical absorption coefficient above 10^4 cm^{-1}. Therefore, the use of CZTS thin film solar cells in the PV industry seems highly promising. Figure 2.3. shows the superstrate CZTS solar cell.

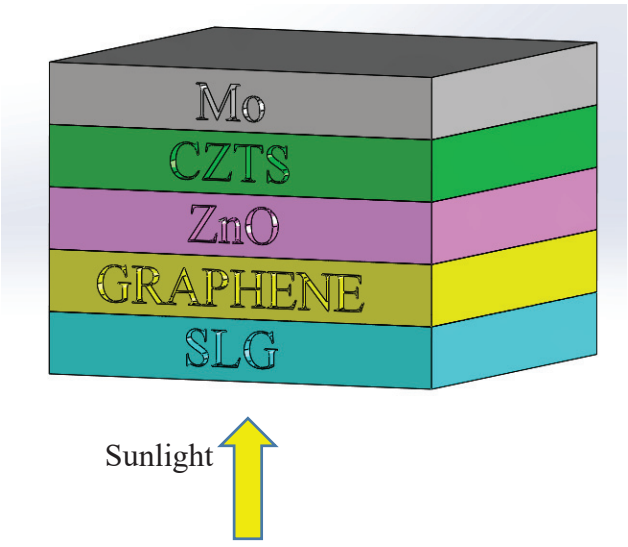

Figure 2.3. CZTS solar cell in superstrate structure.

High quality CZTS is required to be a single phase kesterite structure. However, the growth of pure kesterite phase without any secondary phase is difficult due to the low thermal stability and narrow single-phase region. Many secondary phases occur in CZTS material during the formation process and these compounds affect the performance negatively.

The world highest recorded yield for a CZTSSe (sulfoselenide) cell was assigned as 12.6% by Japanese thin film manufacturer Solar Frontier in 2013 (W. Wang et al. 2014). Barely, the highest efficiency for CZTS solar cell is 11% as of 2020 (Green et al. 2018). Removal and control of secondary phases are the significant parameters in terms of the solar cell efficiency. The yields achieved are still far from theoretical values.

Up to now, commonly used materials of solar cells were introduced. Compared to these solar cells, antimony selenide (Sb_2Se_3) is a much more recently studied material and outstands as a brilliant candidate to be used as an absorber layer in thin film PVs. It has a binary phase structure consisting of Sb and Se elements. Sb_2Se_3 gets more attention than others due to its optoelectronic properties. The detailed investigation of Sb_2Se_3 solar cell will be given in the following sections.

CHAPTER 3

FUNDAMENTALS OF SOLAR CELLS

3.1. Semiconductors

Materials are grouped with respect to their electrical properties as, semiconductors, insulators, and conductors. The difference between these materials can be explained by band theory. Figure 3.1. shows the band diagram of conductor, semiconductor, and insulator. The distance between the valance and the conduction band determines electrical properties of the material which represent the electron mobility between the bands. Semiconductors are existing in somewhere between that of a conductor and an insulator.

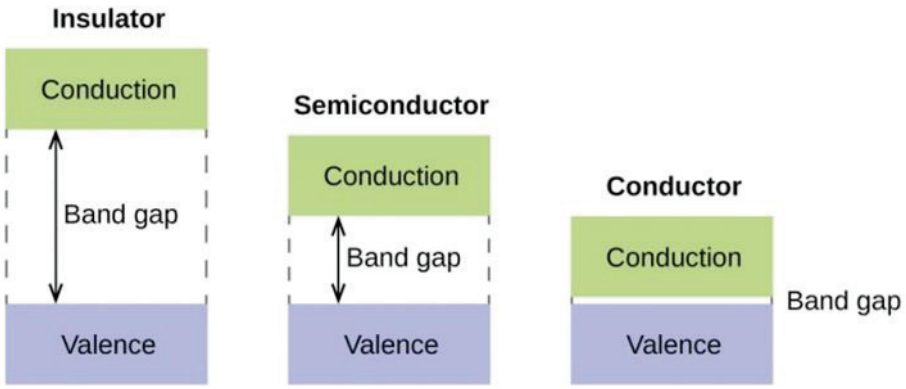

Figure 3.1. Band diagram of insulator, semiconductor and conductor.

The valence band is located lower in energy while the conduction band is higher in energy. In conductors, the valance band is mostly empty and there is no existent energy gap. Therefore, electrons easily jump to the conduction band which enables current to flow. In insulators, the valance band is mostly full and energy gap is very large (>3 eV) so, electrons can't jump from valance to the conduction energy band. There is no current flow. In semiconductors, the valance band is half full and they have a moderate energy gap (1 - 3 eV). Only a few electrons can jump to the conduction band and a little current can flow throughout the material. At absolute zero (T = 0 K) the semiconductor behaves

like a perfect insulator because the bands are either completely filled or completely empty. However, at higher temperatures, some of the electrons gain enough energy to jump on the empty conduction band. These electrons contribute to electrical conductivity while leaving vacancies or holes (considered positive) behind (Kittel 2004).

Semiconductors categorized as intrinsic and extrinsic (doped) semiconductors. An intrinsic semiconductor is a mono (single) crystal semiconductor without any other types of atoms in it. Most widely knowns are silicon and germanium elements. They belong to group IV elements in the periodic table which means that they have 4 electrons in their valence band. Figure 3.2. shows the covalent bonding structure in silicon lattice.

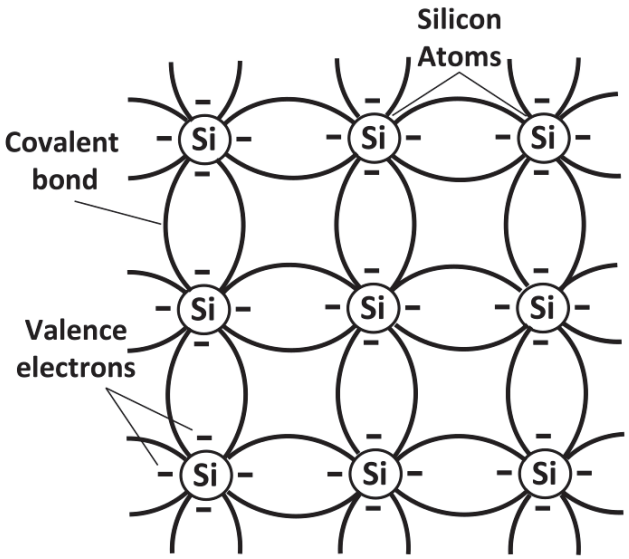

Figure 3.2. Intrinsic silicon lattice showing the covalent bonding.
(Source: Kittel 2004)

An excited electron causes a local defect in the covalent bond. This defect can be filled with an electron in the crystal, but it is empty. This space is called hole. Both electrons and holes can move in a crystalline structure. A free electron in crystalline structure can move randomly with the thermal energy it receives from the crystal. Similarly, a hole can move in the crystal. Because one of the electrons leaving the covalent bond can be replaced by one of the neighboring electrons to complete the bond. In this case, a hole is formed at the place where the last electron is discharged. Thus, the hole moves in the opposite direction with respect to the electron. The reason for this hole mobility can be

thermal stimulation in the lattice. At the same time, the holes and electrons can move within the crystal structure by reacting to the electric field, and in this case the macroscopic current flow through the crystal is increased.

Unlike elemental semiconductors such as Si and Ge, compound semiconductors also exist and commonly used in electronic applications. A compound semiconductor is comprised of chemical elements of at least two different species. These semiconductors usually form in periodic table groups III–V and II–VI. Figure 3.3. shows the important semiconductor elements in the periodic table and possible semiconductor compounds. Also, properties of notable element and binary compound semiconductors at 300 K is given in Table 3.1.

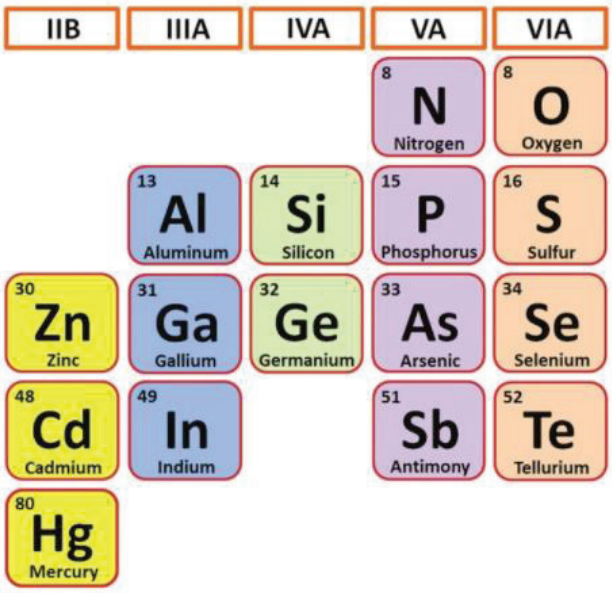

Figure 3.3. The elements in the periodic table to form possible semiconductor. (Source: Congcong Wang et al. 2014)

In an intrinsic semiconductor, the concentrations of free electrons and holes are small, therefore magnification of the current is limited. For the purpose of increasing the concentration of free electrons and holes, impurities can be added to the semiconductor. Adding impurities is called doping and an extrinsic semiconductor is one that has been doped. It can have divided into two groups as p-type and n-type dopants. These will be detailed in the next section.

Table 3. 1 Properties of Important Semiconductors (Sze and Ng 2006).

Semiconductor		Bandgap (eV)	Dielectric constant
Element	Ge	0.66	16.2
	Si	1.12	11.9
III–V	GaAs	1.42	12.4
	GaP	2.27	11.1
II–VI	CdS	2.42	5.4
	CdTe	1.56	10.2
	ZnO	4.58	9.0
IV–VI	PbS	0.41	17.0

3.1.1. P-type Semiconductors

Different from silicon, an impurity could exist either one more or one less electron in the valance shell. Thus, impurities for group IV type atoms (silicon) would stem from group III or group V elements. Group III elements are the most common acceptor impurities which have 3 valence electrons (e.g. Boron). Since boron (B) has just 3 valence electrons, the boron atom can only bond with three of its contiguous, thus leaving one open bond position. Boron accepts a valence electron, and it is designated as an acceptor impurity. Acceptor impurities bring excess holes but do not bring free electrons. Therefore, the electrons in the valence band get mobile. Holes and electrons move in opposite directions. In brief, p-type semiconductor which doped with an acceptor impurity, has excess holes. In p-type materials, holes are the majority charge carriers, while electrons are the minority charge carriers. Al, Ga and In are some of doping materials.

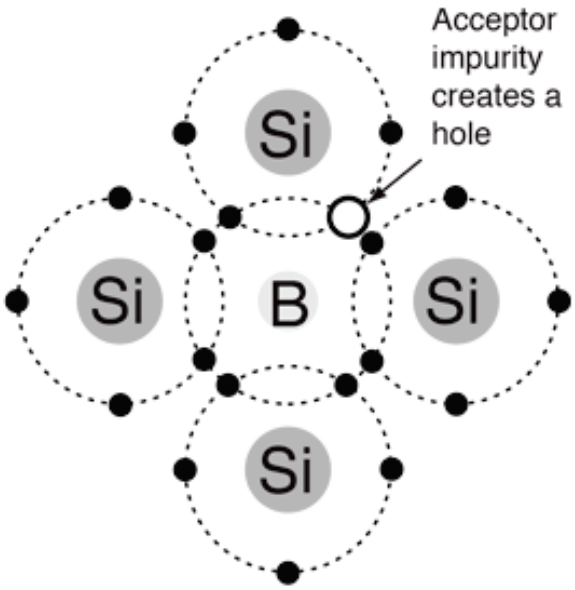

Figure 3.4. P-type semiconductor scheme.
(Source: Kittel 2004)

3.1.2. N-type Semiconductors

The main difference between the doped semiconductors is the majority charge carrier types. A semiconductor doped with donor impurities gives out free electron and is termed as an n-type semiconductor. The group VI atom is called a donor impurity since it donates a free electron. A small amount of pentavalent (e.g., arsenic, antimony) impurity is enough to form an n-type semiconductor. As shown in the Figure 3.5., if antimony (Sb) adds, this atom substitutes one silicon atom in the lattice. Sb atom has 5 valence electrons and shares its 4 electrons to form a quadratic bond with neighboring silicon atoms. At room temperature, crystal's thermal energy is sufficient to remove the weakly bound fifth electron of Sb from the electron shell of this atom. Therefore, this electron is free to move since it jumps to the conductivity band and can contribute to electrical conductivity. In n-type materials, the majority charge carriers are electrons, while the minority charge carriers are holes.

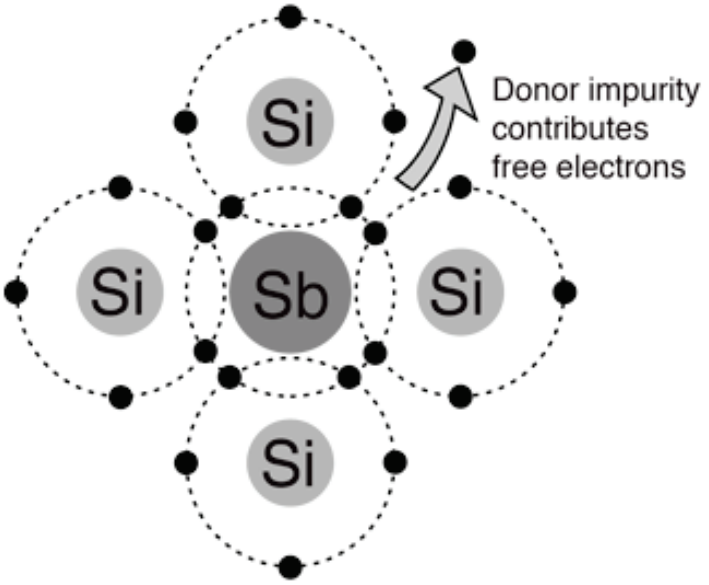

Figure 3.5. P-type semiconductor scheme.
(Source: Kittel 2004)

3.2. P-N Junction

A p-n junction is formed by the contact between a p-type semiconductor and an n-type semiconductor. If the n-type and p-type zones consist of the same type of semiconductor (i.e., n-type silicon and p-type silicon), this junction is called a homojunction. If semiconductor materials differ from each other (such as n-type silicon p-type germanium), the junction is called heterojunction. A diode is a semiconductor device formed of a single p-n junction (Figure 3.6.). It shows a non-linear current voltage (I-V) characteristic and is commonly used as a rectifier device. Some diodes can emit light (LED = light emitting diode) and some can emit laser light (laser diode).

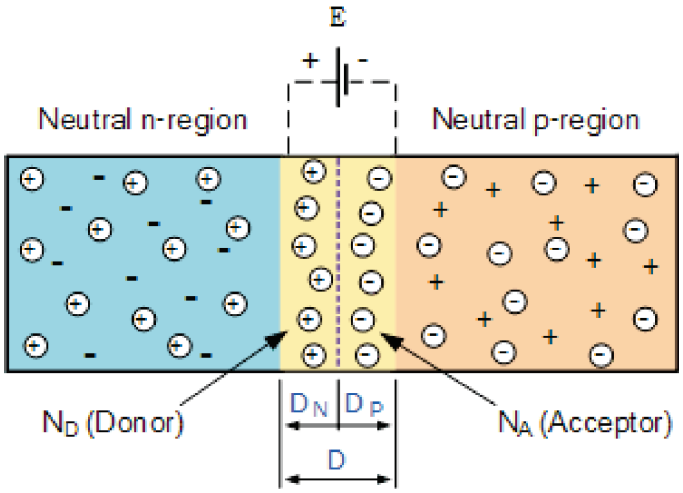

Figure 3.6. P-N junction.
(Source: Wenham et al. 2013)

When the electrons penetrate from n-type region to the p-type region, they leave behind the ionized donor atoms. As a result of this diffusion, electric field is generated from n-type material to p-type material at the junction. Ionized atoms are located in the crystal lattice to the places of the actual crystal atoms and cannot move in the crystal. The region where these positive ions are located is a space charge region, which is called "depletion region". The reason for the formation of the depletion region at the junction is an electric field across the junction that allows the carriers to drift in the opposite direction to the diffusion current. The drift current equilibrates the diffusion current, and the net current becomes zero in case of no voltage application. So, at equilibrium the electrochemical potential is constant.

3.2.1. P-N Junction Under Bias

When the external voltage employed to the junction in such a direction that blocks the potential barrier, thus enabling current flow, it is called forward biasing. Forward bias is applying by connecting positive terminal of the battery to the p-type region and negative terminal to the n-type region (Figure 3.7). As is, the current in the circuit is called forward current. The magnitude of current depends upon the applied forward voltage. If the potential barrier across the junction is decreased, more free electrons from n-type region can penetrate to the p-type region. Correspondingly, the diffusion current

increases. In this case, the drift current doesn't change since it depends on the carrier amount produced within a diffusion length of the depletion region.

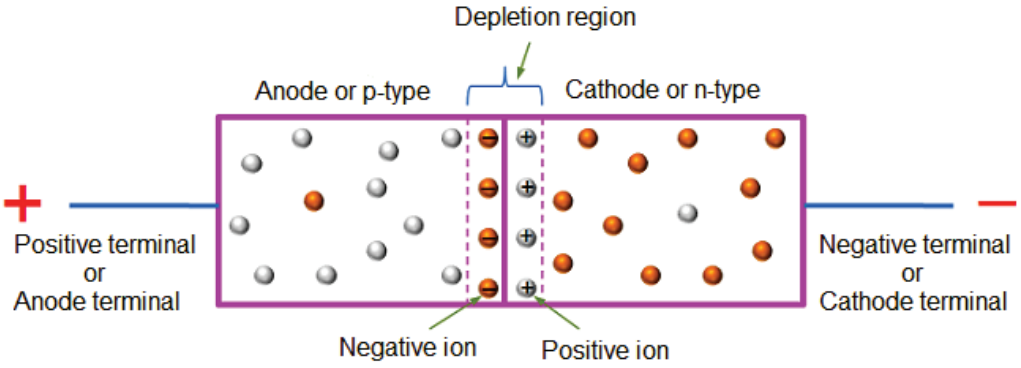

Figure 3.7. P-N junction under forward bias condition.
(Source: Wenham et al. 2013)

When the external voltage employed to the junction in such a direction that increases the potential barrier, it is called reverse biasing. In contradiction to forward bias condition, negative terminal of the battery is connected to the p-type region and positive terminal is connected to the n-type region (Figure 3.8.). The junction shows very high resistance to current flow and the potential barrier is increased. When the small increment occurred in the width of the depletion region, drift current slightly increases. This increment is an effect that referred to a second order in silicon solar cells. However, in many thin film solar cells, where the discharge region is about half of the thickness of the solar cell, the variation in the width of the depletion region with voltage has a great influence on cell operation.

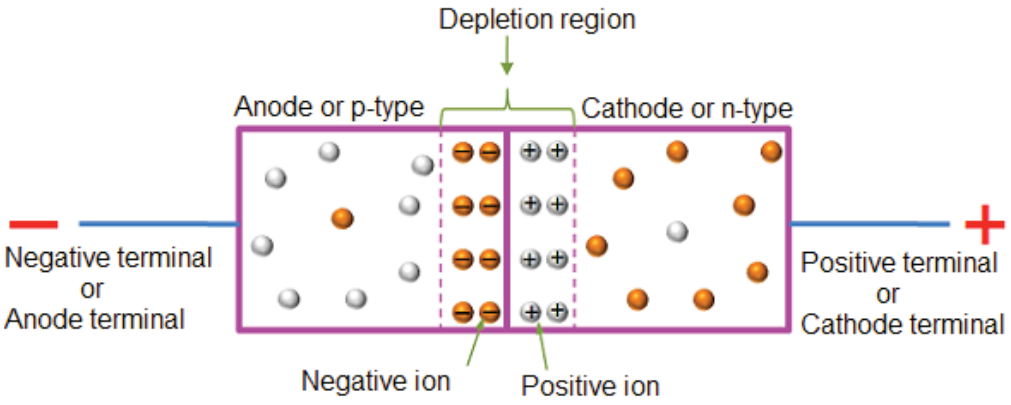

Figure 3.8. P-N junction under reverse bias condition.
(Wenham et al. 2013)

3.2.2. P-N Junction Under Illumination

In order to generate electricity, band gap energy of the material should be lower than the band gap energy of the incident light. In this way photons are absorbed, and additional electron-hole pairs are created in junction. Electrons move towards n-side region while holes move towards p-side region. In the depletion region generated carriers will be pull to the opposite sides since the diffusion length can reach the junction. Only minority carriers will cross the junction. The electrons in the p-side will come close to the n-side and the holes in the n-side will come close to the p-side region. As a result, there is a net increase of the negative charge in the n-side and the positive charge in the p-side. This induces a potential across the p-n junction, and it is known as the photovoltaic effect. Under illumination, the direction of the current flow is from n-type region to p-type region, and it is opposite to the dark current. This current is called photo-current (IL). The current generated by solar cell increases as the intensity of the incident light increases. Under applied voltage, the net current of the p-n junction under illumination is given by;

$$I = I_0\left(e^{\frac{qV}{kT}} - 1\right) - I_L \tag{3.1}$$

In Equation (3.1), I_0 refers to saturation current, q refers to the electron charge, V is voltage, k is Boltzmann's constant and T is absolute temperature in Kelvin unit. For solar cells, main parameter is current. It can be calculated with the given equation.

3.2.3. P-N Junction I-V Characteristics

I-V characteristic for the illuminated p-n junction is represented in Figure 3.9. Illuminated p-n junction creates photocurrent in opposite direction of the dark current therefore I-V curve shifts along the negative current-axis. Current of the solar cell increases with the incident light intensity.

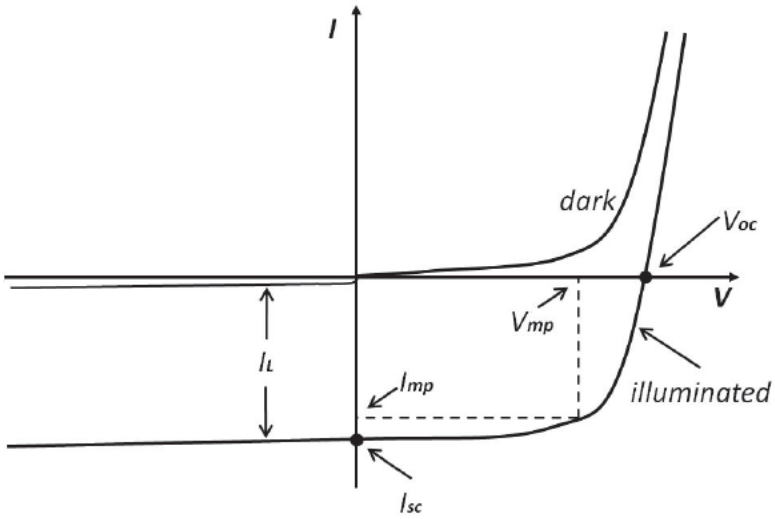

Figure 3.9. Dark and illumination conditions of a solar cell I-V characteristics. (Source: Khudayer 2017)

Figure 3.8 shows that there are four output parameters need to be considered in solar cell. These are open circuit voltage (V_{oc}), short circuit current (I_{sc}), fill factor (FF) and efficiency (η), which determines the performance of the cell.

I_{sc} is measured when V is equal to 0 or the output terminal is by-passed. The short circuit current is formed by the production and collection of photo-generated carriers. Since the short-circuit current is the maximum current delivered by a solar cell, while considering an ideal solar cell, amount of the short-circuit current and the photo-generated current are the same. To obviate the dependance of the cell area, the short circuit current

density (J_{sc} in mA/cm^2) is commonly used to describe the highest current delivered by a solar cell.

The second parameter V_{oc} is measured when I is equal to 0 or the output terminal is unlocked. The value of output voltage V_{oc} demonstrates the maximum output voltage of solar cell at a certain illumination level and can be derived from Equation (3.2). According to the equation, the I_0 should be lower for higher V_{oc}. There is no current flow inside the heterojunction under open circuit condition. It indicates that the current of the flux of photo-generated and thermally generated carriers must be balanced with the reverse recombination current. The recombination current raises as the electrostatic-potential barrier decreases by an amount V_{oc} along the depletion region. V_{oc} depends on the current produced from the light.

$$V \approx \frac{nkT}{q} \ln\left(\frac{I_L}{I_0} - 1\right) \tag{3.2}$$

The third parameter is fill factor "FF" which represents the ratio maximum power to the product V_{oc} and I_{sc}. It decides the maximum power that can be acquired from a solar cell, and it is given by the equation;

$$FF = \frac{V_m \times I_m}{V_{oc} \times I_{sc}} = \frac{P_{max}}{V_{oc} \times I_{sc}} \tag{3.3}$$

Graphically, the area of the largest rectangle that will fit in the I-V curve gives the FF value. For the most part, the solar cell with adequate efficiency accepts FF between 0.7 and 0.85. Energy conversion efficiency (η) in photovoltaic cell is the ratio of the output energy (P_{max}) to the input energy incident on the cell (P_{inc});

$$\eta = \frac{P_{max}}{P_{inc}} = \frac{V_{oc} \times I_{sc} \times FF}{P_{inc}} \quad (3.4)$$

Along with the spectrum and the intensity of the incident light, the temperature of solar cell affects the efficiency. In order to measure the efficiency, standard test conditions (STC) are used as a base which defines temperature of 25 °C and irradiance of 1000 W/m^2 with AM 1.5 spectrum.

3.3. Losses in Solar Cells

In solar cell with no losses, each photon striking the surface is absorbed and transfers its total energy to create an electron-hole pair. If these electron-hole pairs contribute to the generation of photocurrent, 100 % efficiency would be achieved. However, many types of losses occur in real conditions. Theoretically, performance of a solar cell was first studied in the 1960s (Shockley, Queisser, and Queisser 1961). According to the Shockley–Queisser limit, maximum solar power conversion efficiency is around 33.7 % assuming a single p-n junction with band gap of 1.4 - 1.5 eV. Although losses cannot be completely eliminated, they can be reduced. If losses are reduced, performance of the solar cell performance will increase.

3.3.1. Optical Losses

Optical losses majorly affect the power from a solar cell by reducing the short-circuit current. Optical losses comprise of light, which is reflected from the surface, or not absorbed by the cell because an electron-hole pair couldn't have been generated in this case. There are some aspects to reduce the optical losses which are describes as;

- Using anti-reflection coatings for the top surface of the cell.
- Using surface texturing to reduce reflection.
- Minimizing the front contact coverage of the cell surface.
- Optimizing the absorber layer thickness to increase absorption.

3.3.2. Recombination

Recombination occurs if some of the charge carriers (electron and hole) are not collected at the electrodes. Recombination losses affect the current collection and hence, the short-circuit current. V_{oc} is also suffered from this situation. Thus, recombination at the both surface and bulk must be minimized to collect all of the photo-generated carriers at the p-n junction. On the other hand, lattice defects and impurity atoms of the semiconductor can be assumed as a recombination centers.

3.3.3. Thermalization

A solar cell absorbs high energetic photons than band gap but act as a transparent surface to photons with energies lesser than the band gap. Only these high energetic photons produce electron-hole pairs. The excess amount of energy that received from the photons is released as heat into the semiconductor lattice. This energy lost is called thermalization. Therefore, to reduce thermalization loss, the band gap should be as high as possible. But, in order to collect much more photons, a low band gap is required. That's why maximum theoretical efficiency (~ 30%) can be achieved with the band gap is somewhere around 1.4 – 1.5 eV.

3.3.4. Electrical Losses

Fill factor is a significant parameter because it influences the solar cell's maximum power output. However, series resistance and shunt resistance reduce the FF value. Shunt resistance is caused by the leakage of current through the cell due to local defects at the junction or shunts at the edges of solar cells (Nelson 2003). Series resistance arises from the sum of the resistances of the current path when the photo-generated carriers reach to the external circuit. The main impact of series resistance is to cut down the fill factor. The main reasons of series resistance can be listed as follows: the drift of

current through the emitter and base of the solar cell; the contact resistance between the junction and electrodes and the resistance of the electrodes.

The equivalent circuit of a solar cell with series and shunt resistance can be seen in Figure 3.10.

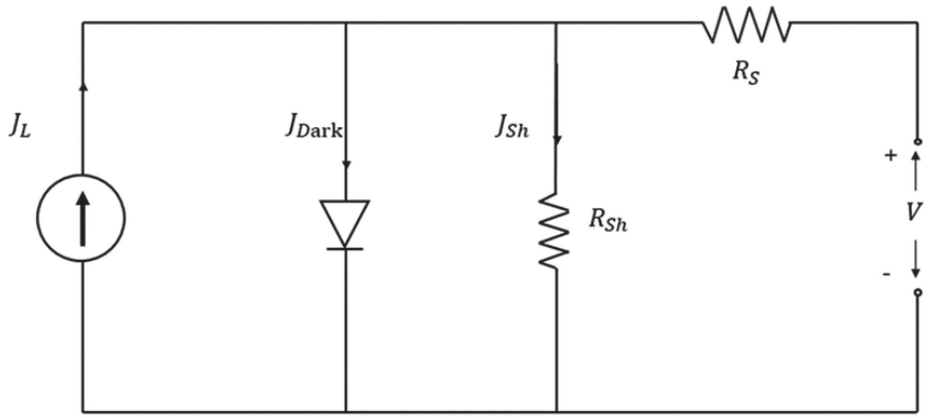

Figure 3.10. The equivalent circuit of a solar cell with series and shunt resistance.
(Source: Karim et al. 2018)

Here, I_L is photo current, I_{Dark} is the diode current, I_{sh} is the shunt current, R_s series resistance and R_{sh} is the shunt resistance. Output current is given by;

$$I = I_L - I_D - I_{sh} \tag{3.5}$$

V_D is the potential across the diode and V is the output voltage given by;

$$V_D = I_{sh}R_{sh} \tag{3.6}$$

$$V = V_D - IR_s \tag{3.7}$$

Based on the above equations, output power for non-ideal solar is designated as;

$$I = I_L - I_0 \left[exp\left(\frac{V + IR_s}{kT}\right) - 1 \right] - \frac{V + IR_s}{R_{sh}} \quad (3.8)$$

3.4. Aim of The Thesis

Although Sb_2Se_3–based solar cell has established a very rapid growth reaching 9.2% (Z. Li et al. 2019) efficiency in a short time like 7 years, it is still lower than the theoretically expected value which is higher than 30%. Therefore, this thesis is dedicated to improving the performance of relatively new Sb_2Se_3 thin film solar cells. In this work, two solar cells in different configurations were fabricated. Instead of toxic CdS buffer layer which is commonly used in Sb_2Se_3 solar cells, Zn(O,S) is used as a buffer layer in this thesis for superstrate solar cell. Zn(O,S)/Sb_2Se_3 structure will be the first device in the literature until now. In order to investigate the effect of Zn(O,S) on solar cell structure and performance, a solar cell was also fabricated with CdS for comparison. Consequently, Zn(O,S) buffer layer is the unique aspect of this thesis. For the rest, the objectives of this thesis are to:

1) provide easy adjustment to fabricating large-scale and reproducible Sb_2Se_3 solar cells using only the magnetron sputtering method for all thin film layers in the Sb_2Se_3 solar cell structure.

2) optimize the sputtering conditions and annealing parameters of the Sb_2Se_3 absorber layer and the Zn(O,S) buffer layer to obtain the solar cell with desired properties.

3) investigate the effect of the thickness on the physical properties of Sb_2Se_3 films.

4) investigate the effect of post-annealing degree and time on the physical properties of Sb_2Se_3 films.

5) investigate the effect of Sb_2Se_3 solar cell structure (substrate and superstrate configuration) on the photo conversion efficiency.

6) Introduce environmentally friendly alternative Zn(O,S) buffer layer to substitute traditionally used CdS buffer layer.

CHAPTER 4

DEVICE STRUCTURE OF Sb_2Se_3 SOLAR CELL

In this thesis, solar cells with different configurations were manufactured as superstrate and substrate structure. Substrate structure is conventionally and extensively used in thin film solar cells. In this structure, the substrate is located at the bottom where the substrate side faces the incident sunlight in a superstrate structure. Substrate type Sb_2Se_3 solar cells ordinarily use CdS as a buffer layer in the literature. In this study, SLG/Mo/Sb_2Se_3/CdS/ITO structured solar cell was fabricated.

In terms of superstrate configuration, instead of the conventional CdS buffer layer, it is proposed to use Zn(O,S) as a buffer layer which will be the novelty of this thesis.

In the following section, layers and included materials used for the manufacture of Sb_2Se_3 solar cells will be briefly presented.

4.1. Substrate

A substrate must be used for thin film solar cells deposition since they are as thin as nanometers to micrometers. It works as a carrier of the cell structure and protector. The most used substrate is soda-lime glass due to its favorable properties. Also, glass is more advantageous in terms of cost. Flexible substrates such as metal foils can be used but solar cells with glass substrates have reached the highest efficiencies.

In superstrate solar cell configuration, the glass substrate is used either as carrier structure or as window for the illumination. It is also part of the encapsulation. Therefore, solar cells with superstrate configuration require less layers and materials.

4.2. Molybdenum (Mo) Back Contact for Substrate Cell

In a standard solar cell, the charge carriers generated from sunlight are collected through the metal contacts on the front and back of the solar cell and transmitted to the circuit. Therefore, initially the back contact layer must be deposited onto substrate. Solar cell performance is substantially affected from back contact material properties. Low resistance, good work function and stability against corrosion, oxidation etc. are necessities for a good contact. A nonreactive back contact is essential for reproducible Sb_2Se_3 solar cells in an extremely corrosive atmosphere process. In addition, to minimize optical losses, a high optical reflectance is necessary.

There are many metals and semi-metals with these properties to be used as a back contact, but for the formation of a good electrical contact to Sb_2Se_3 is still challenging due to the Schottky barrier formation between the interface of an absorber layer and a back contact layer. An ohmic metal/semiconductor contact is established when the back contact for the Sb_2Se_3 satisfies the following condition, otherwise Schottky barrier is come into existence.

$$\phi_m > E_g + x \tag{4.1}$$

where E_g and x are the band gap and electron affinity for a p-type semiconductor, and Φ_m is the work function of a metal.

Molybdenum (Mo) is generally used for Sb_2Se_3 solar cells because it complies well with most requirements. Research on substrate structure Sb_2Se_3 thin film solar cells is very few in number except the report by Chen et al., in which the back contact was fluorine-doped tin oxide (FTO) instead of Mo. However, in that study the poor contact of Sb_2Se_3 and FTO back contact layer resulted in low efficiency. Therefore, Mo is unique for substrate structure Sb_2Se_3 solar cells. As well as its low electrical resistivity, it has other properties which satisfy the most necessities of a good back contact. Mo is thermally stable at high processing temperatures and has perfect adhesion between soda lime glass substrates and Sb_2Se_3 absorber layer. Furthermore, formation of $MoSe_2$ improves the qualification of heterojunction, resulting with a notable increase in V_{oc} and FF (Z. Li et

al. 2017a). In this thesis, Mo deposited soda lime glasses were obtained from TEKNOMA Technological Materials Industrial and Trading Inc. (www.teknoma.net).

4.3. Silver (Ag) Top Conctact for Superstrate Cell

Same as the back contact, the work function value of the material to be used as the top contact plays a crucial role. The increase in the work function of the material to be used as a metal contact, prevents recombination that will occur at the metal/p-type semiconductor interface by increasing the Schottky barrier between the metal and the p-type material. This effect increases the V_{oc} value and correspondingly the efficiency.

In the literature, Sb_2Se_3 thin film solar cells conventionally use Mo as the back contact metal (substrate configuration) and gold (Au) or silver (Ag) as the top contact metal (superstrate configuration) (Z. Li et al. 2017a; L. Wang et al. 2017). However, the high cost of Au contact and pattering problems makes it unfavorable in real applications. Silver as the top contact is a popular metal due to its high work function (Φ_m = 4.73 eV), low cost, high electrical conductivity and long-term stability (Meier et al. 2013).

In recent years, many experimental studies showed that the efficiency of the solar cell had been enhanced by Ag diffusion into the absorber layer (Cui et al. 2015; Guchhait et al. 2016; Yun Zhao et al. 2020). Choi and his research group grew Sb_2Se_3 nanowires using the hot injection method and added $AgNO_3$ into the nanowire solution. As a result of this process, the electrical conductivity of Sb_2Se_3 nanowires increased and also their photosensitivity improved (Choi et al. 2014). Because of these, Ag was preferred as the top contact metal in this thesis.

4.4. A Review of Sb_2Se_3 Absorber Layer

Inorganic thin film solar cells use cadmium telluride (CdTe), amorphous silicon (a-Si), copper indium diselenide (CIS), copper indium gallium diselenide (CIGS), and $Cu_2ZnSnS(e)_4$ (CZTSe) materials as absorber layer in the cell structure. Among them CdTe and CIGS are traditional inorganic thin film solar cells which have succeed in power conversion efficiency over 22% (Powalla et al. 2018). Although these thin film

solar cells have been mass produced, the toxicity of cadmium (Cd) and rare elements such as indium, gallium and tellurium make them costly and non-safe solar cells (Buldu et al. 2018; X. Liang et al. 2019). For these reasons, to compete with expensive CIGS and toxic CdTe based solar cells, there are a lot of interest in research on solar cells containing low-cost absorber layer having high power conversion. Against to these obstacles, low-cost and earth-abundant binary compound Sb_2Se_3 has been suggested for solar cell application. Antimony chalcogenides, i.e. Sb_2Se_3, Sb_2S_3, and $Sb_2(S,Se)_3$ have excellent stability when subjected to water or oxygen (J. Zhang et al. 2020). Sb_2Se_3 exhibits excellent physical properties such as favorable bandgap to Shockley-Queisser limit (E_g = 1.1 – 1.3 eV), a high absorption coefficient (> 10^5 cm^{-1}), carrier mobility of approximately 10 cm^2 $V^{-1}s^{-1}$, and a lifetime of 60 ns for minority carriers. For these reasons, it is a promising candidate for high efficiency PV applications (L. Wang et al. 2017).

The utilization from Sb_2Se_3 in photovoltaics as photon-absorber was studied by Nair et al. in 2000s, reaching a quite small conversion efficiency of 0.66% (Messina, Nair, and Nair 2009). Since the remarkable efficiency values of 3.21% and 2.26% acquired in 2014 respectively, Sb_2Se_3 based solar cells have developed rapidly (Zhou et al. 2014; Choi et al. 2014). It is known that the structural and physical properties of films that sputter-deposited were strongly affected by the growth process parameters such as gas pressure, RF power and substrate temperature (Cantas et al. 2018; Yazici et al. 2015). Yuan and his research group examined the effects of annealing temperature on selenizing metal precursor deposited by sputtering and reached the efficiency of 0.72% in 2016 (Yuan, Jin, et al. 2016). Liang and his research group reported the temperature dependent Sb_2Se_3 film growth by sputtering, eventually reaching an efficiency of 3.35% in 2018 (G. X. Liang et al. 2018a). 1D materials such as Bi_2S_3, Sb_2S_3 and Sb_2Se_3 which have strong bonds in only one direction, are referred to chain compounds. Low structural dimensionality fatally causes to low electronic dimensionality, resulting in very strong anisotropy of the charge carrier mobilities. Therefore, in order to successfully use low-size materials in thin film solar cells, controlling to orientation of the absorber layer plays a crucial role (Kondrotas et al. 2019). The importance of the orientation of Sb_2Se_3 films for the device performance was first demonstrated by Zhou and his research group. When the absorber layer is oriented along with the c-axis, charge carrier density increased so the efficiency of Sb_2Se_3 based solar cells are almost doubled. In this study, Sb_2Se_3 films grown in the form of 1D ribbons by rapid thermal evaporation method onto the substrate

perpendicularly. They obtained 5.6% yield from the films with superstrate configuration SLG/ITO/CdS/Sb_2Se_3/Au thin film solar cell (Zhou et al. 2015). Chen and his research group succeeded to increase the efficiency up to 6.5% with using PbS film as a hole transport layer (HTL) in superstrate SLG/ITO/CdS/Sb_2Se_3/HTL/Au solar cell. As a consequence, an improvement was observed in all electrical parameters (open circuit voltage (V_{oc}), short circuit current density (J_{sc}) and fill factor (FF)) (C. Chen, Wang, et al. 2017). In 2018, Wen and his research group used rapid thermal evaporation (RTE) method to develop Sb_2Se_3 solar cells. RTE is a procedure like close spaced sublimation where the steam is limited to an area and deposits rapidly on the substrate. By means of this technique, crystallinity of Sb_2Se_3 films improved and the efficiency increased up to 7.2% in superstrate ITO/CdS/Sb_2Se_3/Au solar cells (Wen et al. 2018). Following Wen's work, Li and his research group constructed nanorod arrays of Sb_2Se_3 and [001]-oriented solar cells on Mo coated glass substrates with the close spaced sublimation (CSS) method. They investigated the CdS/Sb_2Se_3 nanorod interface and hence, the junction structure. They showed that the element antimony (Sb) drifts through the entire CdS buffer layer if no definite protection was taken. Subsequently, they insert a very thin titanium oxide (TiO_2) layer coated by atomic layer deposition (ALD) method at the CdS/Sb_2Se_3 heterojunction interface. This interface engineering with TiO_2 enabled to obtain verified record conversion efficiency of 9.2% for the Sb_2Se_3 solar cells (ZnO:Al/ZnO/CdS/TiO_2/Sb_2Se_3 nanorod arrays/$MoSe_2$/Mo) with an absorber thickness over 1000 nm while maintaining a high fill factor of 70.3% (Z. Li et al. 2019). However, the efficiency of Sb_2Se_3 solar cells is still far from the theoretical value. Studies are going on to improve.

4.4.1. Crystal Structure

Sb_2Se_3 is a binary compound with an orthorhombic crystal structure and a member of the space group Pmna (62). The crystal structure parameters of Sb_2Se_3 were calculated by other research groups. Sb_2Se_3 compound has lattice constants of a=11.62 ± 0.01 Å, b=3.962 ± 0.007 Å, and c=11.77 ± 0.01 Å, with a primitive cell volume of 0.524 nm^{-3} and density of 5810 kg/m^3 (Caracas and Gonze 2005; Tideswell and McCullough 1957; Zeng, Xue, and Tang 2016). There are existing Se-Sb-Se chains (ribbons) along the c-

axis, in the Sb_2Se_3 structure. In other words, crystal structure of Sb_2Se_3 is composed of one-dimensional (1D) units. Sb_4Se_6 units are bound by weak Se–Se interactions and form this 1D structure (Voutsas et al. 1985). As a one-dimensional material, control of the crystal orientation of Sb_2Se_3 film is a key factor to achieve efficient charge carrier transmission and useful grain boundaries. Due to the unique semi-1D crystal structure, the orientation of Sb_2Se_3 absorber films plays a critical role in the transmission of charge carriers and accordingly in the performance of solar cells. During the deposition, Sb_2Se_3 films can be crystallized in horizontal (hk0) or vertical (hkl, $1 \neq 0$) shapes in which the c axis bends to the substrate, depending on the type and temperature of the substrate used. From a photovoltaic point of view, the second vertical orientation is considered to be beneficial for the transmission of charge carriers along the absorber layer (Kondrotas et al. 2019).

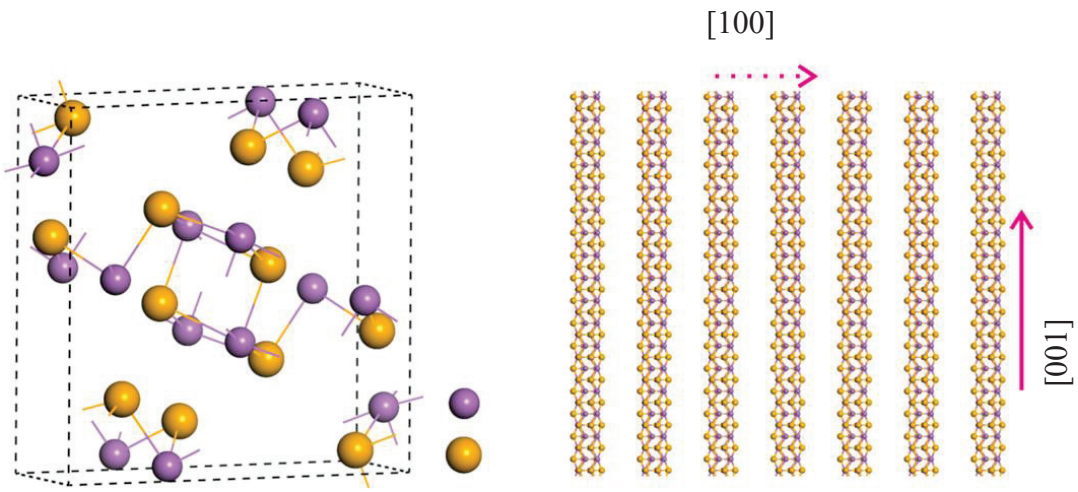

Figure 4.1.Crystal structure of Sb_2Se_3.
(Source: Zeng, Xue, and Tang 2016)

4.4.2. Optical Properties of Sb_2Se_3

The optical properties of Sb_2Se_3 are determined by both crystal structure and chemical formulation. Band gap energy (E_g) of polycrystalline Sb_2Se_3 films with stoichiometric composition is in the range of 1.0 – 1.3 eV (C. Chen et al. 2015; Shen et al. 2018). However, sometimes fluctuation in the band gap of Sb_2Se_3 was observed by changing the material composition or using different growth conditions. Except

experimental results theoretical outcomes reveals that the E_g of Sb_2Se_3 stands within the optimal range to achieve high PCE (Figure. 4.2) (Shockley, Queisser, and Queisser 1961).

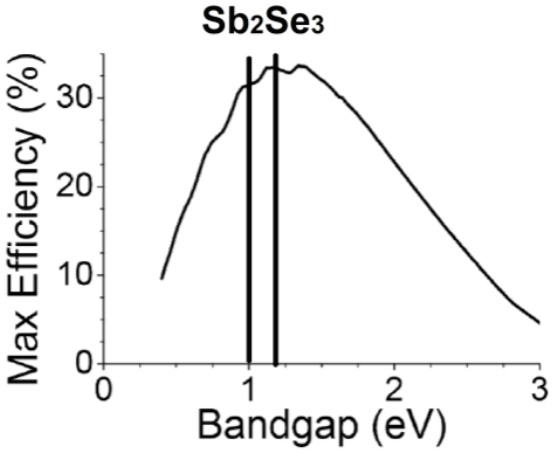

Figure 4.2. E_g value of Sb_2Se_3.
(Source: Shockley, Queisser, and Queisser 1961)

The absorption coefficient of Sb_2Se_3 thin films was found to be larger than 10^5 cm^{-1} (Lai et al. 2012; K. Li and Tang 2018; G. X. Liang et al. 2018b; J. Liu et al. 2020). This value is ideal for PV solar cell applications and much higher than that of other solar cell absorber layers (Sun et al. 2013). In addition, 400 nm thick Sb_2Se_3 film completely absorbs the photons with wavelengths $\lambda > 800$ nm (C. Chen et al. 2015). Compared to other conventional absorbers, this value remains below. Moreover, Sb_2Se_3 has higher εr values (> 18 $\varepsilon 0$) than CdTe (10.0 $\varepsilon 0$) and $CuInSe_2$ (14.3 $\varepsilon 0$), which is favorable for the absorber layer (C. Chen, Wang, et al. 2017).

4.4.3. Raman Analysis of Sb_2Se_3

Raman spectroscopy was used to investigate the vibration modes of Sb_2Se_3 films. It is a fast and non-destructive technique which characterizes Sb_2Se_3 and its impurity phases. When light interacts with sample molecules, the majority of photons are separated or scattered at the same energy with incident photons. This is defined as elastic scattering or Rayleigh scattering. A small number of photons (about one photon in 10 million) are scattered at a different frequency than the incident photon. This process is called inelastic

scattering or the Raman effect. The energy difference between the incident photons and those scattered by the sample corresponds to the vibrational energy levels of the molecule diffusing. Information about the molecular structure and chemical composition can be obtained from the analysis of the shift of the spectral lines.

According to group theory, for the unit cell Sb_2Se_3, 30 regions belong to the central irreducible representation, and the Raman active phonon modes are $\Gamma_{Raman} = 10\ A_g + 10\ B_{1g} + 5\ B_{2g} + 5\ B_{3g}$ (Efthimiopoulos et al. 2013). By removing the zero frequency acoustic phonon modes, a total of 27 optical Raman modes are expected to be observed. Although there are many theoretically expected phonon modes for the Sb_2Se_3 compound, very few Raman peaks were observed in the previous studies (Shongalova, Correia, Vermang, et al. 2018). Zhang's research group studied the annealing effect on Raman analysis (Figure 4.3).

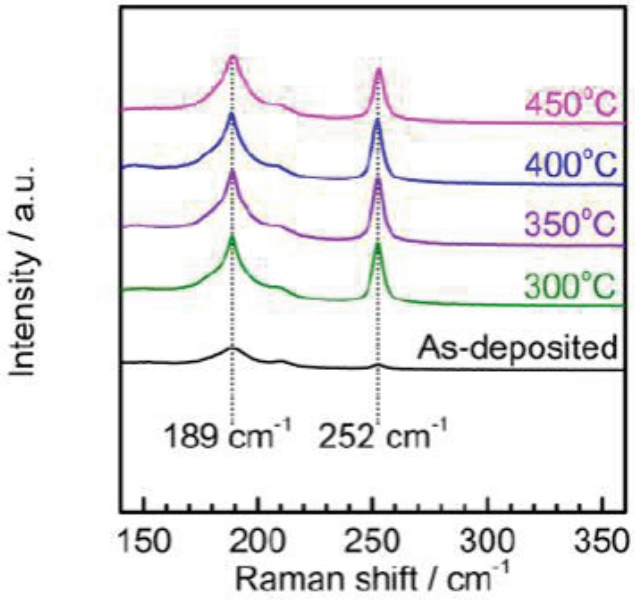

Figure 4.3. Raman spectrum for Sb_2Se_3 absorber layer annealed at different temperatures.
(C. Zhang et al. 2017)

4.4.4. Electrical Properties of Sb_2Se_3

The electrical property of Sb_2Se_3 films is one of the most important factor for its performance in devices. Although Sb_2Se_3 material is generally an intrinsic p-type semiconductor (Lai et al. 2012), some Sb_2Se_3 films may exhibit n-type conductivity due to doping. However, the p-type conductivity of the Sb_2Se_3 absorber has been used for solar cells, therefore arguments represented in this work based on p-type Sb_2Se_3.

Sb_2Se_3 compound has desirable optoelectronic features such as favorable band gap energy (1.0-1.2 eV) (C. Zhang et al. 2017), high absorption coefficient ($>10^5$ cm^{-1}), and long carrier lifetime of about 60 ns according to short-term absorption spectroscopy (L. Wang et al. 2017). While the electron mobility given in the literature for the Sb_2Se_3 semiconductor is 15 cm^2 V^{-1} s^{-1}, the hole mobility is given as 42 cm^2 V^{-1} s^{-1} which is suitable for use as an absorber layer in solar cells (C. Chen, Bobela, et al. 2017).

4.5. Buffer Layer

Buffer layer is required to complete the p-n heterojunction. It is deposited on p-type Sb_2Se_3 absorber layer and protects absorber layer from any processes such as damage during other layer deposition stage. Buffer layer absorbs almost whole incident light to create photo-generated carriers and transfers these charge carriers to the absorber layer. Besides, it helps to minimize the interface recombination. Thickness of the buffer layer is usually quite thin, 50 to 200 nm, to avoid series resistance. Besides, less thickness enables to increase the light transmission as well as device performance. The band gap value of the buffer layer is somewhere between the window layer and the absorber layer band gap. Hence, the conduction band offset, ΔE_c, is significantly reduced (Turkoglu et al. 2019). For this reason, the band gap value of the buffer layer needs to be larger to reduce high energetic photon absorption.

4.5.1. Cadmium Sulphide (CdS) as a Buffer Layer for Substrate Cell

Cadmium sulphide (CdS) is a II–VI compound and an n-type semiconductor. It has an energy band gap of 2.42 eV at room temperature (Lisco et al. 2015). CdS has been emerged as an ideal material for employing as the buffer layer of heterojunction solar cells due to its physical properties. It has a high absorption coefficient and a good transparency in the visible region. In addition, it is easily ohmic contact to various materials. Therefore, it had been functioned as a buffer layer in many solar cells such as Cu_2ZnSnS_4 (CZTS) (Tajima et al. 2017), $Cu(In,Ga)Se_2$ (CIGS) (Lindahl et al. 2013), Sb_2Se_3 (Wen et al. 2021), Sb_2S_3 (Escorcia-García et al. 2018), CdTe (Harif et al. 2020).

CdS films can be deposited using various methods such as chemical bath deposition (CBD) (Cantas et al. 2018), vacuum evaporation, sputtering, spray pyrolysis, photochemical deposition, electrodeposition, etc. Among these, CBD technique is a well-established technique with low temperature process (27 – 80 °C) and cheap (H. Chen et al. 2010). Deposition rate, thickness, pH concentration and temperature can be controlled during the coating.

In the literature, the highest solar cells of CIGS, CZTS and Sb_2Se_3 were achieved using CdS buffer layer with 22.8% (Huang et al. 2018), 9.4% (Tajima et al. 2017), 9.2% (Z. Li et al. 2019) photo-conversion efficiency, respectively. However, there are alternative buffer layers for CdS such as Zn(O,S) and ZnS with wider bandgap. Due to its versatility, Zn(O,S) is a promising candidate for replacing the traditional and toxic CdS as a buffer layer.

4.5.2. Zinc Oxysulfide (Zn(O,S)) Buffer for Superstrate Cell

Zinc oxysulfide (Zn(O,S)) thin films are II–VI compound semiconductors and have been successfully used as phosphor host materials (Sanders and Kitai 1992) and photo-catalysts (Pandey et al. 2013) up to now. Due to the tunability of their compositional and crystal structure, there is a rapid increase in the use of Zn(O,S) as a buffer layer in solar cells. In addition to its functional tunability, Zn(O,S) buffer layer also contains elements that are non-toxic and abundant on earth. Owing to its versatility,

Zn(O,S) is an excellent candidate for substituting the traditional CdS as a buffer layer since it is coherent to several absorber layers, such as SnS, CIGS, CIS, and CZTS (Grimm et al. 2010; 2011; Kieven et al. 2012; Platzer-Björkman et al. 2006; Yousfi, Fouache, and Lincot 2000).

Zn(O,S) is also expressed as $ZnO_{1-x}S_x$ when $0 < x \leq 1$. The S/(S+O) ratio in $ZnO_{1-x}S_x$ can easily vary by changing experimental parameters (e.g changing the O_2/Ar gas composition during sputtering). Since their composition is adjustable, essential parameters such as conduction band offset, bandgap, and conductivity can be precisely controlled (Buffière et al. 2015; Pandey et al. 2014; Platzer-Björkman et al. 2003; Sinsermsuksakul et al. 2013; Sun et al. 2013).

Zn(O,S) is a mixture of ZnO and ZnS which have wide band gaps such as 3.54 eV (Hervé and Vandamme 1994) and 3.3 eV (Srikant and Clarke 1998), respectively. The band gap of the Zn(O,S) can exhibit a very strong bowing effect (bowing parameter b of 3 eV) as the S/(S+O) ratio fluctuates (Eicke et al. 2013; Platzer-Björkman et al. 2006), with a minimum energy gap of 2.6 eV for a S/(S + O) ratio of 45 % (Meyer et al. 2004). Figure 4.4 shows bandgap bowing of $ZnO_{1-x}S_x$ thin films deposited by magnetron sputtering system (Meyer et al. 2004). A large bandgap (2.6 - 3.8 eV) makes possible to collect more high energetic electrons, and thus reduces the photocurrent loss in the short wavelength region. Moreover, by means of the careful arrangement of the sulfur content, recombination can be minimized at the buffer interface (Platzer-Björkman et al. 2006).

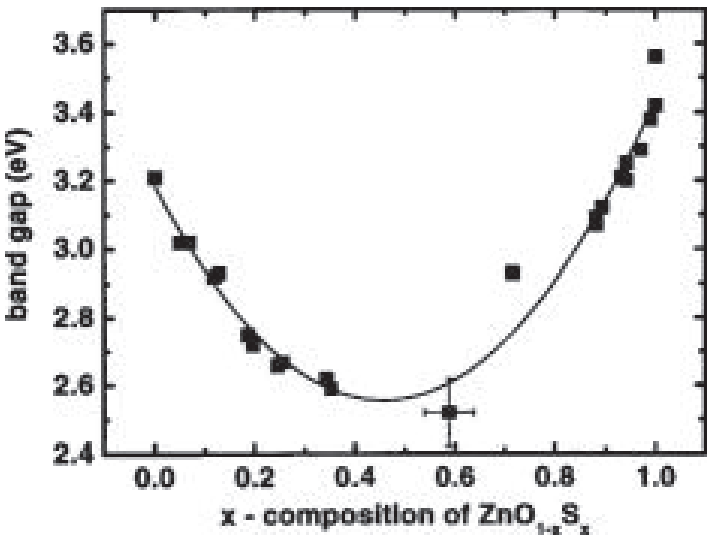

Figure 4. 4. Band gap energy of $ZnO_{1-x}S_x$ films as a function of the composition x. (Meyer et al. 2004)

Furthermore, fluctuations of S and O contents in the Zn(O,S) buffer layer allow the conduction band offset (CBO) value to be adjusted at the p-n junction interface and this is providing an additional opportunity to increase the efficiency. The tunable buffer layer plays an important role in the performance of solar cells.

The deposition of Zn(O,S) thin films has been performed using various deposition methods such as chemical bath deposition (CBD) (Buffière et al. 2011; Kushiya 2004; Sáez-Araoz et al. 2008; Witte, Abou-Ras, and Hariskos 2013), atomic layer deposition (ALD) (Platzer-Björkman et al. 2003; 2006; Sanders and Kitai 1992; Zimmermann, Ruth, and Edoff 2006), ion layer gas reaction (ILGAR) (Muffler et al. 2000), evaporation (Romeo, Bosio, and Romeo 2010), sputtering (Grimm et al. 2010; 2011; Klenk et al. 2014; M. Nakamura et al. 2013), and pulse laser deposition (PLD) (Deulkar, Huang, and Neumann-Spallart 2010; Yoo et al. 2002). Despite the differences in the deposition techniques carried out by the various groups, most of the research groups use a Zn(O,S) buffer of about 50-100 nm.

The doping of S into ZnO was first performed by Yoo and his research group using the PLD technique (Yoo et al. 2002). They showed that the S concentration of single-phase wurtzite Zn(O,S) thin films deposited on c-plane sapphire at 700 °C was limited to 0.13, and above this value, the $ZnSO_4$ phase appeared (in addition to ZnS and ZnO). They also observed that both the band gap and the c-axis lattice constant showed a non-linear correlation with the variation of the S content in the thin films. Meyer et al., 2004 succeed to synthesize single-phase wurtzite $ZnO_{1-x}S_x$ films almost in the entire composition interval on both glass and c-plane sapphire substrates at a relatively low substrate temperature of 340 °C by RF reactive sputtering and using a ZnS ceramic target with Ar/O_2 as reactive gases (Meyer et al. 2004). They observed that the c-axis lattice constant changed linearly as the energy gap changed nonlinearly with the sulfur content in the Zn(O,S) compound, and an optical bowing parameter was designated as 3.0 eV. Locmelis et al., 2007 found nearly symmetrical solubility of about 5 mol % for $ZnO_{1-x}S_x$ crystals grown by chemical transport reactions at 900 °C (Locmelis et al. 2007). Using a method similar to Meyer et al., 2004, Pan et al., 2010 deposited the $ZnO_{1-x}S_x$ films on glass substrates at 300 °C and after the deposition, applied heat treatment to the films at 500–600 °C (Meyer et al. 2004; Pan et al. 2010). They realized that wurtzite structure with (002) preferred orientation formed in the O-rich region ($0 \leq x \leq 0.23$) and zinc blende structure with (111) preferred orientation formed in S-rich region ($0.77 \leq x \leq 1$). Two phases

of w- and β- $ZnO_{1-x}S_x$ coexisted in the composition range of $0.23<x<0.77$. Despite all these studies and observations, more experimental studies are needed.

The highest efficiencies reported for CIGS solar cells have been achieved by using CBD or ALD methods in the Zn(O,S) buffer layer, 22.3% (Kamada et al. 2017) and 21.0% (Friedlmeier et al. 2015), respectively. When grown by CBD method, the Zn(O,S) layer had been reported to be a blend of ZnS, ZnO, and $Zn(OH)_2$ (Bhattacharya et al. 2005; Nakada and Mizutani 2000) because it is difficult to obtain stable films with this method. Although the ALD method is beneficent, CIGSe devices that using Zn(O,S) buffer layer which has been grown by RF magnetron sputtering from a binary compound target with an argon pressure of 5 μbar, obtained efficiencies above 18% (Klenk et al. 2014).

Until this time, many experimental approaches have been made to analyze the performance of CdS/Sb_2Se_3, ZnO/Sb_2Se_3 and ZnS/Sb_2Se_3 devices. But (to our knowledge) there is no experimental study on thin-film solar cells based on $ZnO_{1-x}S_x/Sb_2Se_3$ p-n junction in the literature.

4.6. Indium Tin Oxide (ITO) Window Layer

Transparent conductive oxide (TCO) thin films, such as zinc oxide (ZnO), tin oxide, indium tin oxide (ITO), aluminum doped zinc oxide (AZO) and cadmium tin oxide are used for a broad range of significant applications such as transparent electrodes in LCDs, organic light emitting diodes, lenses, sensors and solar cells (G. Li et al. 2018). Among TCO thin films, ITO is widely used because of its unique electrical and optical properties such as good conductivity (about $10^4\ \Omega^{-1}\ cm^{-1}$) and high transmittance (~88%) in the visible region. As-grown ITO thin films are usually intrinsic n-type semiconductors due to the oxygen vacancies and substitutional Sn dopants (Wohlmuth and Adesida 2005). ITO has a large band gap of about 3.70 eV at room temperature which makes this material suitable for solar cells.

Various methods, such as electron beam evaporation (Jang et al. 2007), ion beam assisted deposition (Yu and Lee 2014), pulsed laser deposition (Socol et al. 2019), ion implantation (Oluwaleye et al. 2019), and DC/RF magnetron sputtering (Tuna et al. 2010)

are used for the deposition of ITO thin films. Most of the reports used O_2 as a reactive gas during the deposition.

ITO was used as a window layer in this thesis. It is deposited onto buffer layer to prevent the reduction in the V_{oc}. When ITO contacts with the buffer layer, it must be very resistive or act as an insulator to prevent recombination at the interface.

CHAPTER 5

EXPERIMENTAL PROCEDURES

5.1. Growth Method of Sb_2Se_3 Absorber

In this study, magnetron sputtering system was used to grow Sb_2Se_3 absorber films. The magnetron sputtering technique is a vacuum deposition process that is categorized of physical vapor deposition (PVD). Mainly metals, alloys and composite textile materials are deposited on a substrate. A target or metallic precursor is bombarded with energetic ions of inert gases (e.g., argon or helium) within this technique. As a result of the collision between these energetic ions and the target, the metal atoms are sputtered and deposited to form a film onto the substrate. For this reason, it is a technique frequently used in thin film coatings. During deposition, the target material is cooled with water, so very little radiation heat is generated. As the target material, a wide variety of metals can be used, including silver, copper, tin, titanium, silicon, and carbon nitride. Advantages of the magnetron sputtering method can be listed as:

- Deposition process is rapid and there is no temperature increase on the substrate.
- The target material spectrum is wide (both conductor and insulator).
- High quality films are obtained with good adhesion.
- It is a repeatable process and applicable for large scale substrates.
- The thickness of the film can be controlled.

The magnetron sputtering method is preferred owing to advantages mentioned above.

5.1.1. Deposition of Sb_2Se_3

In this study, solar cells were fabricated with two different configurations (substrate and superstrate) that mentioned in the “Device Structure” section. For substrate structure, 1 μm thick Mo back contact which was coated on soda lime glass (SLG) is used as a substrate. For superstrate structure, 200 nm thick ITO top contact which was coated

on SLG is used as a substrate. Substrates are cleaned by ultrasonication in acetone, ethanol, and distilled water, respectively and then dried by a nitrogen gun. As demonstrated in Figure 5.1 multi-target magnetron sputtering system was used to deposit Sb_2Se_3 films on substrates. Multi-target magnetron sputtering system comprise of 2-inch alloy targets of Sb_2Se_3 (99.999%) and ZnS. The remaining sputtering target guns were empty. The distance between target to substrate was fixed at 8 cm and for the deposition of an absorber layer, substrate holder was rotated 180 degrees to deposit twice. Before the sputtering, the vacuum chamber was evacuated by Rough Pump (RP) and then evacuated at around 10^{-6} Torr by Turbo Molecular Pump (TMP). Heating was not applied to the substrates during sputtering. After reaching to the required pressure, a constant amount of 30 sccm Ar gas was sent into the chamber as long as the deposition time. The operating pressure was constant along with the deposition process and kept at 1.5×10^{-2} Torr. Since the thickness of the absorber layer is one of the key parameters in the performance of the solar cell, it was desired to obtain 500 nm thick Sb_2Se_3 film.

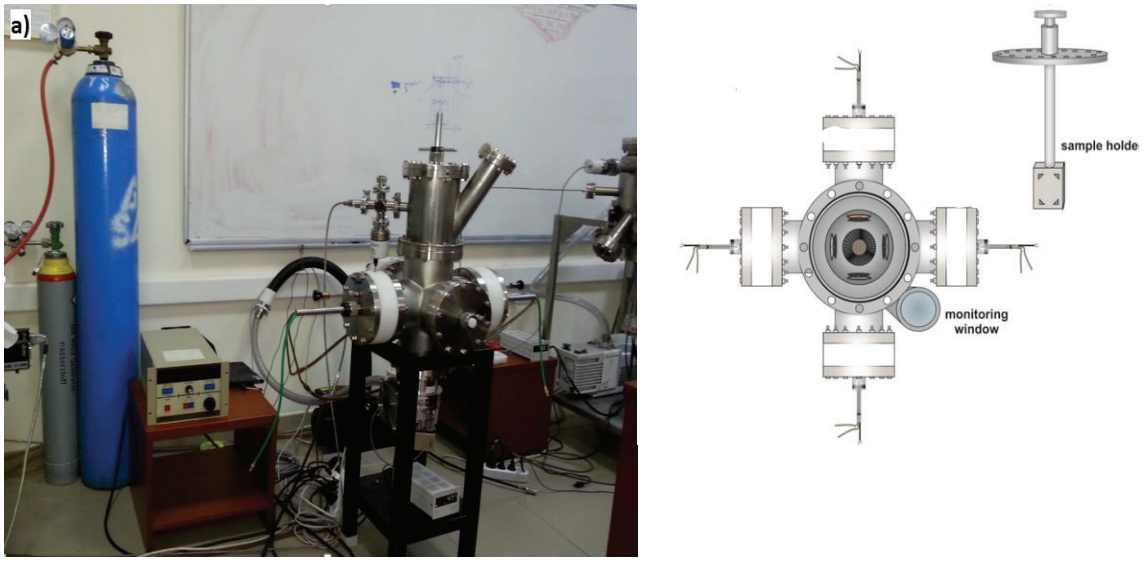

Figure 5.1. a) The magnetron sputtering system used for the growth of Sb_2Se_3 and Zn(O,S) films b) top view of the system.

The thickness calibration of each target was performed using density and molecular weight of each element before the sputtering. Hereby, the compositional ratio can be easily checked. Since in the literature highly efficient solar cells are reported with having Se-rich composition, Sb_2Se_3 films were obtained at this rate. RF and DC supply

sources were used to deposit at 30W RF power and 20W DC power for the Sb_2Se_3 target. Thickness of the Sb_2Se_3 absorber layer was kept constant at 500 nm.

5.1.2. Annealing of Sb_2Se_3 Thin Films

In order to increase the crystallization of Sb_2Se_3 thin films, heat treatment applied through the furnace system which shown in Figure 5.2. Annealing process was performed with a quartz glass tube (Lindberg/Blue M tube furnace) under Ar atmosphere. Sb_2Se_3 films were placed at the center of the furnace. The heat treatment temperature range is between 150 and 450 ˚C, and it was carried out under 100 sccm Ar (using a MKS 647C mass flow controller) gas flow for 30 minutes. For each sample, the heat treatment temperature was increased at a constant rate of 20 ˚C/min, and the sample was left to cool naturally after the heat treatment. Heat treatment parameters are given in Table 5.1.

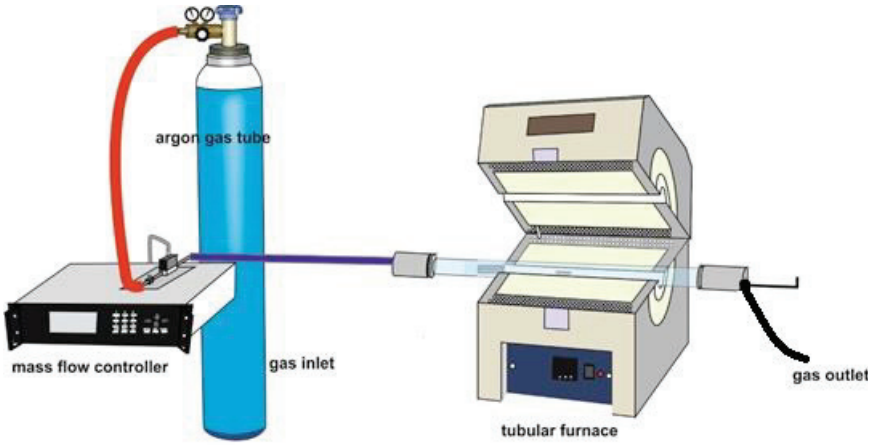

Figure 5.2. Furnace System.

When the temperature dependent physical and electrical properties of the films are compared, 350 °C was determined as the optimum value. Moreover, the effect of temperature on Sb_2Se_3 films will be discussed in Chapter 6.

Table 5. 1. Heat treatment parameters applied to Sb_2Se_3 films.

Temperature	**150**	**200**	**250**	**300**	**350**	**400**	**450**
Ar gas (sccm)	100	100	100	100	100	100	100
Annealing time	30	30	30	30	30	30	30
Ramping rate (°C/min.)	20	20	20	20	20	20	20

5.2. Chemical Bath Deposition (CBD) of CdS Buffer Layer

Substrate type Sb_2Se_3 solar cells commonly used CdS as a buffer layer. The buffer layer thickness of the CdS film was determined to be optimum 50 nm. The thinner is better for n-type buffer layer for an ideal solar cell because if the buffer layer is too thick, p-n junction does not work. Hence, there will be no electricity generation.

Calibration of CdS film has been done by our research group and reported in the literature (Cantas et al. 2018). Figure 5.3 shows the CBD system. In the deposition system two different size beakers were used. The big one function as a water bath tank and the small one was used for the chemical bath deposition. The bath chemical liquid includes 1.19 ml of 0.5 M cadmium acetate ($Cd(CH_3CO_2)_2$), 6 ml of 2 M ammonium acetate ($NH_4CH_3CO_2$), 6.5 ml of 0.5 M thiourea $SC(NH_2)_2$, and 12 ml of 14.5 M (25% of NH_3 solution) ammonium hydroxide (NH_4OH) and 280 ml of de-ionized water. The CdS buffer layer was coated at 85 °C for 45 minutes on SLG/Mo/Sb_2Se_3 film which will become a substrate solar cell.

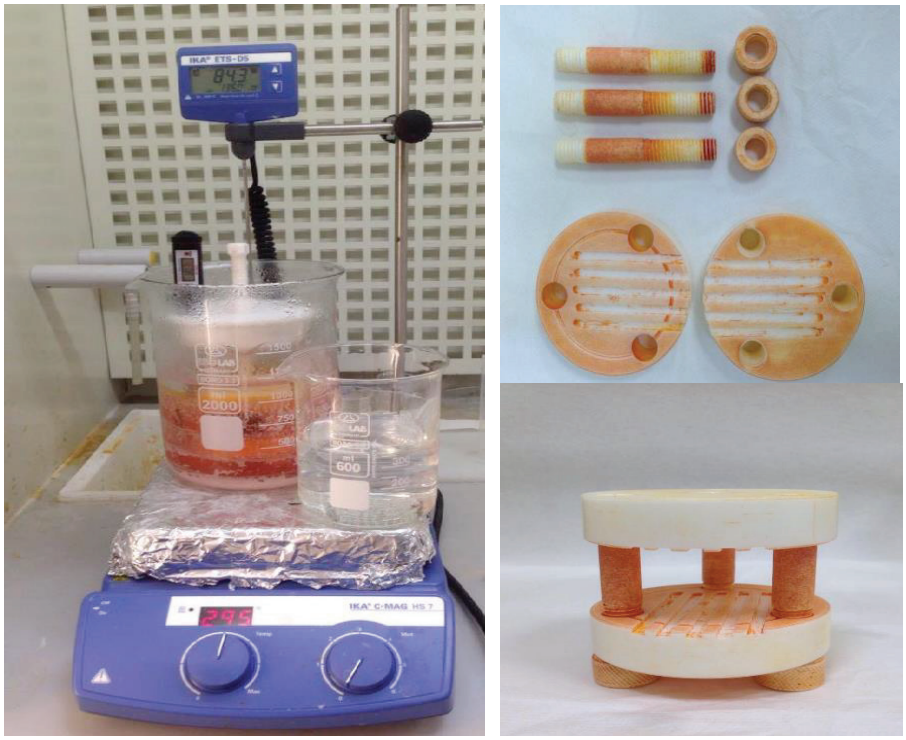

Figure 5.3. Chemical Bath Deposition System
(Source: Cantas 2017)

5.3. Deposition of Zn(O,S) Buffer Layer

In this experimental study, 50 nm thick Zn(O,S) ($ZnO_{1-x}S_x$) buffer layer was used to complete the p-n junction with the Sb_2Se_3 absorber layer. The n-type semiconductor Zn(O,S) buffer layer was deposited on SLG/ITO film by reactive RF magnetron sputtering method using a 2 inch diameter ZnS target (Figure 5.1). Characteristic deposition parameters were a base pressure of $2.0x10^{-6}$ Torr, an RF power of 40 W and target to substrate distance was 8 cm. The deposition was performed under 50 sccm Ar gas. In order to produce $ZnO_{1-x}S_x$ films with different oxygen and sulfur concentrations, the deposition was carried out with 0.5 sccm and 1 sccm oxygen. Oxygen partial pressure (O/(Ar+O)) was 0.99% and 1.96% for deposited Zn(O,S) thin films, respectively.

5.4. Evaporation of Ag Top Contact Layer

The vacuum thermal evaporation technique is evaporation of the material in filament boat heated by high current source and re-condensation of the material with vapor state onto cooler substrate. The material vapor finally condenses in the form of thin film. Usually low pressures are used, about 10^{-5} or 10^{-6} Torr. It ensures silver layer to be coated without damaging to substrate surface. The value of the current required for evaporation varies with the filament boat resistance. The thermal evaporation system is given in Figure 5.4.

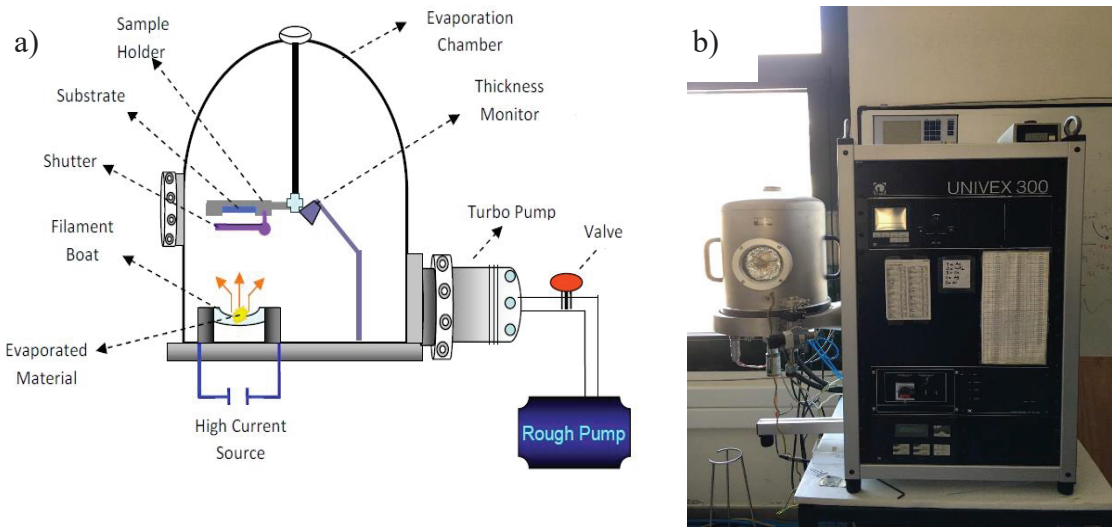

Figure 5.4. Thermal evaporation system a) inside view, b) outside view.

The current was 75 A for Ag material. Thickness of the Ag film was controlled by the shutter and it also ensured to obtain good quality Ag thin film on SLG/ITO/Zn(O,S)/Sb_2Se_3 structure. Evaporation rate was set to 1,5 Å per second. The thickness monitor was calibrated for Ag and the evaporated thickness of the Ag film was 200 nm.

5.5. Deposition of ITO Top Contact Layer

Since indium tin oxide (ITO) has satisfying properties like low electrical resistivity and high transparency at the solar spectrum region with respect to other transparent conducting oxide (TCO) materials, it has been extensively employed as transparent electrodes in PV applications (Demirhan et al. 2020). Therefore, for solar cell fabrication, ITO films with low electrical resistivity (Rs<10 Ω/sq.) were deposited as window layer (top contact) on SLG/Mo/Sb_2Se_3/CdS substrate structure by DC magnetron sputtering system. This system is a large version of the magnetron sputtering system which was used to grow Sb_2Se_3 and Zn(O,S) films. The image of the DC magnetron sputtering system is given in Figure 5.5 (a). Figure 5.5 (b) shows the plasma occurring during deposition process.

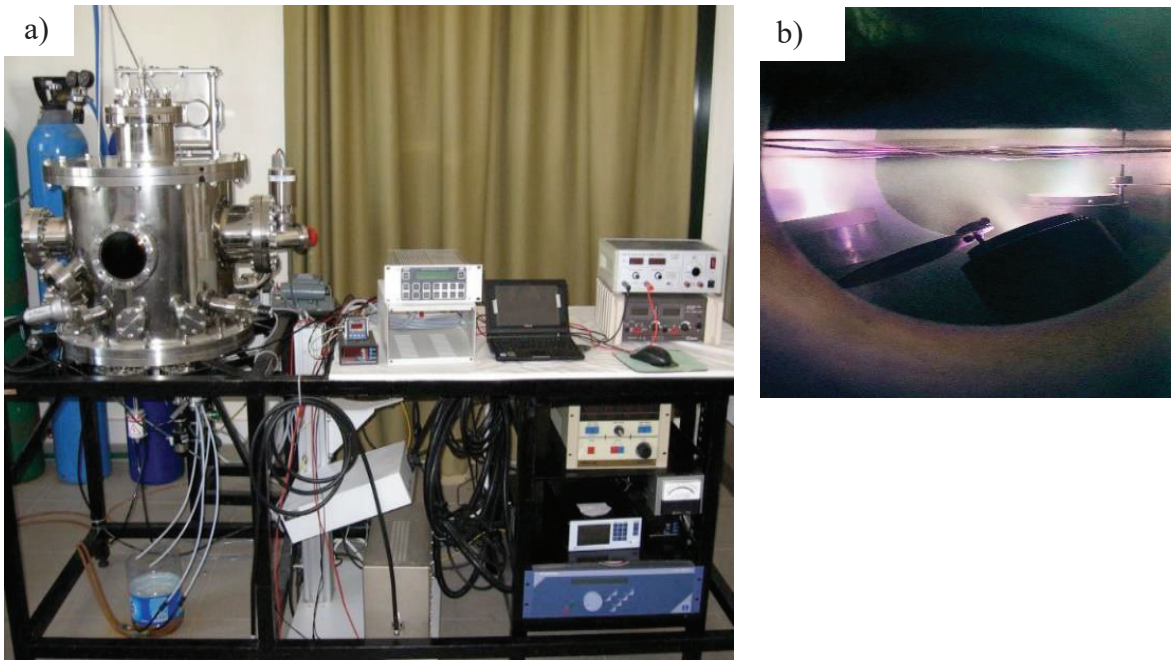

Figure 5. 5. a) DC magnetron sputtering system, b) The plasma during deposition.

The two-inch ITO target with a purity of 99.999% and a weight per cent of 10 to 90 for SnO_2 and In_2O_3, respectively, was used. The sputtering system equipped with a turbo molecular pump and a rough pump. The target-substrate distance was 7 cm. The

sputtering system chamber was evacuated to a base pressure of less than 2×10^{-6} Torr before starting deposition. The deposition was performed for 30 minutes, using 15-Watt DC power and 40 sccm Ar gas. ITO thickness was 200 nm for both single and buffer layered substrate solar cells.

5.6. Device Fabrication

In this thesis, a total of 4 solar cells were produced in two different configurations, two in the superstrate structure and the rest in the substrate structure. Detailed information will be given in the subsections.

5.6.1. Substrate Structure Device Fabrication

The substrate configured solar cell was fabricated on Mo coated soda-lime glass substrate. The Sb_2Se_3 absorber layer growth with a thickness of 500 nm is performed using 30-Watt RF power and 30 sccm Ar, as described in Chapter 5.1. Following deposition part, Sb_2Se3 film was heat treated at 350 ˚C with a ramping rate of 20 ˚C/min for 30 minutes under 100 sccm argon flow. Then, 50 nm CdS buffer layer was coated on the SLG/Mo/Sb_2Se_3 structure with chemical bath deposition technique as shown in Chapter 5.2. The cell was completed by depositing 200 nm ITO material (window layer) as the top layer by DC magnetron sputter. In the SLG/Mo/Sb_2Se_3/CdS/ITO solar cell structure, each layer has a different function in terms of the working solar cell. Figure 5.6 demonstrates the substrate structured device with CdS buffer layer.

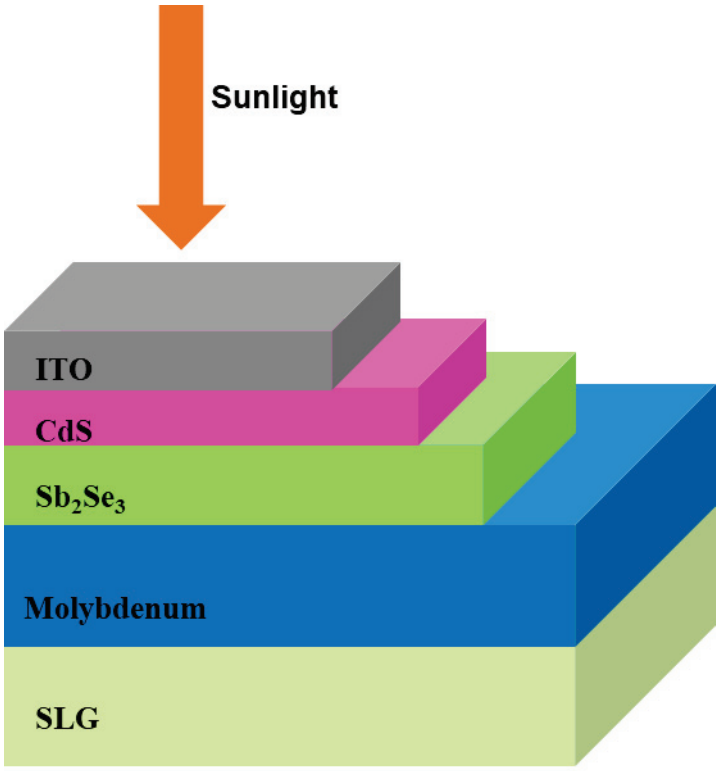

Figure 5.6. Device structure of Sb_2Se_3/CdS substrate solar cell.

5.6.2. Superstrate Structure Device Fabrication

The superstrate configured solar cell was fabricated on SLG/ITO substrate. The Zn(O,S) buffer layer growth with a thickness of 50 nm is performed using 40 Watt RF power and 50 sccm Ar, as described in Chapter 5.3. During the deposition 0.5 and 1 sccm O introduced to fabricate two different solar cells, respectively. Sb_2Se_3 thin film was deposited onto SLG/ITO/Zn(O,S) structure in the same sputtering system without breaking the vacuum. Sb_2Se_3 film thickness remained constant (500 nm) for both films. Following deposition part, SLG/ITO/Zn(O,S)/Sb_2Se_3 structure was heat treated at 350 ˚C with a ramping rate of 20 ˚C/min for 30 minutes under 100 sccm argon flow. Then, the cell was completed by depositing 200 nm metal (contact layer) by thermal evaporation (Chapter 5.4). In the SLG/ITO/Zn(O,S)/Sb_2Se_3/Ag solar cell structure, each layer has a different function in terms of the working solar cell. Figure 5.7 demonstrates the superstrate structured device with Zn(O,S) buffer layer.

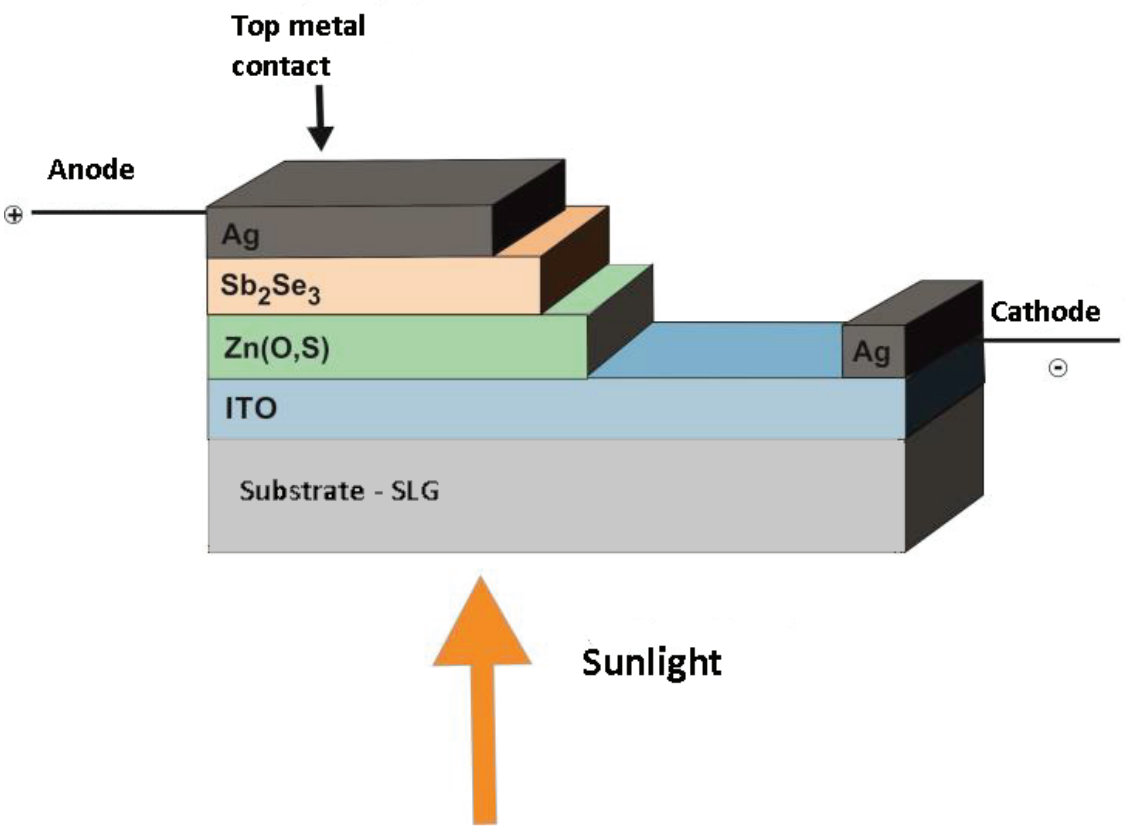

Figure 5.7. Device structure of Sb_2Se_3/Zn(O,S) superstrate solar cell.

5.7. Sample Characterization Methods

5.7.1. Profilometry

A profilometer is an instrument that uses a stylus to detect the film surface. It measures small surface variations (nanometer) in vertical direction as a function of position. A Veeco DEKTAK 150 profilometer was used to determine the thickness of all thin films used in the device fabrication Sb_2Se_3 solar cells. It is capable of measuring thickness ranging in height from 131 microns to less than 100 Angstroms on a wide variety of substrate surfaces.

5.7.2. Scanning Electron Microscopy (SEM)

Scanning Electron Microscopy (SEM) is a reliable technique to display the morphology of thin films and the interfaces between thin film layers. The operation principle of SEM is similar to optical microscope. In order to obtain images from the sample surface, focused electron beams are used instead of the light. Compared to an optical microscope, much larger magnifications (> 100 000 X) are possible to analyze the sample. A topography image of the sample surface is provided by scanning the sample with the focused electron beam.

In the present work, FEI-QuantaFEG 250 SEM was used to examine sample surface morphology. The surface topography of the films was imaged at 50 000 X magnification by using 15 kV acceleration voltage, 5 spot size and back-scattered electron detector (BSED) at 10 000 X magnification. In addition, surface images taken at 50 000 X magnification were measured by through-lens-detector (TLD) with 5 kV acceleration voltage and spot size 2.

5.7.3. Energy Dispersive X-Ray Spectroscopy (EDS)

Energy Dispersive X-Ray Spectroscopy (EDS) analyses enables to investigate the atomic composition of the sample. The working principle of the EDS is similar to SEM technique. The sample surface is exposed to focused electron beams, hence, an electron at the inner is excited. While ejecting it from the shell, an electron hole is created. This vacant shell is then filled up by an electron from an outer shell. Because of the energy difference between the inner and outer shells, specific energies in the form of an X-ray may be released. EDS calculates the number and energy of the X-rays emitted from a sample. Consequently, elemental composition of the sample can be analyzed since the energy of the X-rays are characteristic for each element.

EDS analysis of the thin films was performed by FEI-QuantaFEG 250 SEM equipped with Oxford X-act EDS. To define the atomic composition of the Sb_2Se_3 films, EDS measurements were taken with 15 kV acceleration voltage having 1000 X magnification with a 20 μm scaling under high vacuum (HV).

5.7.4. X-Ray Diffraction (XRD)

X-Ray Diffraction (XRD) is a powerful technique to specify atomic and molecular structure of a crystal. X-ray beam diffract into many specific directions in a crystalline material during the XRD measurement. From the angles and intensities of these diffracted beams, molecular structure of material can be identified.

In the present work, the X-ray diffractometer (XRD) system GNR, APD pro 2000 with a Cu $K\alpha$ radiation source (λ = 1.5406 A) with a step size of 0.1° and a step time of 1.0 s was used to determine the crystalline structures of the Sb_2Se_3 films.

5.7.5. Raman Spectroscopy

Raman spectroscopy is an effective spectroscopic technique to analyze vibrational modes of materials. The working principle relies on Raman scattering (inelastic scattering) of monochromatic light, generally from a laser source in the visible (390-700 nm), near infrared (700 nm-1400 nm) or near ultraviolet (300-400 nm) range. The frequency of the monochromatic light absorbed by the material changes after its interaction with the sample. The energy difference between the incident photons and those reemitted by the sample corresponds to the vibrational energy levels of the molecule diffusing. The analysis of the shift of the spectral lines can provide information about the chemical composition, molecular structure, and intermolecular interactions of the sample.

The microstructural characterization of the Sb_2Se_3 films were done at room temperature by using a high-resolution confocal micro-Raman spectroscopy (S&I, MonoVista, employing a Princeton Instruments, Acton SP2750 0.750 m Imaging Triple Grating Monochrometer) in the back-scattering geometry with a spectral resolution of about 1 cm^{-1}. As the Raman excitation source, an Ar laser operating at 514.0 nm and 100X objective, giving spot sizes near 3 μm in diameter were also employed at times to probe the vibrational modes of the Sb_2Se_3 films in order to analyze their compositional structure.

5.7.6. Spectrophotometry

Spectrophotometry device is used for the quantitative measurements of the reflection, absorption or transmission properties of a material as a function of wavelength. The transmission change with respect to the wavelength was determined with the measurements taken with the help of PerkinElmer Lambda 950 UV/VIS/NIR spectrophotometer for each solar cell layer.

In this thesis, to determine the electrical characteristics of grown films, Hall measurements were occurred at room temperature using NanoMagnetic instruments ezHEMS system. However, due to the inconsistent results, data is not shared here. Hall measurement system had software based on conductive materials, therefore, it can be the reason for the inaccurate results for our samples.

5.7.7. Device Characterization

The performance of Sb_2Se_3-based thin film solar cell devices, such as V_{oc}, I_{sc}, FF and cell conversion efficiency, was analyzed by current voltage (I-V) characterization. The current-voltage measurement was conducted through an IV sweep which is working with functional generator.

In this thesis, an AM 1.5 G solar simulator was used at 25 °C (Figure 5.8). The intensity of input light was 1 kW/m^2. Two Keithley 2182A nanovoltmeters were connected to a computer and controlled by LabVIEW program that contains serial instrument control, data analysis and data storage. Probes of one of the nanovoltmeter were connected to the front contact and the back contact of the Sb_2Se_3 solar cell to measure the device voltage. The probes of other nanovoltmeter were used to measure the current flowing out of the device. Illuminated I-V measurements were used to calculate the values of V_{oc}, I_{sc}, V_m, I_m, FF and solar cell conversion efficiency, while dark I-V measurements were used to determine loss parameters of solar cells such as R_s and R_{sh}. Figure 5.9 shows the device output power information under dark and illuminated condition.

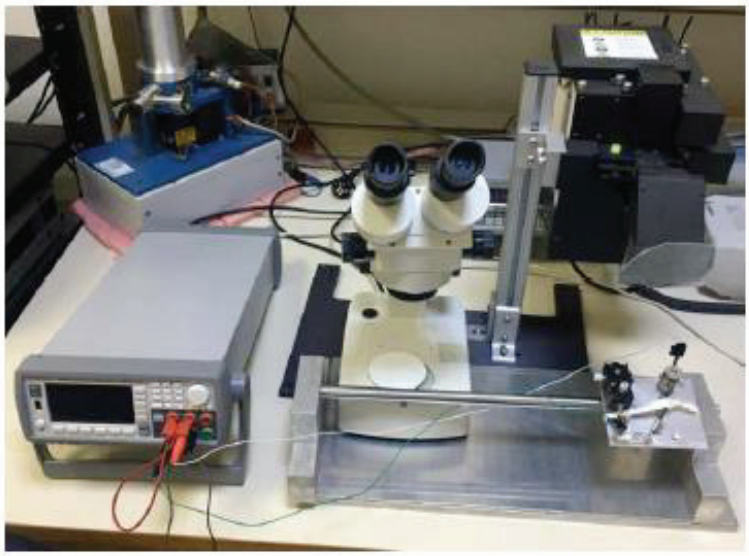

Figure 5.8. Solar Simulator.

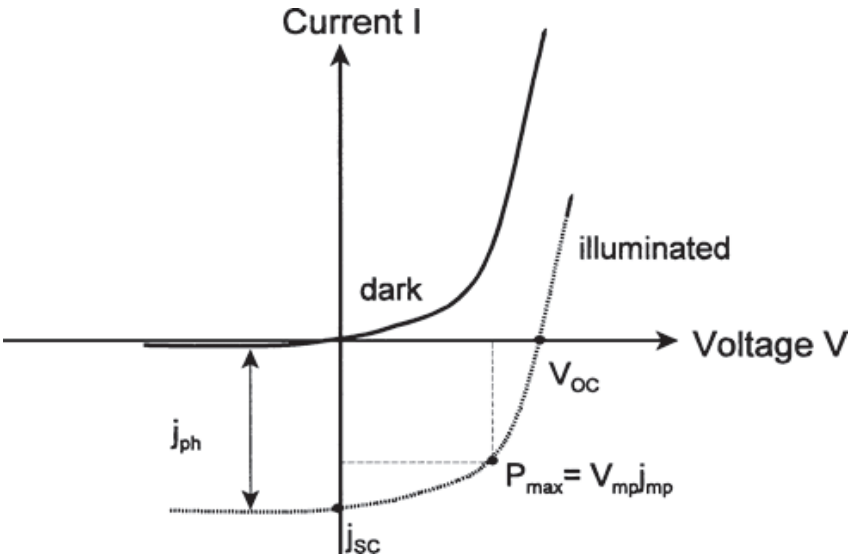

Figure 5. 9. I-V characteristics of a solar cell under dark and illuminated condition.
(Source: Karim et al. 2018)

CHAPTER 6

RESULTS & DISCUSSION

6.1. The Effect of Absorber Layer Thickness on the Structure and Optical Properties of DC Magnetron Sputtered Sb_2Se_3 Thin Films

In this section, Sb_2Se_3 films have been grown with DC magnetron sputtering method onto soda lime glass substrates with different time durations. Morphological, structural, and optical properties of Sb_2Se_3 thin films were systematically investigated as a function of the thickness for photovoltaic applications.

6.1.1. Film Preparation

P-type Sb_2Se_3 absorber layers were deposited by using the DC magnetron sputtering system. This DC magnetron sputtering system is visually presented in Figure 5.1. The Sb_2Se_3 absorber films were grown on a 1.1 mm thick soda lime glass using a 2-inch diameter and 99.999% purity Sb_2Se_3 sputtering target. At room temperature, a power of 20 Watt was applied, and the deposition was performed at different times: 5, 10, 15, 20 minutes respectively. Thickness measurements were obtained by the profilometer. Figure 6.1 shows the variation in the thickness of the Sb_2Se_3 films as a function of the deposition time.

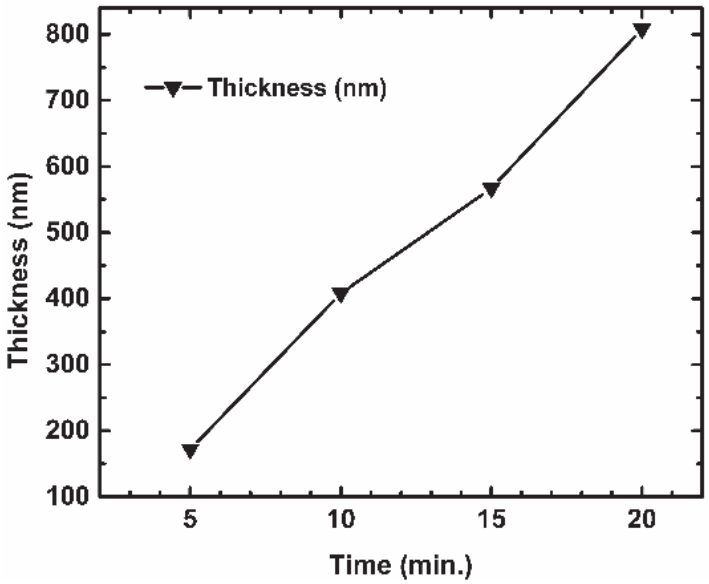

Figure 6.1. Variation in the thickness of the Sb_2Se_3 thin films as a function of the deposition time.

6.1.2. XRD Analysis of Sb_2Se_3 Films with Different Thicknesses

The binary compound Sb_2Se_3 has an orthorhombic crystal structure which belongs to the space group Pnma (62). To improve the performance of the solar cells, the control of the crystal orientation of Sb_2Se_3 films is a key factor. We used the XRD analysis to determine the crystal structure of the Sb_2Se_3 films obtained by the DC magnetron sputtering by using different growth times. According to the XRD spectra, at room temperature the sputtered Sb_2Se_3 condense on the substrate and form amorphous films. No crystalline phase was detected in Sb_2Se_3 films grown at room temperature. In terms of the XRD spectra given in Figure 6.2, the wide peak observed in the range of 25° - 35° belongs to the glass substrate. Due to the low mobility of the Sb and Se atoms, the Sb_2Se_3 thin films grown at room temperature are amorphous (G. X. Liang et al. 2018b). Moreover, the observation of amorphous structure can be attributed to the disorder which may be assigned to the introduction of some defects (Rabeh et al. 2014). The XRD analysis of Sb_2Se_3 thin films grown at room temperature shows that annealing is necessary for the films to develop a crystal structure.

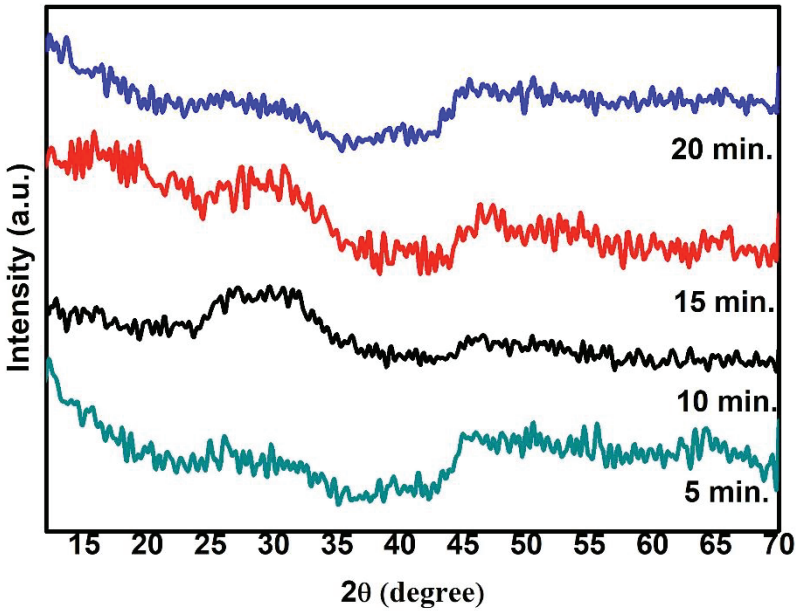

Figure 6.2. XRD analysis of Sb_2Se_3 thin films grown at room temperature with 20-Watt DC source.

6.1.3. SEM and EDX Analysis of Sb_2Se_3 Films with Different Thicknesses

The surface morphology of Sb_2Se_3 thin films grown at room temperature with DC sputtering, were analyzed by the SEM. The surface images of Sb_2Se_3 thin films with different thickness are presented in Figure 6.3. According to the primary SEM images, the surface of the films is observed to be smooth and featureless. On the other hand, the films grown on SLG substrates show good adhesion without visible mechanical defects such as cracks or erosions on their surfaces.

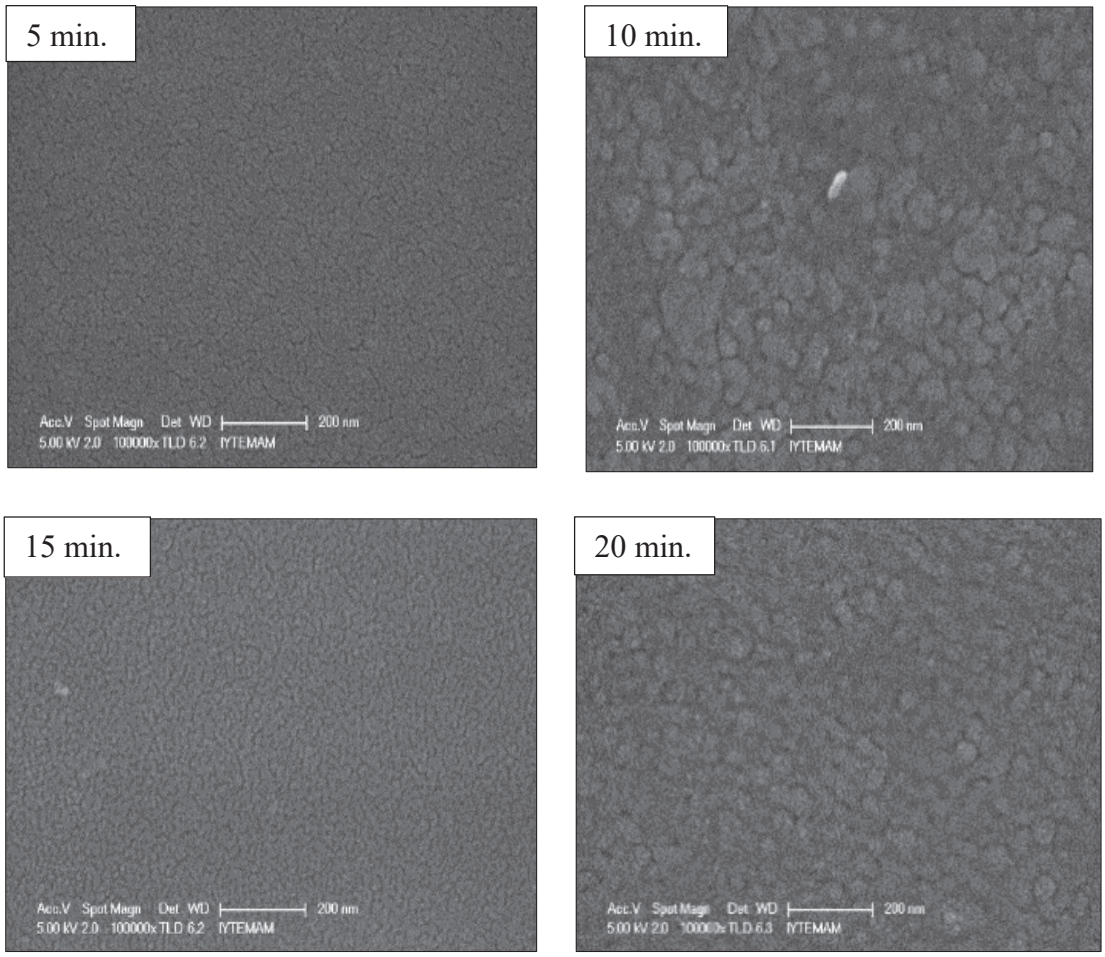

Figure 6.3. Grained surface images at 10 000 X magnification of the Sb_2Se_3 films with various growth times.

From the SEM surface images, partially granular structure was observed. From the Figure 6.3, this granular structure is more evident for the Sb_2Se_3 films deposited for 10 and 20 min. Figure 6.3 shows that the surface of Sb_2Se_3 films have homogeneous and small grain sizes of less than 100 nm. The grained structure is of great importance in solar cells. The grain boundaries serve as the junction center (recombination center) for electron-hole pairs, and it impacts the open circuit voltage (V_{oc}) of the solar cell. Therefore, large grain sizes will reduce the number of the grain boundaries and enable high values for V_{oc} by reducing the number of the junction centers for electron-hole pairs. Figure 6.4 shows SEM cross-sectional images taken at different magnifications for the Sb_2Se_3 film grown in 20 minutes by the DC magnetron sputtering method. As can be seen from these images, the sample surface has a smooth structure. For a 20 minutes' deposition, the film thickness was calculated to be between 793 to 769 nm. These values are very close to 800 nm, which was measured by profilometer.

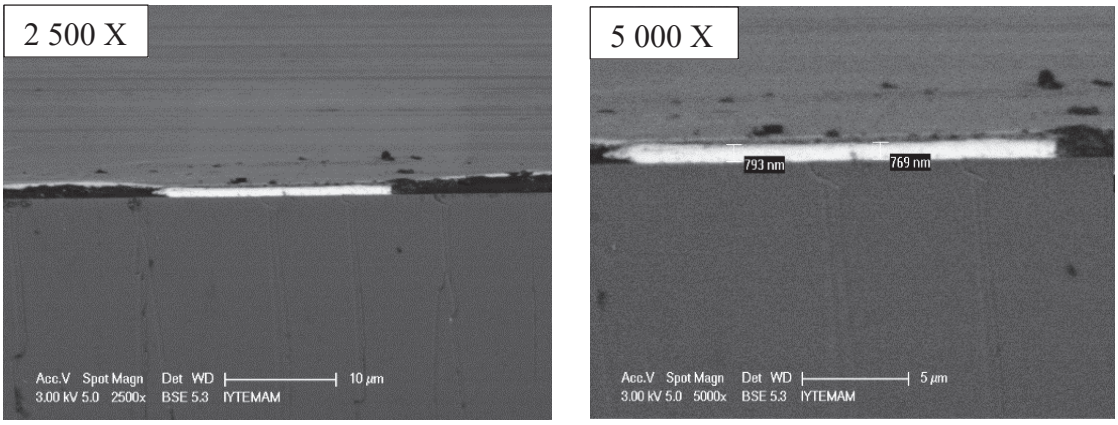

Figure 6.4. SEM cross-sectional images of Sb_2Se_3 thin films grown by DC magnetron sputtering system for 20 minutes.

The atomic concentration of Sb_2Se_3 films were determined by EDS analysis. In determining the atomic composition of the Sb_2Se_3 thin films, at least 3 points were measured from the film surface and averaged. The mean atomic percentages of the component elements Sb and Se are listed in Table 6.1.

Table 6.1. Average Atomic Concentration of the Samples.

Deposition Time (min.)	**Average Atomic %**			**Standard Deviation**
	Se	**Sb**	**Sb/Se ratio**	
5	69.82	30.18	0.43	0.17
10	63.06	36.94	0.59	0.08
15	63.69	36.31	0.57	0.06
20	63.68	36.32	0.57	0.13

For stoichiometric Sb_2Se_3 films, the atomic composition of Se and Sb elements are 60% and 40%, respectively. In this case, Sb/Se ratio value is 0.66. If this ratio falls below 0.66, the amount of selenium in this ratio is considered to be more than the stoichiometric ratio. Therefore, the compositions of these films are called in rich with selenium. According to Table 6.1, Sb/Se ratios of all Sb_2Se_3 films are lower than the stoichiometric value. This indicates the presence of excess selenium concentration. To

understand the composition variation in the film, the standard deviation of constituent elements has been calculated and given in Table 6.1. These standard deviations of constituent elements are not as high as to change the Sb/Se ratio from slightly selenium rich composition to the reverse. The Se-rich Sb_2Se_3 films are desirable for obtaining highly productive solar cells. Due to high vapor pressure of the Se element, Se vacancies may occur during the deposition (V_{Se}) and these vacancies act as deep recombination centers, thus causing a crystal defect in the film structure. This affects adversely the efficiency of the solar cell (Tang et al. 2019). When Table 6.1 is examined, we find a slight decrease in the selenium ratio for the deposition times over 5 minutes. The high saturation vapor pressure of Se and the different sputtering yield of Sb and Se are thought to decrease this ratio. The particles splashed from the Sb_2Se_3 target during the sputtering, may be partially broken down into antimony and selenium in plasma. Since selenium has a much higher saturation vapor pressure than antimony and Sb_2Se_3, it can be re-concentrated at a lower rate than antimony (Efthimiopoulos et al. 2013). The loss of Se during deposition may arise in the meantime. Although some amount of Se is lost, they still have a Se-rich composition. For deposition times over 5 minutes, there is no major differences in the film stoichiometry. Table 6.1 shows that Sb_2Se_3 films can be grown on the SLG substrates at room temperature by DC magnetron sputtering with a slight excess of Se composition.

6.1.4. Raman Analysis of Sb_2Se_3 Films with Different Thicknesses

The Raman Spectroscopy was used as an additional method to determine the phase purity of the Sb_2Se_3 films, the vibration modes, and the crystallization of molecules. Figure 6.5 shows Raman scattering spectrum of Sb_2Se_3 films grown at room temperature. Raman measurements were taken from at least 3 different points on the sample surface. Although there are many theoretically expected phonon modes for the Sb_2Se_3 compound (a total of 27 optical Raman modes), very few Raman peaks were observed in the previous studies (Shongalova, Correia, Vermang, et al. 2018). The Raman active bands observed at 67 and 72 cm^{-1} belong to rhombohedral selenium and are caused by the crystalline lattice vibrations (Nagata, Ishibashi, and Miyamoto 1981).

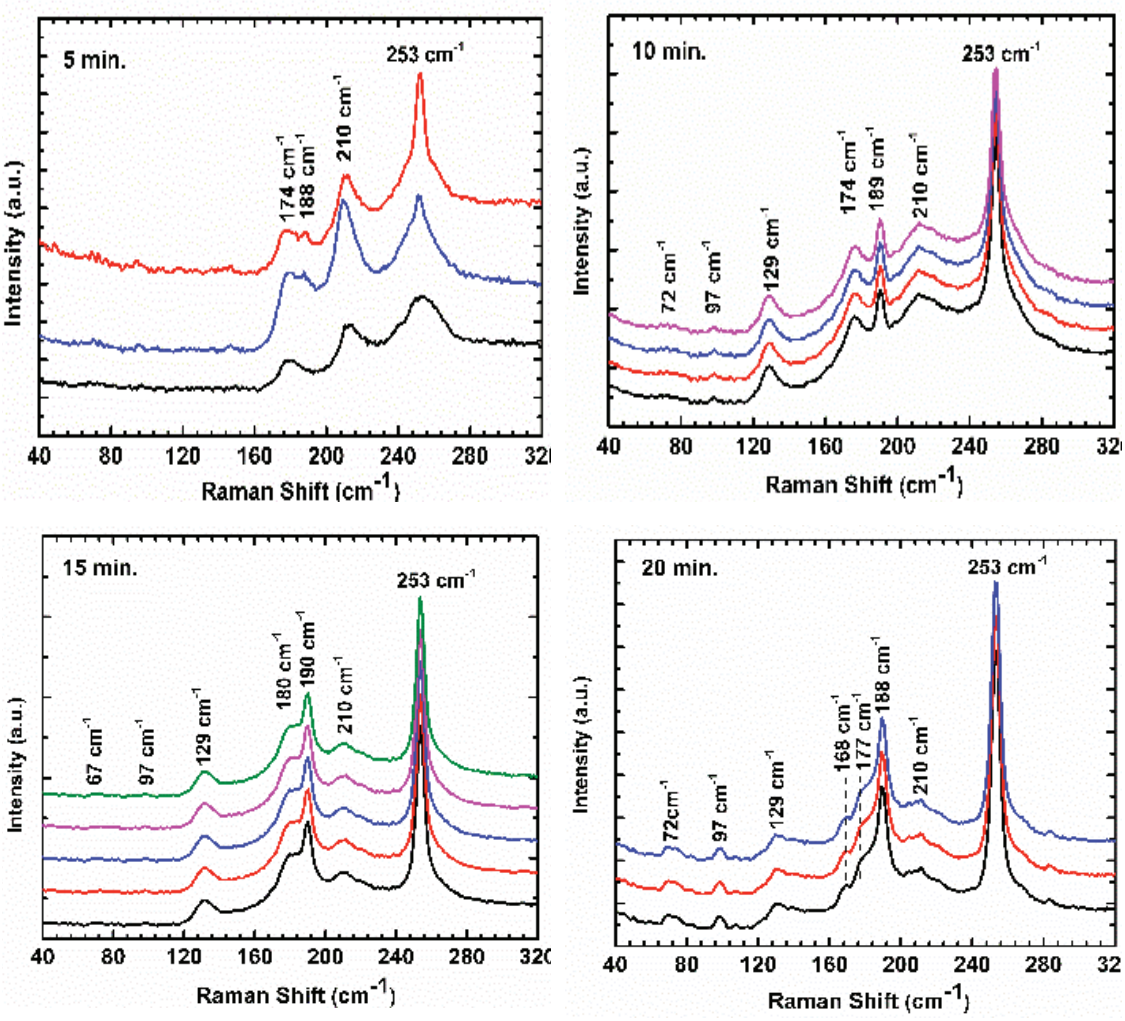

Figure 6.5. Raman scattering spectra of the Sb_2Se_3 films grown at room temperature with the DC power.

Another Raman peak observed at 97 cm^{-1} corresponds to a mode caused by the vibration of Se_8 ring molecules and has the E_1 symmetry (Nagata, Ishibashi, and Miyamoto 1981). The Raman peak which is observed at 129 cm^{-1} corresponds to the Raman mode of selenium E_3 (Nagata, Ishibashi, and Miyamoto 1981). These extra peaks of selenium were not observed in the Raman spectrum (Figure 6.5) of the film grown for 5 min. As the film thickness increases, the Se peaks became observable in the Raman spectrum. All films contain three characteristic Raman peaks of Sb_2Se_3, in the range of 188-190 cm^{-1}, at 210 and at 253 cm^{-1} as expected. The peaks observed in the range of 188-190 cm^{-1} and at 210 cm^{-1} are due to the Sb-Se vibration mode (Tao, Hu, Xue, et al. 2019; Z. Li et al. 2017b). The Raman peak, which is observed at 188-190 and 210 cm^{-1} and belongs to the Sb-Se vibrations, is called the A_{1g} mode (Browning et al. 2017). For the peak detected at 253 cm^{-1}, there are different considerations. According to literature,

this peak either belongs to selenium or antimony oxide. The Raman active peak of Se-Se vibrations, which is observed at 253 cm^{-1}, is also called A_{1g} mode (Shongalova, Correia, Vermang, et al. 2018). The Raman active modes of Sb_2Se_3 which we find at 168, 174, 177 and 180 cm^{-1} had not been reported previously. Even though Sb_2Se_3 is theoretically expected to have 27 Raman active modes, in previous experimental studies very few Raman peaks have been observed and reported in the literature. According to our investigation of the published literature, Sb_2Se_3 and Bi_2S_3 have the same structure, but more Raman active modes of qualified Bi_2S_3 material are reported experimentally (Yanyuan Zhao et al. 2011). If Sb_2Se_3 and Bi_2S_3 indeed have the same orthorhombic crystal structure, then we expect that the vibrational Raman peaks of these two compounds will have the same symmetry properties (Shongalova, Correia, Vermang, et al. 2018). For this reason, we think that the peaks observed at 168 and 174 cm^{-1} belong to the B_{1g} vibration mode of Sb_2Se_3, as in the case of Bi_2S_3 (Zhao et al. 2011). For the film deposited for 5 min, the characteristic Raman peaks of Sb_2Se_3 were not very intense and sharp. However, the number and the intensity of the Raman signals increased as the film deposition time was increased. Raman signal in thin films vary for several reasons, for example, film roughness, texture, crystalline nature, and thickness of film. Since Sb_2Se_3 thin films in this research have amorphous structure, crystalline nature cannot be reason for Raman signal intensity change. Raman scattering process takes place following three steps. Firstly, the incident laser beam excites the film. And then, the Raman-scattered light is generated from the film. Finally, this Raman light is collected. In case the thick film, the more laser beam is absorbed, and the more Raman-scattered light is generated which results the obtaining high intensity Raman signal from the film. Since a sufficient scattering volume would be necessary to get sufficient Raman signal, thickness might be a crucial reason of change in Raman signal in this work. Moreover, to get good vibrational-mode signal in the Raman spectra in thin film, thickness, and density of film as well as particle size should be high. Therefore, as the film thickness increased, both the Raman signal increased and some vibration modes began to be observed with increasing film thickness.

Various studies show that there is a relationship between the intensity rate of the Raman modes of the Sb-Se and Se-Se vibrations and the solar cell efficiency. In particular, it has been shown that decreases in $I_{(210)}/I_{(253)}$ and $I_{(210)} + I_{(188)}/I_{(253)}$ intensity rates of the characteristic Raman peaks of Sb_2Se_3 thin films result in higher efficiency for

the solar cells (Tao, Hu, Xue, et al. 2019; Z. Li et al. 2017b). Figure 6.6 shows the variation in intensity ratios of the characteristic peaks of Sb_2Se_3 thin films over coating time. The intensity ratios of both $I_{(210)} / I_{(253)}$ and $I_{(210)} + I_{(188)} / I_{(253)}$ calculated from the characteristic Raman peaks also decrease as the film deposition time increases. As seen in the Raman analysis given in Figure 6.5, the characteristic peak of Se-Se bonds that appears at 253 cm^{-1} is sharper and more severe as the deposition time increases due to the increased scattering cross-section.

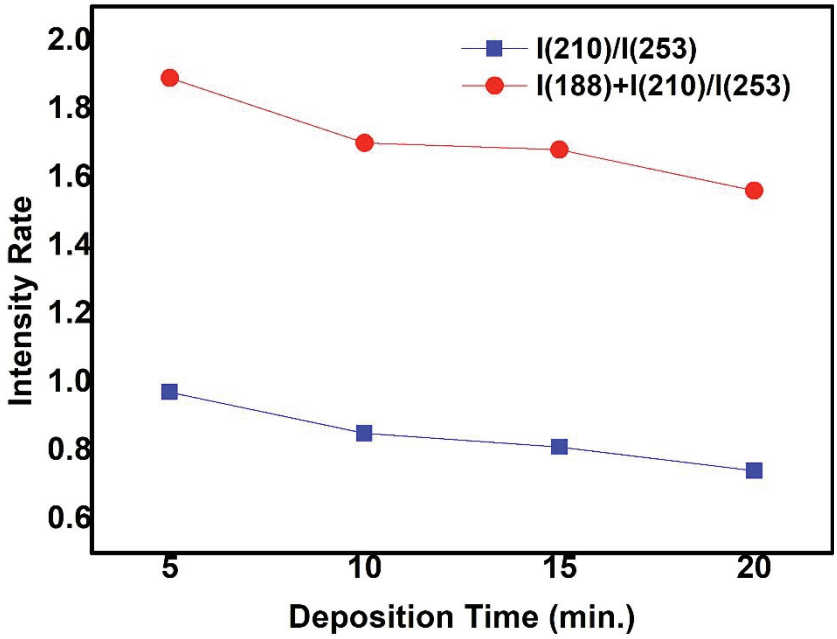

Figure 6.6. Raman peak intensity ratios of the Sb_2Se_3 films grown by DC magnetron sputtering plotted as a function of the deposition time.

6.1.5. Optical Analysis of Sb_2Se_3 Films with Different Thicknesses

Optical properties are also important in obtaining an efficient absorber layer, and hence an efficient solar cell. Figure 6.7 shows the optical transmittance of the films in the wavelength range from 200 nm to 1600 nm. As can be seen in this figure, the optical transmittance of the Sb_2Se_3 films grown at different times, is higher in the near-infrared region than in the visible region. This shows that Sb_2Se_3 films are infrared-transparent materials. Although 5 minutes deposited Sb_2Se_3 film shows a different behavior, the presence of the interference peaks towards large wavelengths had been generally

observed as the film thickness increased. The reason for this is that the defects in the film increase with the thickness and the increase in light scattering due to the increase in particle size (C. Liu et al. 2019). Since the optical absorption is largely dependent on these defects, they can affect the transition of the electrons (Turkoglu et al. 2019). Figure 6.7 represents the importance of thin film thickness. The variation in the film thickness leads to a shift in the optical absorption edge thus induces a change in the band structure of the film. This give rise to thought that the defects in the thin films form in the course of deposition of the films. For instance, because of an inadequate number of atoms, unsaturated bonds can be generated. These bonds are responsible for the generation of some defects which produce localized states in the optical bandgap of films (Ovshinsky and Adler 1978). Consequently, the optical absorption edge varies inversely with the width of these localized states in the optical bandgap (Sönmezolu et al. 2011). When the transmission measurements are compared, as the film thickness increases, the absorption edge shifts to higher wavelengths (red shift), indicating that the optical band-gap energy value becomes narrower. The values of the optical band-gap energy (E_g) of the Sb_2Se_3 films were obtained from the transmission analyses given in Figure 6.7. For the calculation of E_g value, Tauc method was used as had been given in Equation (6.1).

$$(\alpha h\nu) = A\left(h\nu - E_g\right)^m \tag{6.1}$$

Here, α is the absorption coefficient, h is the Planck constant, hν is the energy of the incident photon, A is a constant corresponding to the effective mass, E_g is the energy band-gap value, and m is the constant that determines the optical transition type. Since Sb_2Se_3 is a semiconductor material with transitions, m is equal to ½. By plotting $(\alpha h\nu)^2$ versus (hν), the bandgap energy of the Sb_2Se_3 films is obtained by the linear extrapolation to hν axis as shown in Figure 6.8.

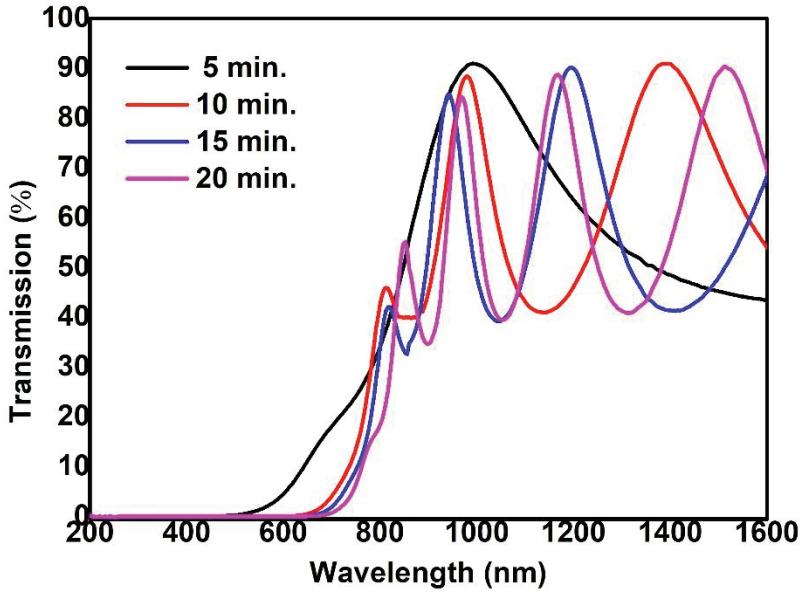

Figure 6.7. Transmittance of the Sb_2Se_3 films, which were grown at room temperature with DC power with different growth times, plotted as a function of the wavelength.

The variation of optical band-gap energies with respect to the Sb_2Se_3 film thickness is shown in Figure 6.9. The optical band-gap energies (E_g) for the samples with 5, 10, 15 and 20-minute deposition times were obtained as 1.78, 1.76, 1.75 and 1.70 eV, respectively. The variation trend of the optical band-gap energy values can be explained by the film thickness. The reduction in the film thickness indicates the increase in disorder within the film which might be assigned to the emerge of some defects which bring into localized states in the bandgap consequently increase the bandgap. There are similar results reported by other researchers (Sönmezolu et al. 2011; Ghasemi Varnamkhasti et al. 2012). Another reason for the decrease in optical band-gap energy value with the increase of thin film thickness is the possible increase in barrier height at the grain boundaries. The reason of this is the increase in the density of states localized near the band edge and consequently reduces the E_g with thickness (Aly and Akl 2015). As can be seen from Figure 6.9, the obtained range of the energy values are consistent with the literature. However, the theoretically calculated values for the energy band gap of Sb_2Se_3 films grown at room temperature are higher than what we found for our samples, because our films have amorphous structure as shown by the XRD analysis presented in Figure 6.2.

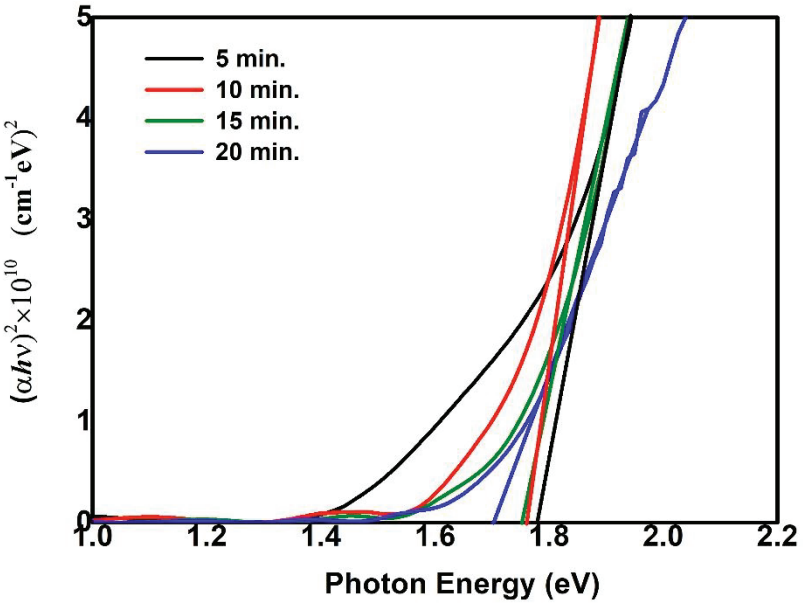

Figure 6.8. Determination of the optical band-gap energy of Sb_2Se_3 films grown at room temperature with DC power with different growth times.

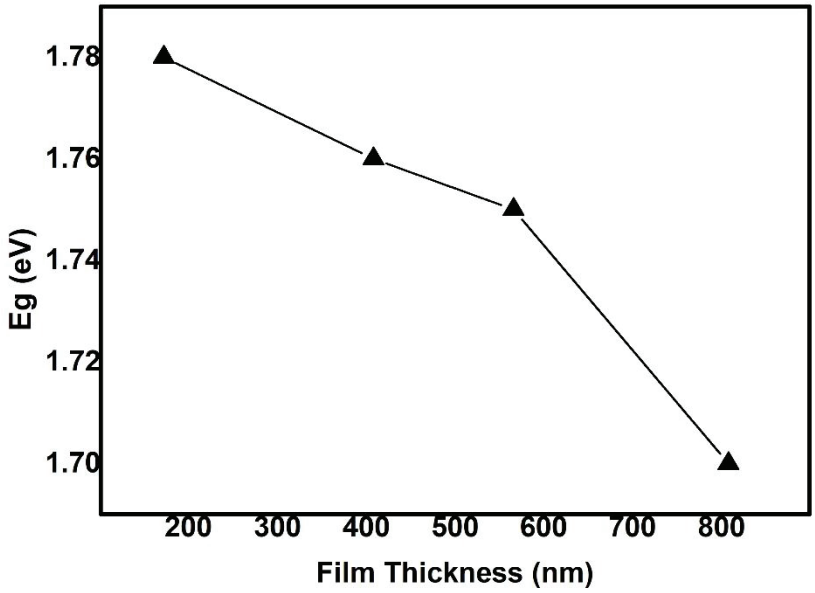

Figure 6.9. Band gap energy values variation with thickness of Sb_2Se_3 films grown at room temperature with DC power at different time periods.

6.1.6. Conclusion

Analytical results indicate that the optical transmission, absorption behavior, and bandgap energy are strongly dependent on the thickness of the film.

To conclude:

- The DC magnetron sputtering method was successfully used to fabricate Sb_2Se_3 thin films for solar cell applications.
- The samples deposited at room temperature have amorphous structure.
- The number and intensity of Raman peaks increased as the film deposition time increases.
- As the film thickness increases the absorption edge shifts to higher wavelengths (red shift) and the value of the band gap energy decreases.

6.2. The Effect of Ar Gas Flow Rate on the Structure and Optical Properties of Magnetron Sputtered Sb_2Se_3 Thin Films for Solar Cells

In this study, effects of argon flow rate on the properties of the Sb_2Se_3 films were investigated. The significance of argon flow rate, that used during film deposition, on the observing of Se loss, antimony oxide formation and the change in the surface morphology was also addressed. It is also reported that the dominant crystal orientation varied with respect to argon flow rate. It was further detected that high argon flow rates cause the decomposition of Sb_2Se_3 structure and the result the formation of antimony oxide phase. The overall analyses revealed that argon flow rate used while sputtering is effective in changing the structural and optical properties of the Sb_2Se_3 thin films.

6.2.1. Film Preparation

Sb_2Se_3 absorber films were grown on 1.1 mm thick soda lime glass (SLG) substrates using a 2- inch diameter and 99.999% purity Sb_2Se_3 binary target with RF

magnetron sputtering technique. The Sb_2Se_3 films were deposited using 6 different standard cubic centimeters per minute (sccm) argon (99.999 purity) flow increments. Argon gas flow rate was increased from 20 to 50 sccm. Mass flow controller was used to arrange the argon gas flow. Depositions were performed at room temperature using 30-Watt RF power for 20 minutes. After the deposition process, films were annealed in a Lindberg/Blue M tube furnace under Ar atmosphere (Figure 5.2). Heat treatment was applied for 30 minutes at 350 °C. After the annealing, the films were naturally cooled down. The grown Sb_2Se_3 films' names are numbered according to the increasing gas flow and are given in Table 6.2. Thickness of these Sb_2Se_3 absorber films were measured by profilometer after the sputtering process. Figure 6.10 depicts the variations of thickness as a function of argon gas flow. As seen from the Figure 6.10, fluctuations in argon gas flow have a slight effect on the film thickness. At low flow rates (up to 35 sccm), film thicknesses were higher due to the high deposition rates. As the gas flow is increased further which is accompanied by an increased pressure, thickness of the films started to decrease due to the reduction in the deposition rate (Ul-Hamid 2020). Similar result has been observed by Arshi et.al (Arshi et al. 2012)

Table 6.2. Deposition parameters of Sb_2Se_3 absorber thin films.

Samples	**Power (W)**	**Deposition Time (min.)**	**Ar Gas Flow Rate (sccm)**
Sb-20	30	20	**20**
Sb-25	30	20	**25**
Sb-30	30	20	**30**
Sb-35	30	20	**35**
Sb-40	30	20	**40**
Sb-45	30	20	**45**
Sb-50	30	20	**50**

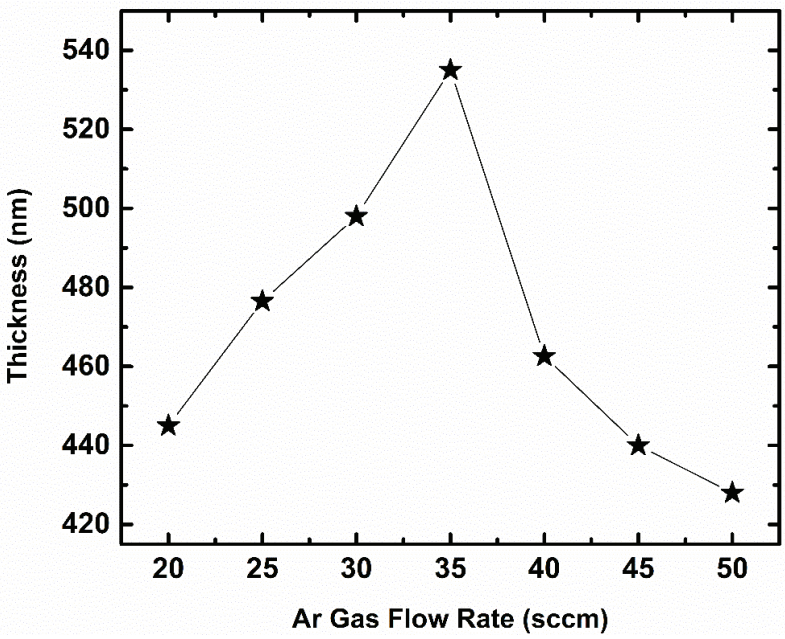

Figure 6.10. Variation in the thickness of the Sb_2Se_3 thin films as a function of the argon gas flow rate.

6.2.2. XRD Analysis of Sb_2Se_3 Films Grown at Different Argon Gas Flow Rates

Figure 6.11(a-g) shows the XRD patterns of Sb_2Se_3 films. It can be seen all films have polycrystalline structure and exhibit characteristic peaks of orthorhombic Sb_2Se_3 (JCPDS 15-0861). According to Figure 6.11(a-g), apparently dominant crystal face of Sb_2Se_3 varies with argon gas flow rate and the number of crystal faces changed with argon flow. The preferred orientation of a film is a result of the lowest total energy. This is a consequence of competition between the surface energy, the strain energy, and the stopping energy of different lattice planes. Therefore, argon gas flow rate affects the intensity of the crystallographic directions (Khojier et al. 2013). The peak we observed at 31.2 ° belong to the lattice plane (221) (Shen et al. 2018). The (221) orientation allows better carrier transport through the Sb_2Se_3 film. This crystal orientation also improves the diode quality and thus the device performance by providing less defects formation in the interface (Z. Chen et al. 2019; C. Chen, Bobela, et al. 2017).

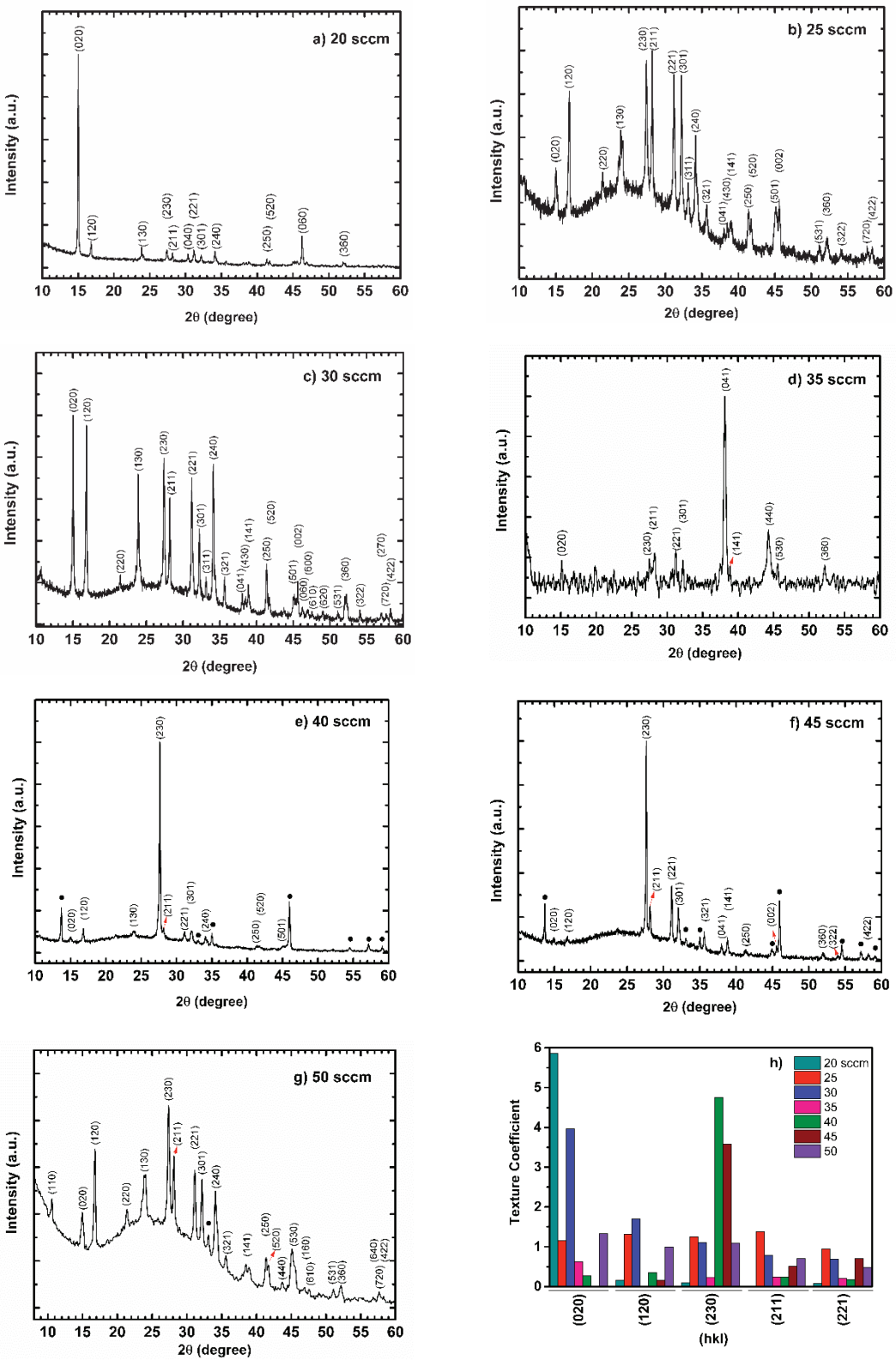

Figure 6.11. Normalized XRD analysis and texture coefficient of Sb_2Se_3 films deposited at different argon flow rate.

In the literature, it is seen that the efficiency values of Sb_2Se_3 based thin film solar cells are directly proportional to the intensity of the (221) peaks (Wen et al. 2018; Tao, Hu,

Xue, et al. 2019). Therefore, in this study, the purpose was to improve the intensity of the peak with (221) orientation. Among the Sb_2Se_3 films deposited using different argon flow rate, Sb-25 showed the highest intensity through the (221) orientation. In the meantime, it is important to say that the intensity of crystal face (120) is detrimental for solar cell performance because it increases the series resistance (Yuan, Zhang, et al. 2016; Z. Chen et al. 2019) which is also related with the argon flow rate. The (120) peak appears with the highest intensity for the film Sb-30 whereas it disappeared for the film Sb-35. To determine the preference orientation of Sb_2Se_3 films quantitatively, texture coefficients (TC) of the diffraction peaks were calculated according to following Equation 6(2):

$$TC_{(hkl)} = \frac{\frac{I_{(hkl)}}{I_0}}{\frac{1}{N}\sum_N \frac{I_{(hkl)}}{I_0}} \tag{6.2}$$

Where $I_{(hkl)}$ is the measured peak intensity of the (hkl) plane and $I_{0(hkl)}$ is the intensity in the standard XRD pattern of Sb_2Se_3 (JCPDS 15-0861). N is the number of reflections considered for the calculation (K. Nakamura et al. 2003). A large value of $TC_{(hkl)}$ for a relevant diffraction peak indicates a preferred orientation along this direction (Tang et al. 2019). The value of $TC_{(hkl)} = 1$ indicates a randomly oriented crystallite. In the abundance of crystallite orientation at the (hkl) direction, the value of $TC_{(hkl)}$ is greater than 1 (Babu, Dev, and Podder 2019; Caglar et al. 2009). The $TC_{(hkl)}$ values for the five major diffraction planes of (020), (120), (230), (211) and (221) are depicted in Figure 6.11-(h) for different argon flow rate. From the Figure 6.11-(h), it is obvious that the deviation of $TC_{(hkl)}$ from unity reveals the effect of argon flow rate on the formation of different diffraction planes. According to Figure 6.11-(h), the (211) and (221) planes have the highest value of $TC_{(hkl)}$ for the film Sb-25. $TC_{(hkl)}$ value of (020), (120) and (230) planes are calculated in the highest for the film Sb-20, Sb-30 and Sb-40, respectively. The means of larger $TC_{(hkl)}$ values is the enhancement of orientation in this direction. Also, it is clearly seen that the (hk0) plane was a dominant orientation with the highest $TC_{(hkl)}$ value for all Sb_2Se_3 films except Sb-25. It is known that the nucleation and final growth orientation effect the crystal orientations. The crystallographic orientation with the lowest surface energy determines the growth orientation. This is a result of that sputtering parameters affect the crystal

orientation of deposited film (Aryanto et al. 2019). In addition, from the XRD pattern given in Figure 6.11, the characteristic peaks of Sb_2O_3 phase (JCPDF # 071-0365) were observed for the films Sb-40, Sb-45, and Sb-50 (remarked by black dot in the XRD spectrum). The reason for the formation of oxide phases at high amounts of Ar gas is thought to be the partial decomposition of Sb_2Se_3 during sputtering. In the meanwhile, Sb_2Se_3 particles may have partially decomposed into antimony and selenium elements in the plasma. Hence, selenium may be concentrated on the film at a lower rate than antimony due to its higher saturation vapor pressure. When the sample is removed from the vacuum system, Sb atoms located on the sample surface are thought to form the Sb_2O_3 compound by combining with the oxygen in the air. As a result, it is thought that it would be more appropriate to sputter the Sb_2Se_3 films using low argon flows (25 sccm) to prevent the formation of Sb_2O_3 and to obtain the dominance of (hk1) direction which is preferred for PV applications.

6.2.3. SEM Analysis of Sb_2Se_3 Films Grown at Different Argon Gas Flow Rates

The top view images of Sb_2Se_3 thin films deposited at different argon flow rate are shown in Figure 6.12 (a-g). At low flow rates (for the film Sb-20 and Sb-25), the coating morphology contains flat features that formed parallel to the substrate. The size of these flat shapes decreases for the film Sb-25. This might be consistent with our XRD data as the texture coefficient of the (020) decreased when the argon flow rate increased from 20 to 25 sccm. As the gas flow is increased further, the flat feature morphology starts to disappear and is replaced by granular structure. The grain boundaries appeared clearer in sample grown with 30 sccm Ar flow rate. An increase in the flow rate makes the grainy structure narrower for the film Sb-35. When the argon flow rate was as high as 40 sccm, the morphology of the film obviously changed. Unusual surface morphology was detected for the films Sb-40 and Sb-45. White bright crystal structures were observed on the film surface and embedded in the film. These shapes belong to the Sb_2O_3 formation which is also supported by XRD pattern of Sb-40 and Sb-45 films. To determine the atomic compositon of this structure, point EDS analysis was taken and given in Figure 6.13. According to point EDS analysis, this white crystal structure contains 43 % Sb and

57 % O elements as listed in Table 6.3. As well as the composition, the shape of this structure support the Sb_2O_3 formation (Z. Zhang, Guo, and Wang 2001). The reason why oxide phases are observed in films grown using high amounts of Ar is the partial decomposition of Sb_2Se_3 during sputtering. While sputtering process, the particles scattered from the Sb_2Se_3 target may have partially decomposed into antimony and selenium elements in the plasma. Selenium may be concentrated on the sample at a lower rate than antimony due to its higher saturation vapor pressure (X. Liang et al. 2019). As a result, Sb atoms partially present on the sample surface are thought to form the Sb_2O_3 structure by combining with the oxygen in the air when the samples are removed from the system. The surface images of Sb-40 and Sb-45 films are very similar. This may be that the $TC_{(hkl)}$ value of the (230) orientation is the highest in the crystal structure of both films. For the Sb_2Se_3 film deposited using 50 sccm argon flow, it displayed a compact and smooth morphology. There are some white bright points on the sample surface which indicates oxide phases. However, the oxide phase population formed in the Sb-50 is less than that of Sb-40 and Sb-45. This is confirmed by the XRD pattern of Sb-50 which represents only one crystal direction belongs to the oxide phase. According to surface topography of Sb_2Se_3 films given in Figure 6.12, the argon flow rate used during sputtering process plays an important role for the change of surface morphology. The chemical composition results of the Sb_2Se_3 thin films analyzed by Energy Dispersive X-ray Spectroscopy (EDS) are listed in Table 6.4. Sb_2Se_3 films have a stoichiometric composition when the Sb/Se atomic ratio is 0.66. If this ratio falls below 0.66, the composition deviates from stoichiometry and absorber layer becomes rich in Se element. The Sb/Se ratio gradually increases with the argon flow rate up to 30 sccm. The partial decomposition of Sb_2Se_3 in the plasma with the increase in argon flow, and the different sputtering yields between Sb and Se might have caused the change in film stoichiometry. The films deposited using 40 and 45 sccm argon flows suffered most seriously about Se-deficiency among all films. The significant increase in antimony composition for the films Sb-40 and Sb-45 resulted the formation of antimony oxide phase within the structures which is confirmed with XRD and SEM analyses. Although the atomic composition of Sb-50 is close to the stoichiometry, it has an oxide phase locally on the film surface which was identified by XRD and SEM analyses.

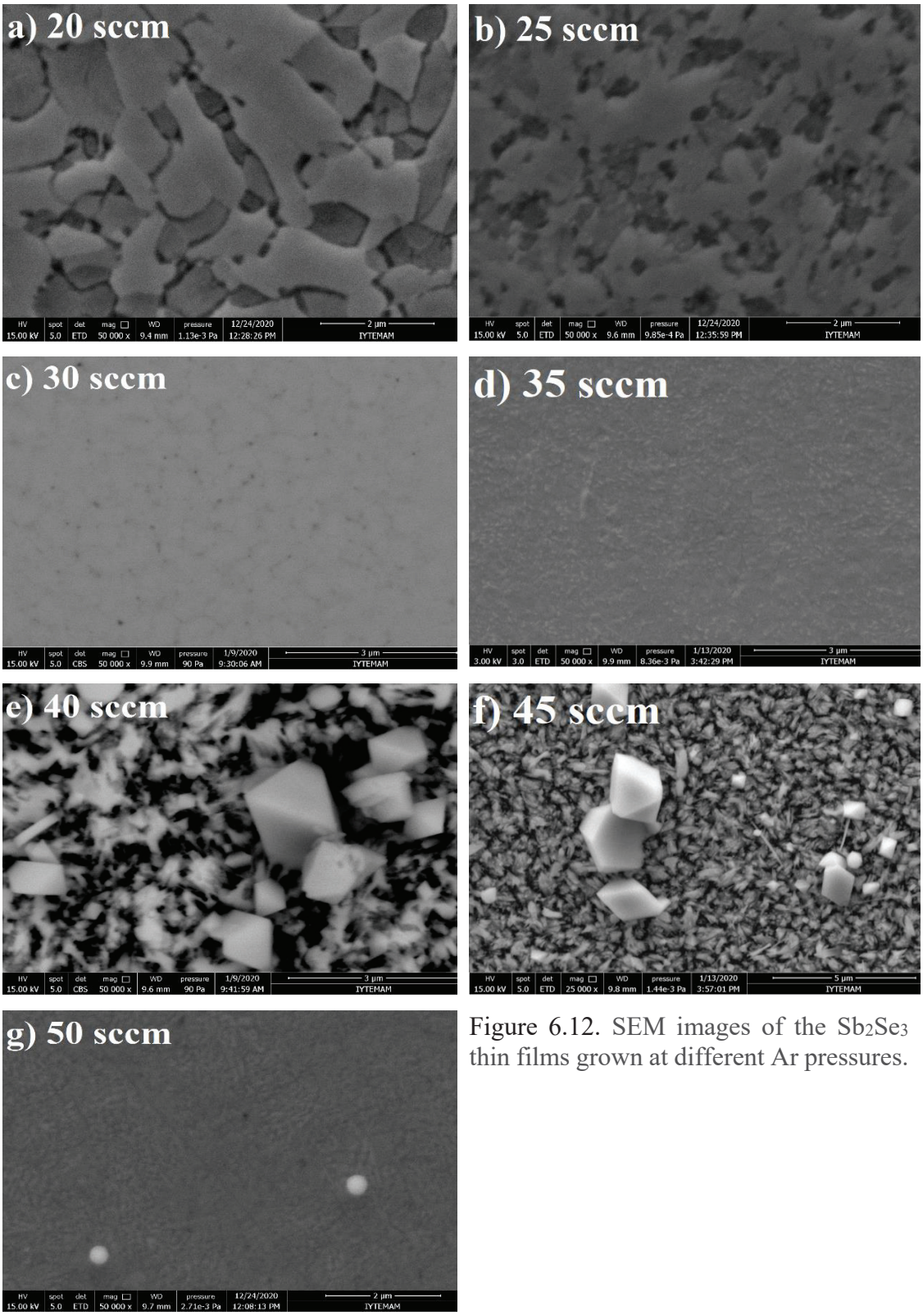

Figure 6.12. SEM images of the Sb_2Se_3 thin films grown at different Ar pressures.

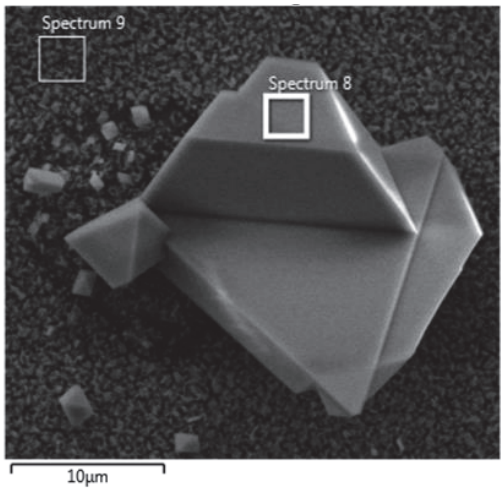

Quantitative analysis of Spectrum 8

Element	Atomic %
Sb	43
O	57
Total	100

Figure 6.13. Point EDS analysis of the Sb_2O_3 compound.

The amount of selenium of absorber film is important for the PV applications. High amount of selenium increases the p-type conductivity of Sb_2Se_3. In the case of selenium poor composition, selenium vacancy defects decrease the performance of solar cells (Tang et al. 2019). Under these circumstances, for PV applications Sb_2Se_3 absorber films should be deposited using argon flow under 40 sccm.

Table 6.3. Atomic composition of Sb_2Se_3 thin films grown with different Ar flow rate.

Ar flow rate (Sccm)	Atomic %		
	Se	Sb	Sb/Se ratio
20	60.60	39.40	0.65
25	60.11	39.89	0.66
30	59.84	40.16	0.67
35	60.84	39.16	0.64
40	55.17	44.83	0.81
45	48.97	51.03	1.04
50	60.36	39.64	0.65

6.2.4. Raman Analysis of Sb_2Se_3 Films Grown at Different Argon Gas Flow Rates

The Raman Spectroscopy was performed to identify main and secondary phases of Sb_2Se_3 films. In Figure 6.14, we present the Raman spectra of Sb_2Se_3 films, deposited using different argon flow rate. All films exhibited the characteristic Raman peaks of orthorhombic Sb_2Se_3 structure at 190 and 210 cm^{-1} assign to A_{1g} modes of Sb-Se vibration (Shongalova, Correia, Vermang, et al. 2018; Tao, Hu, Xue, et al. 2019; Z. Li et al. 2017b; Browning et al. 2017; Nagata, Ishibashi, and Miyamoto 1981). The secondary band originated from B_{1g} vibration mode of orthorhombic Sb_2Se_3 structure was detected between 169 and 171 cm^{-1} (Yanyuan Zhao et al. 2011). However, there are different considerations for the peak observed at 253 cm^{-1}. According to literature, this peak either belongs to selenium or antimony oxide. When high laser power density is used or the laser is dropped on the same point for a long time, the laser induced degradation of Sb_2Se_3 can occur (Shongalova, Correia, Vermang, et al. 2018; Chong Wang et al. 2020). This may be the reason of detection of oxide peak at 253 cm^{-1} for the films of Sb-20, Sb-25, Sb-30 and Sb-35. The intensity of this peak was observed to be high on Sb-40, Sb-45, and Sb-50 films. The reason for this is that the oxide phases determined by XRD and SEM analyses are already present in the structure of these films. The other oxide peak refers to Sb_2O_3 phase was detected at 450 cm^{-1}. This peak was observed more prominently in Sb-40, Sb-45, and Sb-50 films due to the presence of oxide phase detected by XRD and SEM analysis. It is known that quality of overall crystalline is closely related with the intensity and the sharpness of Raman peaks (Chong Wang et al. 2020).

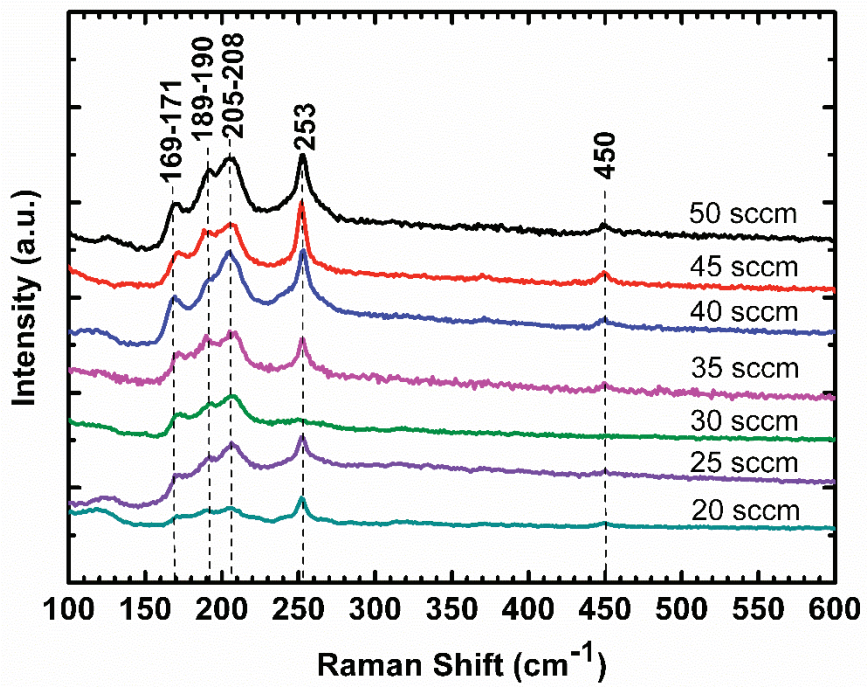

Figure 6.14. Raman scattering spectrum of Sb_2Se_3 films grown at different Ar gas flow rates.

6.2.5. Optical Analysis of Sb_2Se_3 Films Grown at Different Argon Gas Flow Rates

The band-gap energy values of (E_g) the Sb_2Se_3 films were obtained from the transmission measurements given in Figure 6.15 (a). For the calculation of E_g, Tauc method was used as had been given in Equation (6.1). By plotting $(\alpha h\nu)^2$ versus ($h\nu$), the bandgap energy of the Sb_2Se_3 films is obtained by the linear extrapolation to $h\nu$ axis as shown in Figure 6.15 (b).

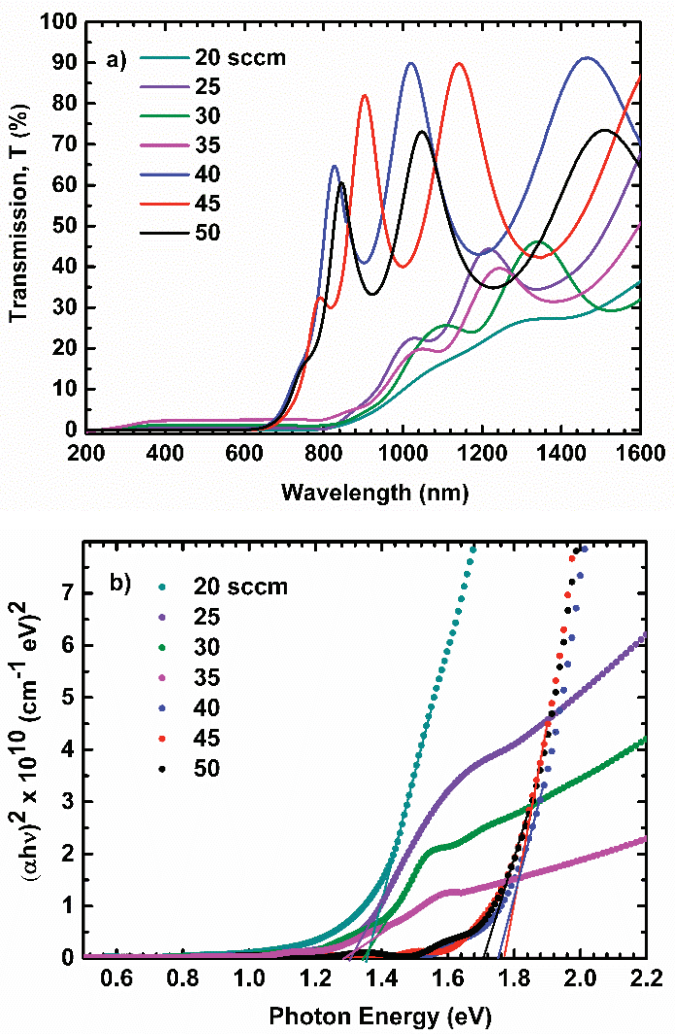

Figure 6.15. a) Transmission and b) optical band gap energy values of Sb_2Se_3 films grown at different Ar gas flow rates.

According to the Figure 6.15 (a), not only the transmission of films in the visible region showed variation but also the absorption edge of the films shifted. While the absorption edge of the films which grown with 40, 45 and 50 sccm Ar was observed in the low wavelength region, the absorption edge of the films which grown with 20, 25 and 30 sccm Ar was observed in the high wavelength region and the E_g decreased. The reason for this shift can be attributed to the antimony oxide phase which was detected for the films grown using argon over 35 sccm. This oxide compound was also observed in XRD and SEM analyses of related films. Since Sb_2O_3 has a high band gap energy (E_g = 3.6 eV) (Song et al. 2017), it also increases E_g value of the Sb_2Se_3 films on which it has been formed. In addition, the different dominant crystal orientation of films grown at different argon flow rates has also changed the bandgap energy as well as transmission. The E_g values of the

Sb_2Se_3 films grown at different Ar gas flow rates are listed in Table 6.4. It seems obviously that, the existence of oxide phase changed the E_g value. In photovoltaic applications, high E_g value causes the less absorption of the incident light, thus reduces the efficiency of the solar cell. For this reason, argon flow should be used below 40 sccm when depositing Sb_2Se_3 films with magnetron sputtering technique.

Table 6.4. Bandgap (E_g) values of the Sb_2Se_3 films grown at different Ar gas flow rates.

Ar flow rate (sccm)	**E_g (eV)**
20	1.35
25	1.30
30	1.34
35	1.28
40	1.75
45	1.77
50	1.70

6.2.6. Conclusion

In order to conclude Ar gas flow rate effect on the physical and optical properties of Sb_2Se_3 films:

- The RF magnetron sputtering technique was successfully used to fabricate Sb_2Se_3 thin films.
- Variation in sputtering gas flow rate had a slight effect on the film thickness.
- Ar gas flow rate changed the preferred orientations of films (crystal structure).
- The oxide phase (Sb_2O_3) was observed in the films grown with 40 sccm and above Ar gas.
- Surface morphology of films changed in shape depending on argon flow rate.
- E_g value changed depending on Ar gas flow rates.

6.3. The Effect of Post-Process Annealing Temperature on the Physical Properties of Sb_2Se_3 Thin Films

In this section, Sb_2Se_3 thin films were sputtered by DC magnetron sputtering technique at room temperature. Afterwards, the post- annealing process was applied on these films in a quartz tube under Ar atmosphere. As known, the post annealing studies about DC sputtered grown Sb_2Se_3 films in a quartz tube under Ar atmosphere have not been studied yet. Therefore, using a different Sb_2Se_3 growth technique followed by a post annealing process has been aimed in this study to investigate the dependence of physical properties on post annealing temperature for photovoltaic applications of Sb_2Se_3.

6.3.1. Film Preparation

A two-step process was used to fabricate Sb_2Se_3 absorber films during this study. In the first stage, Sb_2Se_3 films were deposited on soda lime glass (SLG) substrates by DC magnetron sputtering technique at room temperature from a 2-inch Sb_2Se_3 (99.999%) target. Vacuum chamber was evacuated by Turbo Molecular Pump (TMP). The background and operating gas pressure were approximately 4.5×10^{-6} and 1.2×10^{-3} Torr, respectively. 30 standard cubic centimeters per minute (sccm) Ar was used as sputtering gas and the deposition was conducted at 20 W power, while the deposition time was fixed to 10 min. Film thickness was 500 nm for all samples. In the second stage, DC magnetron sputtered grown Sb_2Se_3 films were exposed to post annealing process under 100 sccm Ar gas flow by means of a 70 cm long quartz tube in a furnace. The temperature ramping rate was kept constant at 20 °C/min for all samples. 150, 200, 250, 300, 350, 400 and 450 °C were chosen for post annealing process temperatures and the annealing duration was kept constant as 30 min.

6.3.2. XRD Analysis of Sb_2Se_3 Films Annealed at Different Temperatures

The variations in crystal structure, and lattice parameters with respect to post annealing temperature were examined by means of XRD. Figure 6.16 shows XRD pattern of as grown and post annealed Sb_2Se_3 thin films. It can be seen that the sputtered grown Sb_2Se_3 thin film at room temperature was condensed on the substrate as amorphous thin film. It is obvious from Figure 6.16 that the post annealing enabled as-grown film to crystallize. Furthermore, all peaks extracted from XRD spectra are characteristic peaks corresponding to orthorhombic Sb_2Se_3 (JCPDS 15-0861). It is seen from XRD pattern of post annealed Sb_2Se_3 films, the dominant orientation in the crystal structure changes with respect to annealing temperature. It can be easily inferred from the variation in the superiority of crystal direction that the crystal structure of Sb_2Se_3 thin films is closely related to the annealing temperature. The diffraction peaks observed at 28.2 and 31.2° belong to lattice planes (211) and (221), respectively (Shen et al. 2018).

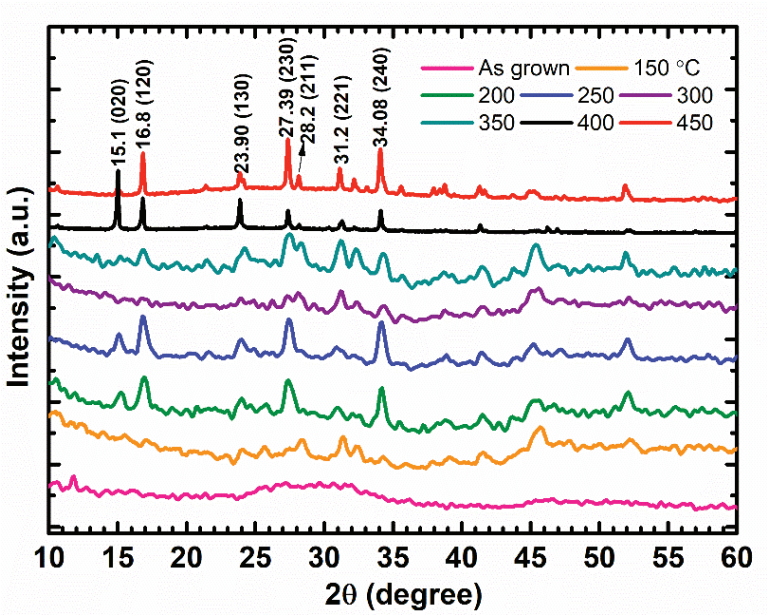

Figure 6.16. XRD analysis of as grown and post annealed Sb_2Se_3 thin films.

Figure 6.17 (a-b) shows normalized XRD analysis of annealed Sb_2Se_3 thin films in the small ranges. The normalized XRD analysis of annealed Sb_2Se_3 thin films at

different temperatures in the range of 2θ from 14 to 20° is shown in Figure 6.17 (a), while from 25 to 32° is shown in Figure 6.17 (b).

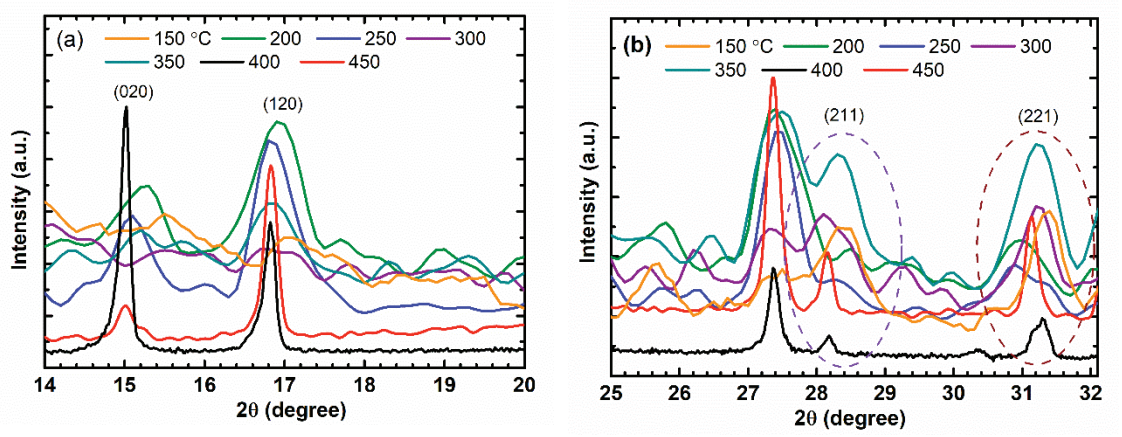

Figure 6.17. normalized XRD analysis of annealed Sb_2Se_3 thin films in the small ranges.

According to Figure 6.17 (a), the intensity of diffraction peak through (120) direction is high for 200, 250, 400 and 450°C heat treated films, while it is the lowest range for the films annealed at 150 and 300 °C. The peak observed at 15.1° corresponds to (020) diffraction plane (JCPDS 15-0861) and it has the highest intensity for the film annealed at 400 °C. In Figure 6.17 (b), the peak detected at 31.2° which belongs to (221) diffraction plane was observed with high intensity for the films annealed at 300, 350, 400 and 450 °C. A similar situation was encountered for the diffraction peak appeared at 2θ =28.2° matching with (211) plane, which defines the level of PV efficiency of orthorhombic Sb_2Se_3 (Ju et al. 2020). By increasing the post annealing temperature up to 350 °C, the favorable crystal orientations of (211) and (221) get stronger. To better understand the annealing effect on the crystal structure, the lattice constants of the films were evaluated from the results of the XRD analysis. For an orthorhombic crystal, the interplanar spacing (d_{hkl}) can be expressed by the Equation (6.3) given below (Ren et al. 2020).

$$\frac{1}{d_{hkl}^2} = \frac{h^2}{a^2} + \frac{k^2}{b^2} + \frac{l^2}{c^2} \tag{6.3}$$

Where, h, k, l are Miller indices and a, b, and c are lattice constants of crystal phase (Zhu et al. 2019). The lattice parameters were calculated using the first order reflection on the (230), (240) and (211) planes which were observed in all films. Variation in the magnitudes of lattice parameter is displayed in Figure 6.18. From temperature 150 to 250 ˚C, the increase in values of 'b' and 'c' along with a decrease of 'a' were detected. This trend reversed for the case of sample annealed at 300 ˚C. With further increase in annealing temperature, the values of 'b' and 'c' continued to increase and that of 'a' continued to decrease. Similar trend was detected for the formation of diffraction peak along (120) direction. The intensity of this peak increased from 150 to 250 ˚C, and then disappeared for the film annealed at 300 ˚C. And this peak started to appear again for the film annealed at 350 ˚C and get stronger for further annealing temperature.

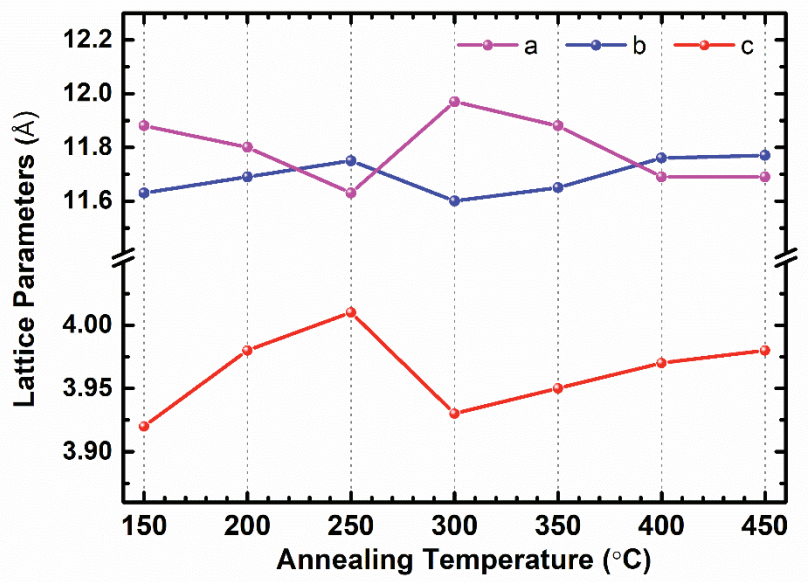

Figure 6.18. Variation in the magnitudes of lattice parameter.

The variation in lattice parameters with annealing temperature is thought to be the effect of reorientation of the microstructure. The change in the intensity of crystal directions in Figure 6.17 (a) and (b) support the variation of crystal parameters. Moreover, the decrease in lattice parameters may be due to the effect of stress undergone by thin film grains (Usseinov et al. 2014). However, the calculated parameters were close to the standard cell parameters a= 11.63 Å, b= 11.78 Å, and c= 3.99 Å as given in the Joint Committee on Powder Diffraction Standards (JCPDS) 15-0861 document. The average

crystallite size (D) of the Sb_2Se_3 films was estimated from the Debye-Scherer Equation (6.4) (Scherrer 1918).

$$D = \frac{K\lambda}{\beta\cos\theta} \tag{6.4}$$

Where λ is the wavelength of CuKα (1.54 A°), θ is the Bragg diffraction angle, β is defined as the full width at half maximum intensity (FWHM) of the x-ray peak on the 2□ axis and K is the Scherer constant which depends on the crystallite shape and the size distribution (Langford and Wilson 1978). In this paper K = 0.9 was used to estimate the average crystallite size (Uvarov and Popov 2013). Since the accurate value of the constant K is unknown for the present system, the calculated D values are only estimates. The average crystallite size calculations were occurred for the (120) and (211) diffraction planes which are important diffraction planes for photovoltaic applications and listed in Table 6.5. Since the (120) and (211) diffraction planes were not detected for some films, the structural parameters of the related peak could not be calculated.

Table 6.5. Diffraction planes for the orientations of (120) and (211).

T_a (˚C)	**(120) diffraction plane**		**(211) diffraction plane**	
	***d* (Å)**	***D* (nm)**	***d* (Å)**	***D* (nm)**
150	-	-	3.1411	13
200	5.2416	14	-	-
250	5.2488	15	-	-
300	-	-	3.1648	11
350	5.2631	13	3.1619	16
400	5.2667	45	3.1629	50
450	5.2668	53	3.1652	80

Here T_a is annealing temperature, d is interplanar spacing, D is average crystallite size. The data of JCPDS (00-015-0861): 2θ=16.874˚, d=5.2500 and 2θ=28.200˚, d=3.1620

Similar with the change in the intensity of the peak at (120) direction, the crystallite size increased from 150 to 250 ˚C annealing temperature. Since the peak was not observed in this orientation at 300 ˚C, the crystallite size could not be calculated. Increase in crystallite size was observed from 350 to 450 ˚C annealing temperature for (120) crystal orientation. Since the diffraction plane (211) was not detected for the films annealed at 200 and 250 ˚C, the crystallite size through this direction could not be calculated. It can be concluded from XRD spectrum that the post annealing temperature has noticeable effect on the direction related growth of Sb_2Se_3 thin films.

6.3.3. SEM Analysis of Sb_2Se_3 Films Annealed at Different Temperatures

Surface morphology of as grown and heat treated Sb_2Se_3 thin films are demonstrated in Figure 6.19 (a-g). The surface image of as grown film which contains many small granular structures can be seen from Figure 6.19 (a). It seems that the atoms sputtered from the Sb_2Se_3 target were collected only on the surface of the film due to the lack of energy. The fact that the as grown film is amorphous according to XRD spectrum (in Figure 6.16) supports this situation. For the post annealed film at 200 °C (in Figure 6.19 (b)), the boundary of grains became more apparent. The increment in the number of grains improved the crystal structure as it was given in Figure 6.16. As the annealing temperature was raised to 250 °C, the size of the grains increased visibly. It is thought that the mobility of Se and Sb atoms may be high enough to rearrange the formation of larger grains. As a result of further increment of annealing temperature to 350 °C, the grainy structure became more evident. This may be resulted since the small particles combine with increasing temperature to form larger particles. However, as the annealing temperature is continued to increase 400 °C, infrequent pinhole formation starts to be seen on the film surface. The number and the size of the pinholes increase by raising the heat treatment temperature to 450 °C. It is inferred from the SEM pictures that heat treatment explicitly improved the grainy structure of as grown Sb_2Se_3 films. However, annealing temperature higher than 350 °C results in a deterioration the structure and the stability of Sb_2Se_3 films. It can be concluded that, the structural properties of Sb_2Se_3 films are very sensitive to post annealing temperature.

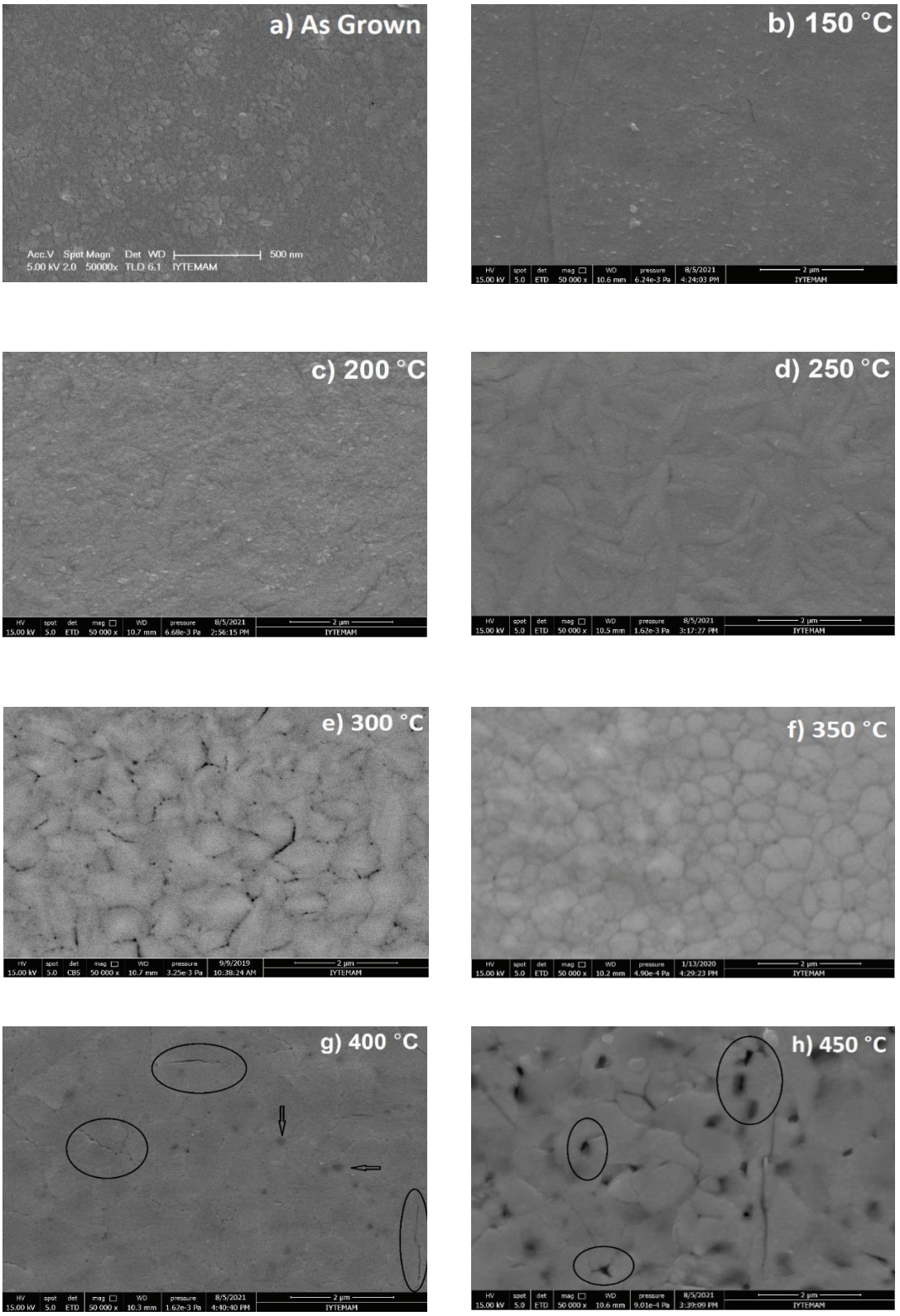

Figure 6.19. Surface morphology of as grown and heat treated Sb_2Se_3 thin films.

Since the film composition is also an important parameter, energy dispersive X-ray spectroscopy (EDS) analyses have been realized on as grown and heat-treated Sb_2Se_3 films. All Sb_2Se_3 films have average atomic percent ratio of Sb/Se lower than the

stoichiometric composition of 0.66 indicating Se-rich composition. This case is desired for photovoltaic applications because in the excess of Se the p-type character of Sb_2Se_3 film is improved by the shallow acceptors Se_{Sb} and V_{Sb} (X. Liu et al. 2017). Due to low melting point (~ 220 °C) Se element (G. X. Liang et al. 2018b), Se concentration of annealed films is lower than the as grown Sb_2Se_3. However, the reason why the Se concentration does not change very high despite the heat treatment is the condensation of Se during the cooling down of the film (Shongalova, Correia, Teixeira, et al. 2018).

Table 6. 6. Average atomic compositions of as grown and annealed Sb_2Se_3 films.

Sb_2Se_3 Films	**Average Atomic %**		**Std. Deviation of Atomic %**	**Sb/Se Ratio of Average Atomic %**
	Se	**Sb**		
As grown	64.04	35.96	0.08	0.56
150 °C	63.03	36.97	0.24	0.59
200 °C	62.85	37.15	0.39	0.59
250 °C	62.60	37.40	0.43	0.59
300 °C	62.48	37.52	0.25	0.60
350 °C	62.32	37.67	0.38	0.60
400 °C	60.71	39.29	0.53	0.64
450 °C	62.46	37.54	0.86	0.60

As seen from the Table 6.6, the standard deviation of the films annealed at 400 and 450 ˚C, which are the highest heat treatment temperatures, showed the largest value among the others. This is the result of a deterioration of the structure due to high annealing temperature which were also detected from the surface images of related films.

6.3.4. Raman Analysis of Sb_2Se_3 Films Annealed at Different Temperatures

The detailed investigations about the structure of Sb_2Se_3 films were further analyzed by Raman scattering spectra. It is seen from Figure 6.20 that all films have the characteristic Raman modes of Sb_2Se_3 phase. The peak detected at 210 cm^{-1} is more apparent for annealed films, and it is thought to be related to the transition of the film from amorphous to crystalline structure by heat treatment. For the film annealed at 450 °C, this peak shows the highest shift towards the higher wavenumber region, which is attributed to the increment in the structural degradation because of high annealing temperature. This result was also supported for the film annealed at 450 °C by SEM surface analysis as given in Figure 6.19. For the peak detected at 253 cm^{-1}, there are different considerations. According to literature, this peak either belongs to selenium or antimony oxide. If this peak comes from the Se-Se vibration, it is called A_{1g} Raman active mode of Sb_2Se_3 (Z. Li et al. 2017a; Shongalova, Correia, Vermang, et al. 2018; Tao, Hu, Guo, et al. 2019). If this peak belongs to oxide phase, it may have occurred during the Raman measurement.

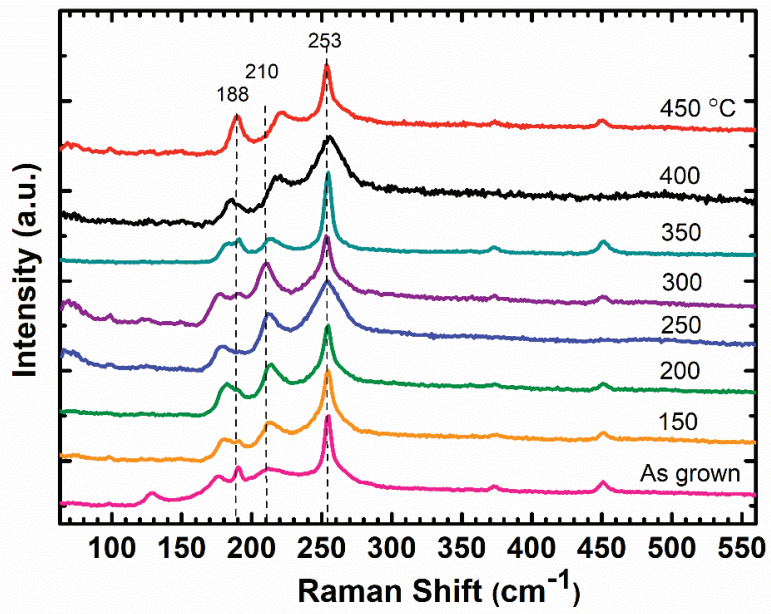

Figure 6.20. Raman scattering spectra of annealed Sb_2Se_3 films.

6.3.5. Optical Analysis of Sb_2Se_3 Films Annealed at Different Temperatures

Transmission spectra of Sb_2Se_3 thin films with respect to wavelength are given in Figure 6.21. As grown film displays higher transmission than that of the annealed Sb_2Se_3 films in the visible region. Due to red shift, absorption edge moves through the higher wavelength side implying a decrement in the optical bandgap for the annealed films. In the transmission measurements, the interference peaks towards larger wavelengths were detected for all films. After thermal processing, the intensity of these peaks decreased compared to as grown Sb_2Se_3. The Sb_2Se_3 annealed at 450 °C shows different variation trend. This film has the lowest transmission and no sharp interference peaks can be detected. The reason might be the existence of defects in the film. The optical band gap energy (E_g) of Sb_2Se_3 films (Figure 6.22) can be deduced experimentally from the transmission spectra by the Tauc method (Equation 6.1). The variation of the band gap energy depending on the temperature is given in the Table 6.7.

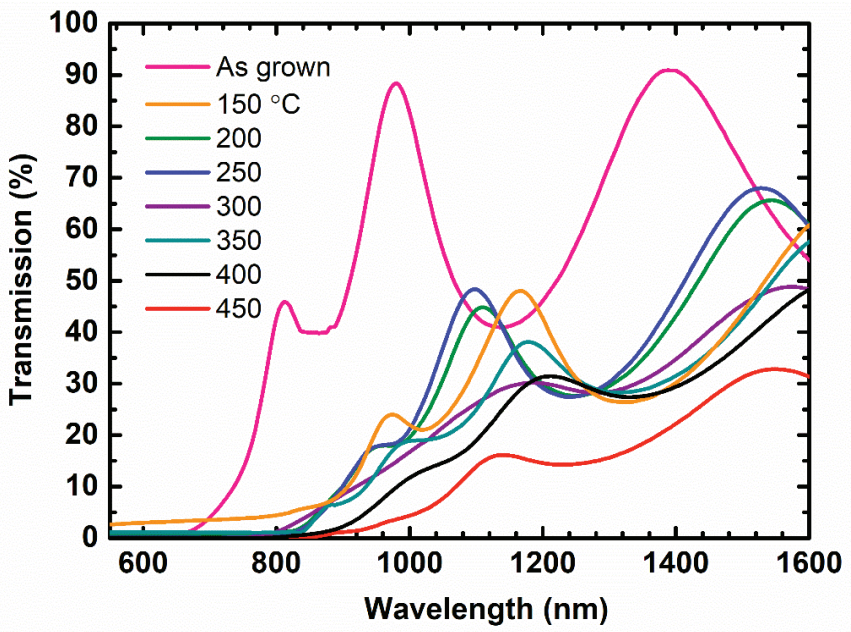

Figure 6.21. Transmission of annealed Sb_2Se_3 films.

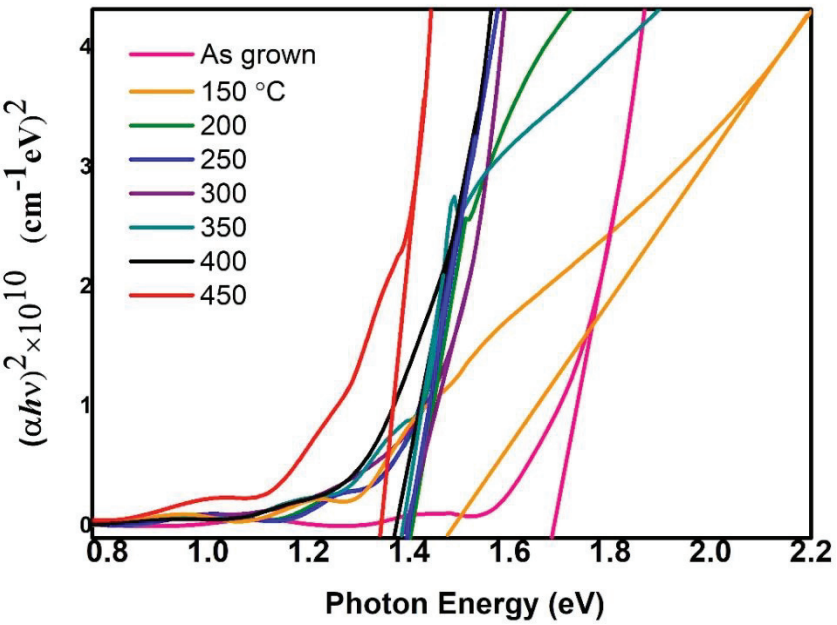

Figure 6.22. Optical band gap energy of as grown and heat treated Sb_2Se_3 films.

Table 6.7. Variation of the bandgap energy of Sb_2Se_3 thin films with respect to the post annealing temperature.

Heat treatment temperature (˚C)	**Bandgap Energy (eV)**
As grown	1.68
150	1.47
200	1.40
250	1.40
300	1.39
350	1.38
400	1.37
450	1.34

According to the Table 6.7, the optical bandgap energy is inversely proportional to post annealing temperature. The optical bandgap energy was extracted as 1.68 eV for as grown film and as 1.34 eV for the heat-treated film at 450 °C. The reason for the high energy bandgap value of the as grown film is that the film as being in amorphous structure seen as well in XRD analysis in Figure 6.16. Reduction in the E_g energy value with respect to elevated post annealing temperature was detected due to the recrystallization of the Sb_2Se_3 films.

6.3.6. Conclusion

Post annealing effect over Sb_2Se_3 thin films was tested, and the results revealed that the post annealing temperature has a crucial effect on the structural, morphological, and optical properties of Sb_2Se_3 thin films. The results listed as:

- Annealing is required to obtain crystalline Sb_2Se_3.
- The growth orientation has a high relation with the post annealing temperature.
- The desired (211) crystal direction increased with temperature (above 300 °C).
- The bandgap energy of Sb_2Se_3 films decreased with respect to increasing heat treatment temperature.
- Optimum temperature range measured 300 – 350 °C.

6.4. Efficiency Analyses of Sb_2Se_3 Based Solar Cells

6.4.1. Superstrate Solar Cell Characterization

In this work SLG/ ITO/ Zn(O,S)/ Sb_2Se_3/ Ag device configuration was used in order to fabricate superstrate solar cells. ITO glass substrates were obtained from TEKNOMA Technological Materials Industrial and Trading Inc. (www.teknoma.net). The growth details of each layer were mentioned in Chapter 5. Two different solar cells were grown using 0.5 and 1.0 sccm oxygen in the Zn(O,S) buffer layer and they were named with Solar Cell-1 and Solar Cell-2, respectively. After the deposition of 500 nm thick absorber layer, the structure SLG/ ITO/Zn(O,S)/ Sb_2Se_3 was annealed at 350 °C for 30 minutes with a ramping rate 20°C/ min. and under Ar gas atmosphere. Devices were completed with the silver top contact layer. These grown solar cells were named SolarCell-1 and SolarCell-2. Table 6.8 shows the Zn(O,S) thin film parameters for each solar cells.

Table 6.8. Deposition parameters of Zn(O,S)/Sb_2Se_3 solar cells.

Sample Name	Ar (sccm)	O (sccm)	(O/Ar+O) (%)	Deposition time (seconds)
SolarCell-1	50	0.5	0.99	360
SolarCell-2	50	1.0	1.96	390

Figure 6.23 demonstrates the fabricated solar cells and designed cell areas with top contacts. In this study, the investigated devices showed electrically inhomogeneity. The photovoltaic characteristic of each designed cell showed different results for the same device. Therefore, in this work, only the highest efficiency values were given.

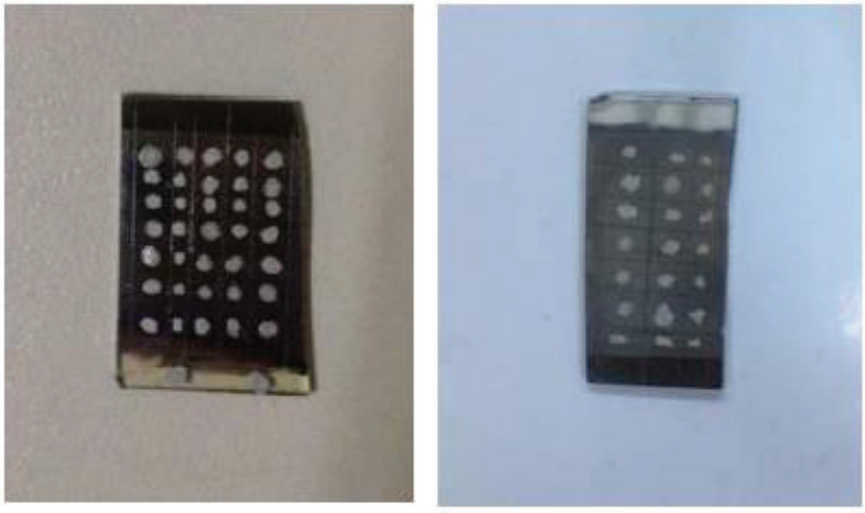

Figure 6.23. Representation of constructed Sb_2Se_3 solar cells in superstrate configuration.

Figure 6.24 shows the XRD patterns of SLG/ITO/Zn(O,S)/Sb_2Se_3 structure. It has polycrystalline structure and exhibit characteristic peaks of orthorhombic Sb_2Se_3 (JCPDS 15-0861). According to the XRD analysis, the dominant orientation of the Sb_2Se_3 absorber layer corresponds to the (020), (120) and (230) lattice planes. The peaks with (020) and (120) orientations, observed at 15.1° and 16.8°, respectively, cause high series resistance along the Sb_2Se_3 film which results in a decrease in solar cell efficiency (Z. Chen et al. 2019). Contrarily, the (221) orientation allows better carrier transport through the Sb_2Se_3 film which improves the diode quality and thus the device performance by

providing less defects formation in the interface (Chen et al. 2019). In addition, the antimony oxide (Sb_2O_3) phase was detected on the Sb_2Se_3 surface, which is the top layer of superstrate solar cell. Shiel et al. investigated the effect of Sb_2O_3 phase on the efficiency values of Sb_2Se_3 based solar cells. They chemically etched the Sb_2O_3 phase with ammonium sulfate. Removal of the Sb_2O_3 phase by etching decreased the potential barrier at the back contact and the series resistance of the solar cell. In this way, fill factor is increased. However, it was stated that the decrease in the shunt resistance and the short-circuit current density is resulting in low efficiency (Shiel et al. 2019). Fleck et al. also investigated the effect of the thin Sb_2O_3 phase on the efficiency of the solar cell by exposing the superstrate structured Sb_2Se_3 solar cells to the atmosphere at different time durations. They observed that the oxide phase formed on the Sb_2Se_3 surface reduces the back contact barrier and the yield losses that may occur as a result of recombination (Fleck et al. 2020). Considering both studies, it was concluded that the formation of thin Sb_2O_3 phase on the Sb_2Se_3 surface, contributed to the efficiency.

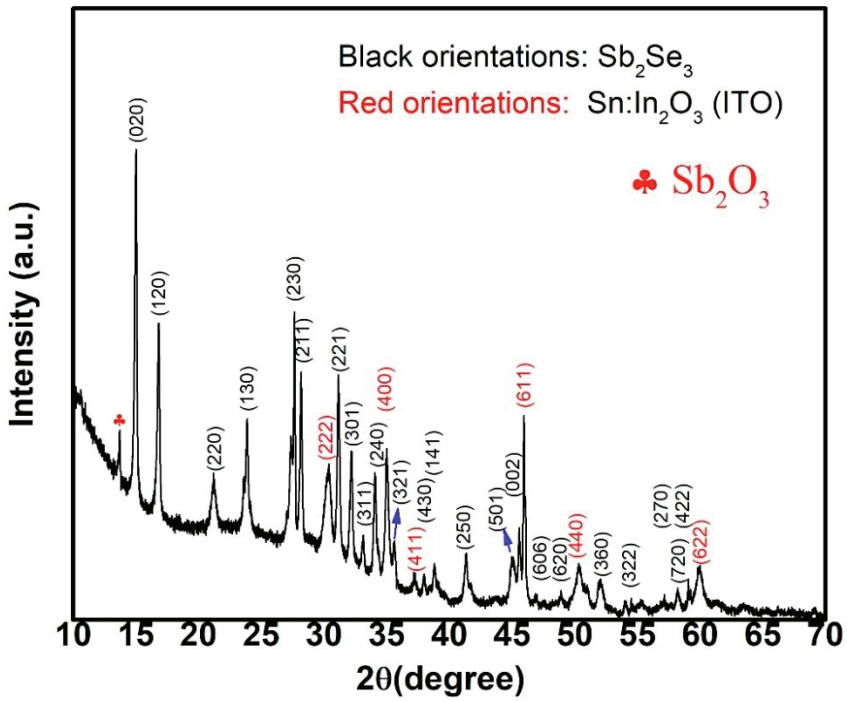

Figure 6.24. XRD analysis of annealed SLG/ITO/Zn(O,S)/Sb_2Se_3 structure.

Surface morphology of the heat treated SLG/ITO/Zn(O,S)/Sb_2Se_3 structure is given in Figure 6.25. Unusual surface morphology was detected and can be seen in Figure 6.25. White bright crystal structures were observed on the film surface and embedded in the film. These shapes belong to the Sb_2O_3 formation which is also supported by XRD pattern of the SLG/ITO/Zn(O,S)/Sb_2Se_3 structure. To determine the atomic composition of this structure, point EDS analysis was taken and given in Table 6.9. According to point EDS analysis, this white crystal structure contains 43 % Sb and 57 % O elements. As well as the composition, the shape of this structure support the Sb_2O_3 formation (Z. Zhang, Guo, and Wang 2001).

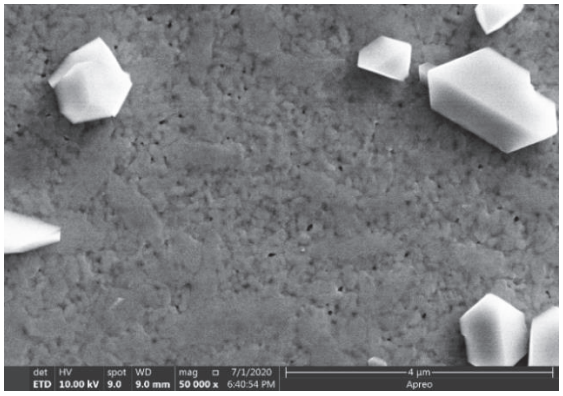

Figure 6.25. SEM surface image of the heat treated SLG/ITO/Zn(O,S)/Sb_2Se_3 structure.

Table 6.9. EDS analysis of the crystal.

Element	**Atomic %**
Sb	43
O	57
Total	100

During the heat treatment, some Se is evaporated as well separated from the structure. When the annealed sample is taken to the atmospheric region, it can be thought that the oxide phase is formed because of the contact of the film with the air. The evaporation of Se element, may have caused voids in the Sb_2Se_3 layer. The tiny voids observed in Figure 6.25 are supportive evidence of this. These voids act as recombination centers for charge carriers and result in obtaining lower J_{sc} and V_{oc} from the solar cell. Moreover, these voids can act as shunt paths and reduce shunt resistance (Zhou et al. 2015).

The detailed investigations about the structure of the heat-treated structure was further analyzed by Raman scattering spectra. Figure 6.26, shows the Raman spectrum of the film SLG/ITO/Zn(O,S)/Sb_2Se_3. Since the laser (514.0 nm wavelength) of the Raman spectroscopy can reach a depth of 150 nm from the sample surface. Therefore, the Raman signals of the ITO and Zn(O,S) layers of the bulk SLG/ITO/Zn(O,S)/Sb_2Se_3 was not

detected. Therefore, the Raman spectrum only gives the characteristic Raman modes of the Sb_2Se_3 structure. The wide peak observed at wavenumber of 180 and 220 cm^{-1} interval covers the characteristic peaks of the Sb_2Se_3 structure, which are observed at 188 and 210 cm^{-1} and called A_{1g} vibration modes. These peaks are derived from the Sb-Se vibration mode (Tao, Hu, Guo, et al. 2019; Z. Li et al. 2017a). As stated in the above studies (Section 6.2 and 6.3) the peak observed at the wavenumber 252 cm^{-1} either belongs to Sb_2Se_3 or Sb_2O_3 (Shongalova, Correia, Vermang, et al. 2018; Chong Wang et al. 2020). In Figure 6.26, the slightly visible peak at 450 cm^{-1} corresponds to the Sb_2O_3 oxide phase, and the presence of this phase is also supported by XRD (Figure 6.24) and SEM (Figure 6.25) surface images.

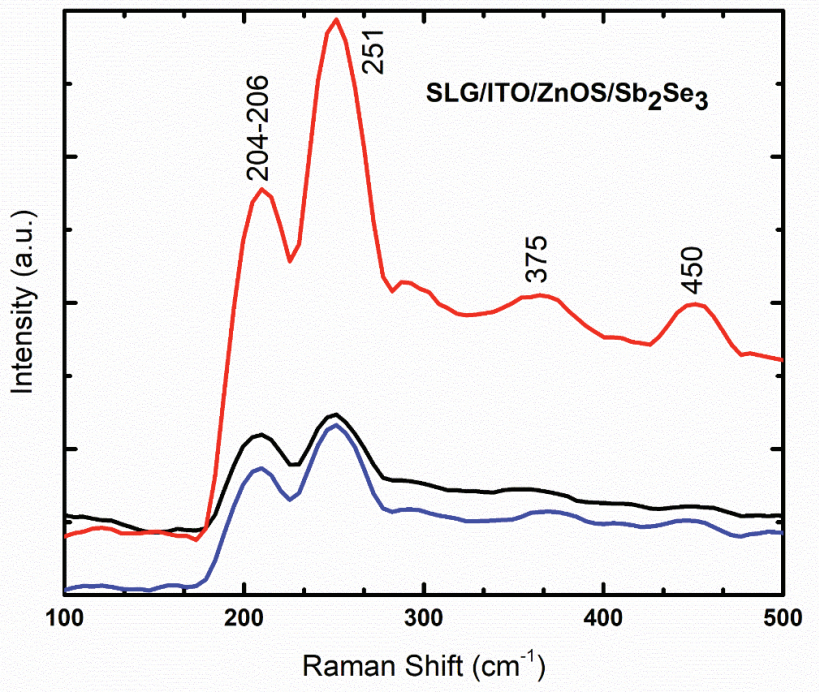

Figure 6.26. Raman analysis of annealed SLG/ITO/Zn(O,S)/Sb_2Se_3 structure.

Figure 6.27(a) shows the current-voltage characteristics of the SolarCell-1 under AM1.5 illumination. It demonstrates the graph of the electrical measurement of the point where the shift was observed under illumination.

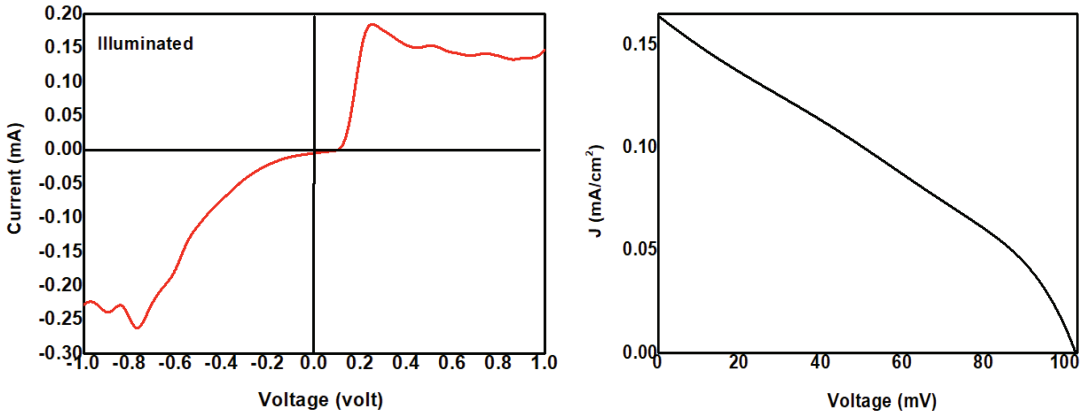

Figure 6.27. a) I-V measurement of the SolarCell-1 where the shift was observed under illumination b) I-V measurement of the SolarCell-1 where the shift was observed under illumination.

Figure 6.27(a) shows a region of the SolarCell-1, where a response was observed to light under illumination. The J-V curve of the I-V curve measured under illumination is given in Figure 6.27(b). The electrical parameters obtained from the J-V graph are open circuit voltage (V_{oc}) 102.0 mV and short circuit current density (J_{sc}) 0.17 mA/cm^2. As a result of photovoltaic calculations with using V_{oc} and J_{sc}, the fill factor of the SolarCell-1 is 31.4% and the efficiency value is 0.005%. Since the J-V curve is close to linear, shunt (parallel) and series resistance could not be calculated. It is thought that the low efficiency of the SolarCell-1 may be the result of structural factors such as active layer morphology and microstructure.

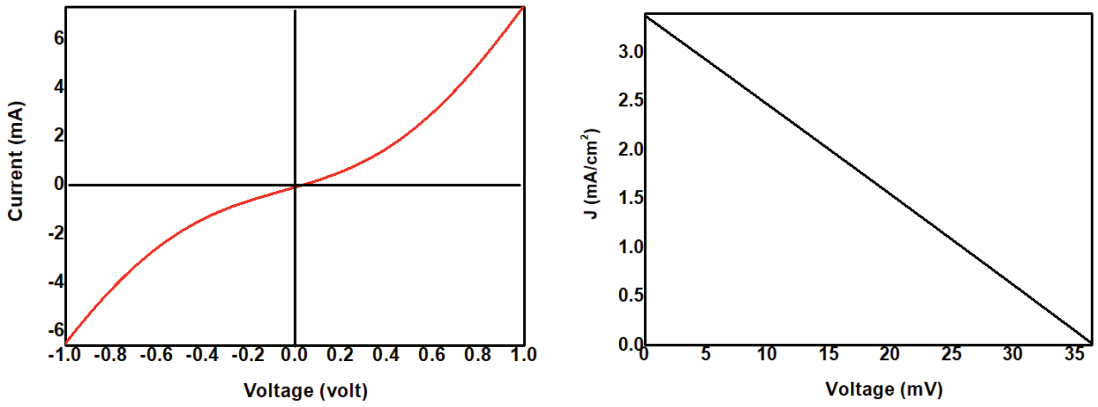

Figure 6.28. a) I-V measurement of the SolarCell-2 where the shift was observed under illumination b) J-V measurement of the SolarCell-2 where the shift was observed under illumination.

Figure 6.28(a) shows a region of the SolarCell-2 where a response to light was observed under illumination. The J-V curve of the I-V curve measured under illumination is given in Figure 6.28(b). The electrical parameters obtained from the J-V graph are open circuit voltage (V_{oc}) 36.36 mV and short circuit current density (J_{sc}) 3.36 mA/cm^2. As a result of photovoltaic calculations with using V_{oc} and J_{sc}, the fill factor of the SolarCell-2 is 25.4% and the efficiency value is 0.031%. Since the J-V curve of the SolarCell-2 is linear, series and shunt resistance could not be calculated.

It was reported that the series resistance of the Zn(O,S) buffer layers grown by the magnetron sputtering technique, increased up to about 40% with the increase in the sulfur ratio. The increase in series resistance may be one of the reasons for the low efficiency. Due to the lack of high-energetic photons in Zn(O,S), it is proposed that the barrier height would be higher than in CdS with a low band gap. Therefore, it has been reported that I-V distortion can be observed even under illumination, for the Zn(O,S) with higher band gap (Song 2013). In the fabricated solar cells, the barrier height decreased the performance by restricting the electron flow.

6.4.2. Substrate Solar Cell Characterization

In this work SLG/Mo/CdS/Sb_2Se_3/ITO which is called SolarCell-3 and SLG/Mo/CdS/ZnS/Sb_2Se_3/ITO which is called SolarCell-4, were produced in substrate solar cell structure. Two different solar cells were grown with single buffer layer (CdS/ Sb_2Se_3) and double buffer layer (CdS/ZnS/Sb_2Se_3), respectively. Mo glass substrates were obtained from TEKNOMA Technological Materials Industrial and Trading Inc. (www.teknoma.net). The growth details of each layer were mentioned in Chapter 5. After the deposition of 500 nm thick absorber layer, structures SLG/Mo/CdS/Sb_2Se_3 and SLG/Mo/CdS/ZnS/Sb_2Se_3 were annealed at 350 °C for 30 minutes with a ramping rate 20°C/ min. and under Ar gas atmosphere. Devices were completed with the ITO top contact layer and were cut to form small squares of 0.03 cm^2 for each cell.

Figure 6.29 indicates the X-ray diffraction patterns of the SLG/Mo/Sb_2Se_3, SLG/Mo/Sb_2Se_3/CdS/ITO and SLG/Mo/Sb_2Se_3/CdS/ZnS/ITO structures. It is seen that whole layer stacks have a polycrystalline structure and demonstrate characteristics peaks

of Sb_2Se_3. The peak detected at approximately 12.73˚ observed at only the XRD analysis of device structures. It was determined that this diffraction point belongs to the closest cubic Sb_2O_3 phase. When heating is carried out below 570 ˚C, this phase occurs in cubic form (Chin, Cheong, and Razak 2010). However, this phase was not observed in the Mo/Sb_2Se_3 structure which was heat-treated at 350 ˚C. It has been thought that the antimony oxide phase may have formed during chemical bath deposition of CdS buffer layer.

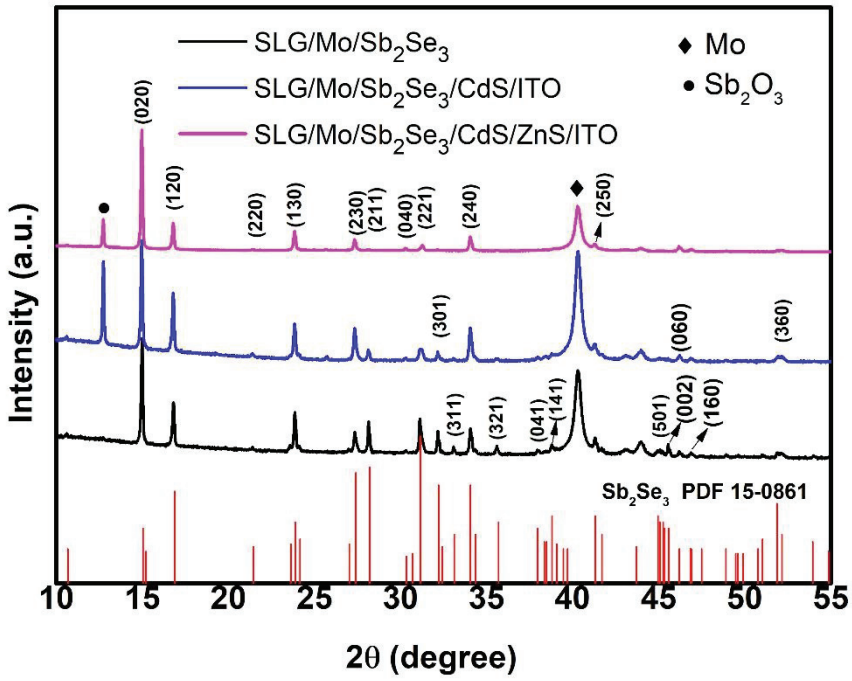

Figure 6.29. XRD analysis of SLG/Mo/Sb_2Se_3, SLG/Mo/Sb_2Se_3/CdS/ITO and SLG/Mo/Sb_2Se_3/CdS/ZnS/ITO layer stacks.

Surface topography of SolarCell-4 (SLG/Mo/Sb_2Se_3/CdS/ZnS/ITO) at different magnifications is shown in Figure 6.30. It has homogeneous surface morphology with apparent cylindrical grain structure. The large grains decrease the recombination of photo-generated carriers at grain boundaries, so they can provide increase in the V_{oc} of a device. On the other hand, white bright crystals over the entire sample surface can be seen in Figure 6.30. The white bright crystals over the entire sample surface were attributed to oxide phases. Since ITO was the top layer of the structure, it shows similarities with the SEM images in the literature in terms of granular structure (Jadhavar et al. 2015). On the other hand, zinc oxide (ZnO) may have formed from the interaction between ZnS and

ITO layers since they are adjacent. However, solar cell layers other than Sb_2Se_3 could not detected by XRD since they were not annealed and hence, crystallized.

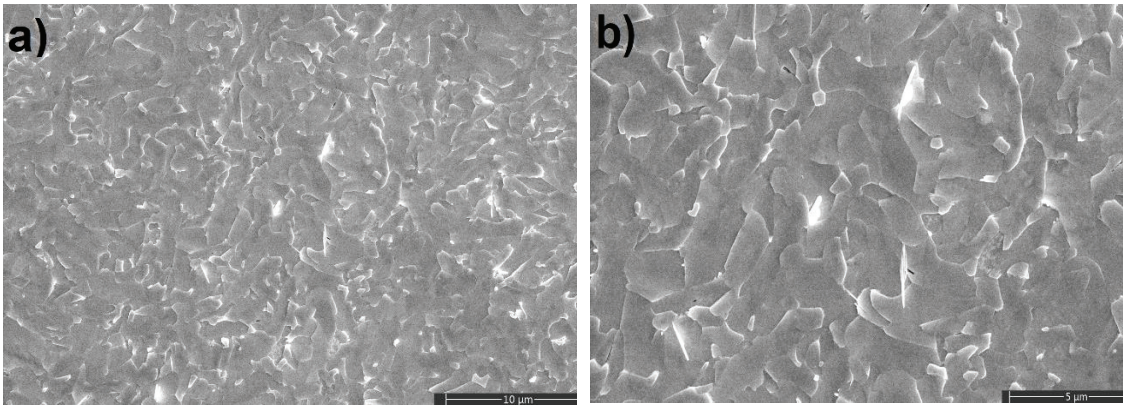

Figure 6.30. SEM surface image of SLG/Mo/Sb_2Se_3/CdS/ZnS/ITO structure at a) 10 000 X and, b) 20 000 X magnifications.

Figure 6.31 and Figure 6.33 shows the SEM cross section image of the SLG/Mo/Sb_2Se_3/CdS/ITO and SLG/Mo/Sb_2Se_3/CdS/ZnS/ITO devices and the EDS points received from the regions. In the Figure 6.31, solar cell layers were clearly distinguished from each other. The absence of voids through the solar cell layers is important for performance of the device. It can be attributed to a dense structure. Figure 6.32 and Figure 6.34 demonstrates the EDS analysis in graphical format. The atomic percentages of the elements are consistent with the analyzed points. Detailed interpretation is given below.

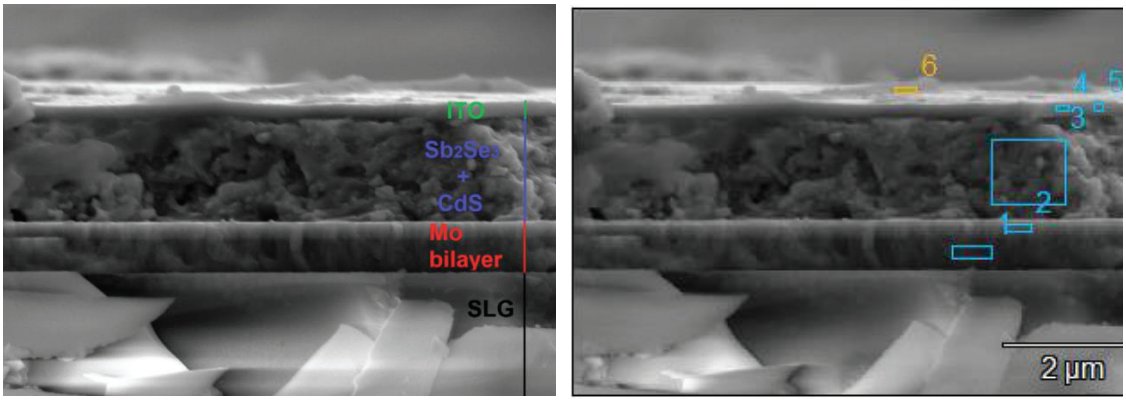

Figure 6.31. SEM cross section and EDS analysis regions of cross section of SLG/Mo/Sb_2Se_3/CdS/ITO solar cell at 50 000X magnification.

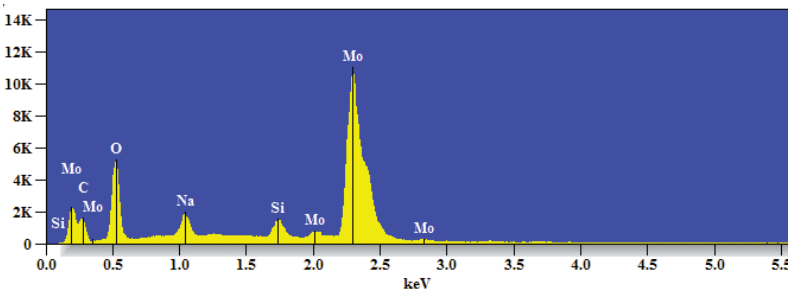

Point 1

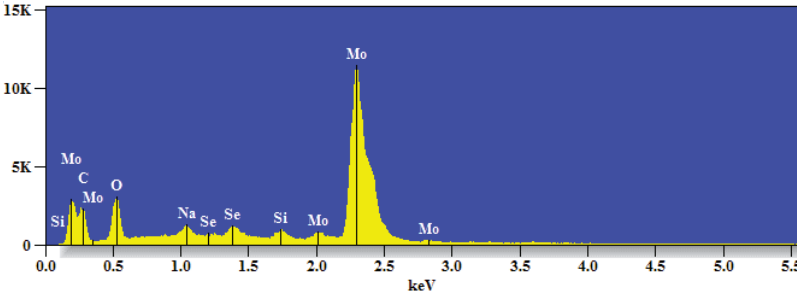

Point 2

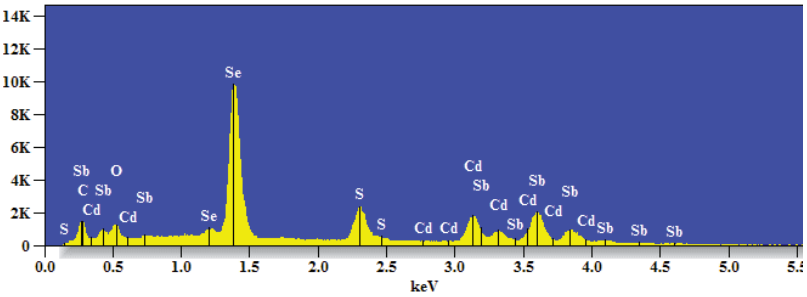

Point 3

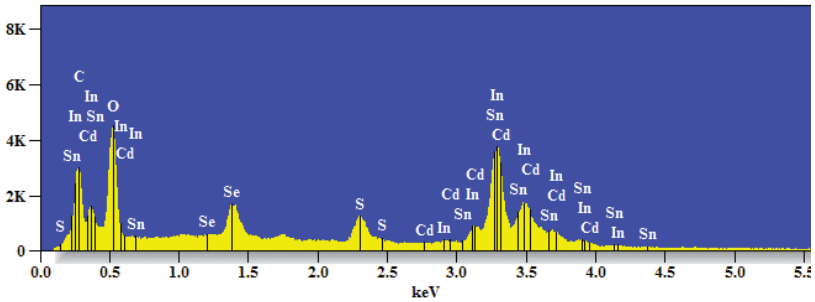

Point 4

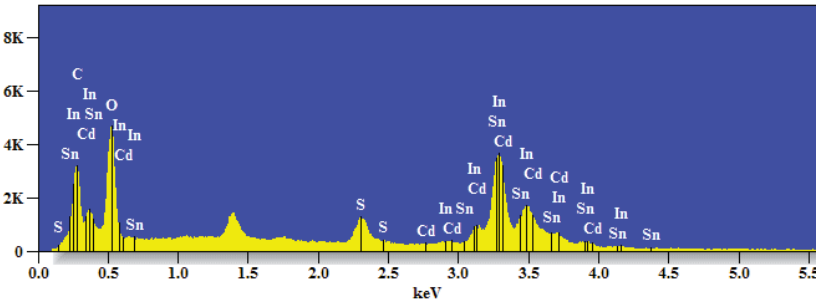

Point 5

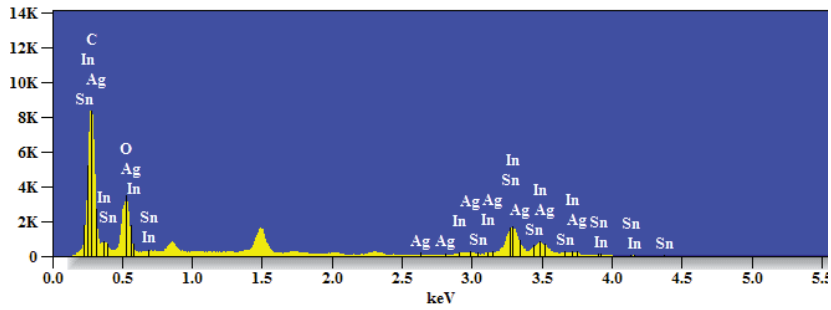

Figure 6.32. EDS analysis of selected regions on cross section image of SLG/Mo/Sb_2Se_3/CdS/ITO solar cell

Table 6.10. EDS analysis of cross section view of SLG/Mo/Sb_2Se_3/CdS/ITO solar cell.

	C	O	Na	Si	S	Se	Mo	Ag	Cd	In	Sn	Sb
Point 1	10.97	54.95	4.17	2.86			27.04					
Point 2	13.88	43.04	2.32	1.65		1.37	37.74					
Point 3	29.64	13.08			9.82	22.44			9.49			15.53
Point 4	14.87	58.30			3.85	2.89			1.46	18.65		
Point 5	13.66	61.64			4.02				1.88	18.81		
Point 6	37.96	50.21						0.66		10.21	0.96	

Table 6.10 shows the atomic percentage of the existing elements in the solar cell layers which were labeled from Point 1 to Point 6. According to the EDS analysis of SolarCell-3 cross section, there are elemental differences from bottom to top. At bottom layer (Point 1), we observed signals as Carbon, Oxygen, Sodium and Silicon (C, O, Na and Si) from the glass. At Point 2 which corresponds to the Mo back contact layer, Mo element has the highest intensity while glass signals showed decrease. In addition, a very small amount of selenium was observed. At Point 3, there are obvious signals from Sb_2Se_3 absorber layer however, existence of oxygen is attributed to the oxide phase (Sb_2O_3). We also observed Cd and S elements since that point corresponds to the either buffer or absorber layers. At Point 4, Oxygen is the most abundant among the elements because ITO compound contributed to the O_2 intensity. No Sb element was found at this point. Nevertheless, due to the migration of Cd, S and Se elements, very few of these elements were observed. As going upward to Point 5, Se is lost and there were still In, Cd, O_2 and S signals from both ITO and CdS layers. C element was seen in all layers as in this layer. At the top point which shows the surface of the SolarCell-3, Sn was observed in addition

to In and O_2 elements. At this point, trace amount of Ag was detected. This is attributed to the silver paint contacts.

In Figure 6.33, cross section image of the SolarCell-4 can be seen. Analyzed regions in terms of EDS were marked from 1 to 6 at the same image. EDS analysis of SolarCell-4 in graphical format is given in Figure 6.34 while data is given in Table 6.11.

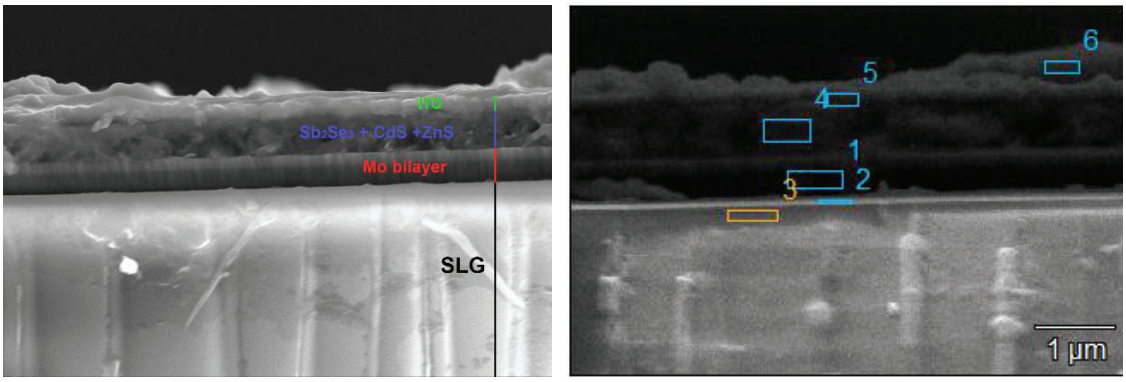

Figure 6.33. SEM cross section and EDS analysis regions of cross section of SLG/ Mo/ Sb_2Se_3/CdS/ZnS/ITO solar cell at 40 000X magnification.

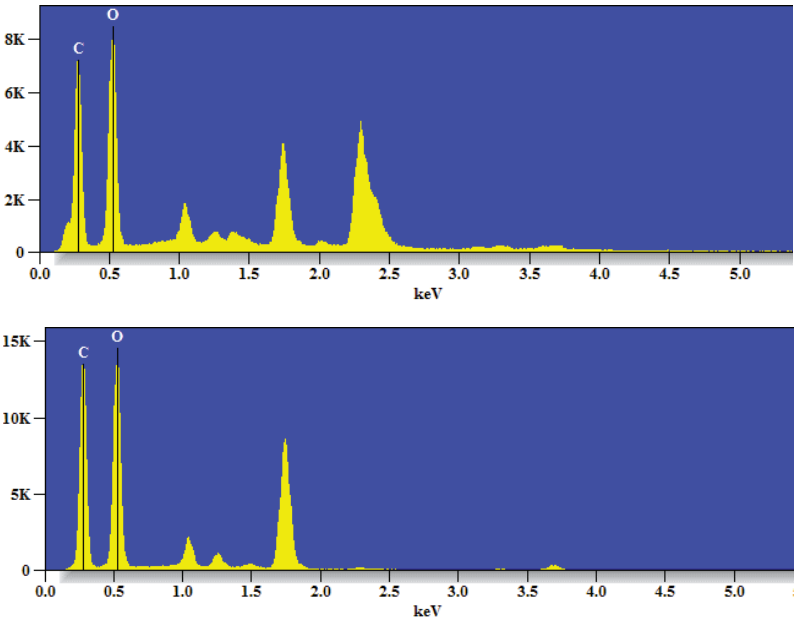

Point 1

Point 2

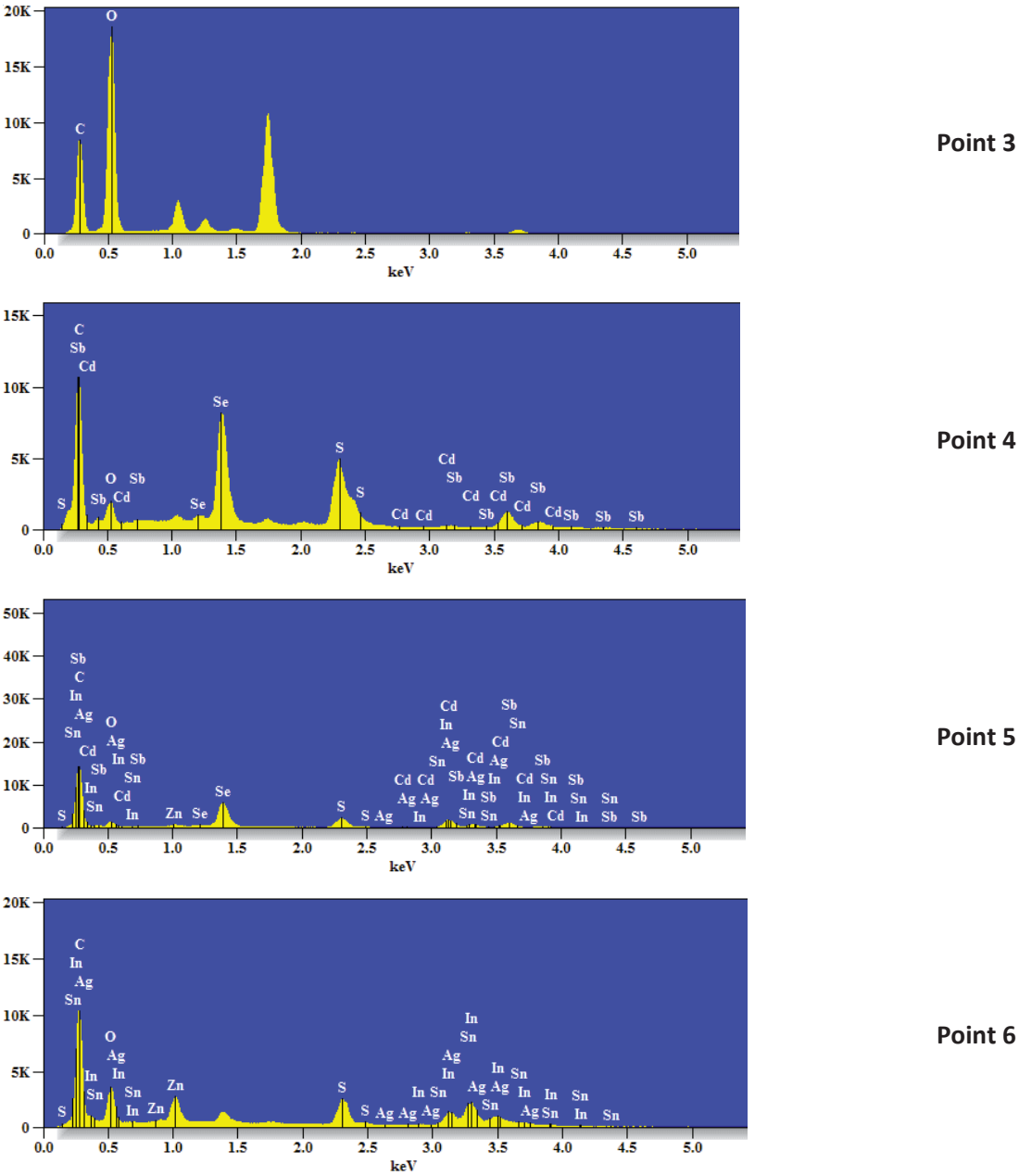

Figure 6.34. EDS analysis of selected regions on cross section image of SLG/Mo/Sb_2Se_3/CdS/ZnS/ITO solar cell.

Table 6. 11. EDS analysis of cross section view of SLG/Mo/Sb_2Se_3/CdS/ZnS/ITO solar cell.

	C	O	Na	Si	S	Zn	Se	Mo	Ag	Cd	In	Sn	Sb
Point 1	34.93	49.17	2.47	6.12				7.31					
Point 2	46.24	43.06	1.77	8.92									
Point 3	34.75	50.86	2.79	11.6									
Point 4	73.20	8.97	0.45		8.14		5.87			0.14			3.24
Point 5	73.91	7.43			4.11	0.29	5.58		0.00	4.62	0.26	0.07	3.73
Point 6	56.53	29.36			5.83	4.10					4.19		

Table 6.11 shows the atomic percentage of the existing elements in the solar cell layers which were labeled from Point 1 to Point 6. According to the EDS analysis of SolarCell-3 cross section, there are elemental differences from bottom to top. At bottom layer (Point 3), we observed signals C, O, Na and Si from the glass while we no signals from other layers were observed. At Point 2 which corresponds to the intersection point of glass and Mo back contact, same elements as Point 3 were observed. Point 1 shows the Mo back contact layer; therefore, Mo element has the highest intensity while glass signals showed decrease. Different from SolarCell-3, no other compound was detected in the back contact layer of SolarCell-4. At Point 4, there are obvious signals from Sb_2Se_3 absorber layer however, existence of oxygen is attributed to the oxide phase (Sb_2O_3). We also observed Cd and S elements since that point corresponds to the either buffer or absorber layers. In SolarCell-4, buffer layer consists of ZnS and CdS compounds but there was no Zn signal in the analysis of Point 4. This may be because Zn element was not present at that point. At Point 5, Na element was not observed because it was far away from the glass. Zn was detected at this point for the first time. In addition to absorber and buffer layers' signals, In and Sn elements belonging to ITO were also observed. At the top point (Point 6), oxygen has higher intensity because ITO compound contributed to the O_2 intensity. No Sb, Se and Cd elements were found at the surface. Nevertheless, there were existing Zn and S elements. It may have observed because ZnS is located just below the ITO and elements may have migrated upwards.

Following characterizations and analysis, SolarCell-3 and SolarCell-4 fabricated in SLG/Mo/Sb_2Se_3/CdS/ITO and SLG/Mo/Sb_2Se_3/CdS/ZnS/ITO configurations respectively, were scribed into squares by razor blade and silver pasted for contacts. The

open circuit voltage (V_{oc}) and short circuit current (I_{sc}) values obtained from the solar cell, vary regionally. This may be due to inhomogeneity or structural defects that occur in the films during depositions. Here, the points where the best results were obtained were shared.

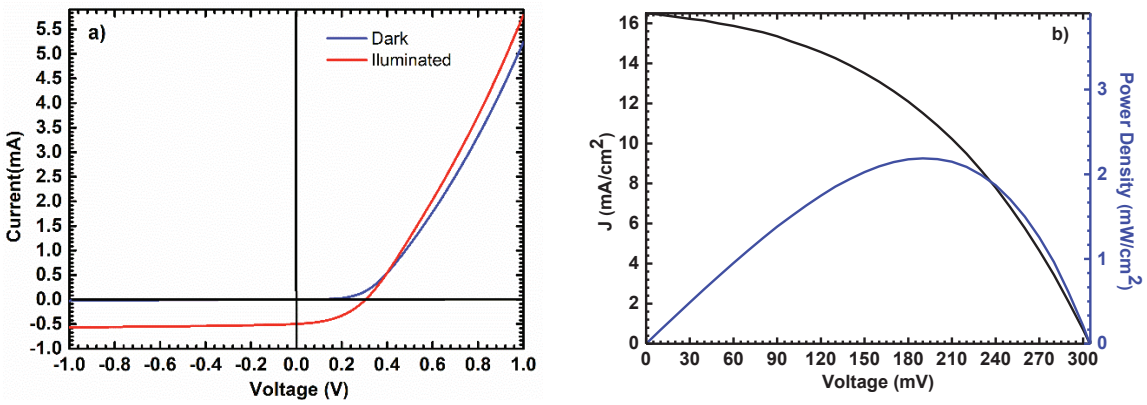

Figure 6.35 a) I-V measurement of the SolarCell-3 under dark and illumination conditions. b) J-V and P-V curve of the SolarCell-3.

Table 6.12. Electrical parameters of SolarCell-3 and SolarCell-4.

Cell	V_{oc} (mV)	J_{sc} (mA/cm^2)	FF (%)	η (%)	R_s (Ωcm^2)	R_{sh} (Ωcm^2)
3	305	16.51	43.45	3.9	53.44	6.11
4	253	1.155	28.15	0.12	-	-

Figure 6.35(a) figures out the current-voltage characteristics of the SolarCell-3 under dark and illumination. It demonstrates the graph of the electrical measurement of the point where the shift was observed under illumination. The dark and illuminated I-V curves did not overlap, they showed a cross over. One of the reasons for that cross over is the formation of a Schottky barrier between the back contact metal and the absorber layer. Because it restricts the hole transmission from the back contact metal to the absorber layer (K. Wang et al. 2011). In the literature, such cross over has been observed in Sb_2Se_3/ CdS solar cells. Leng et al. explained the cause of the cross over they observed

in the dark and illuminated J-V curves, with the sharp conduction band or the electron barrier caused by the high acceptor density in the Sb_2Se_3 surface.

The electrical parameters obtained from the J-V graph are open circuit voltage (V_{oc}) 305.0 mV and short circuit current density (J_{sc}) 16.51 mA/cm^2. As a result of photovoltaic calculations with using V_{oc} and J_{sc}, the fill factor of the SolarCell-3 is 43.45% and the efficiency value is 3.9%. The shunt (parallel) and series resistance were calculated as 53.44 and 6.11, respectively. For an ideal solar cell, series resistance should be low while shunt resistance is infinite. SolarCell-3 has low R_{Sh} value therefore it resulted with power losses by supplying an alternate current path for the photo-generated current. For this reason, the amount of flowing current through the solar cell diminishes.

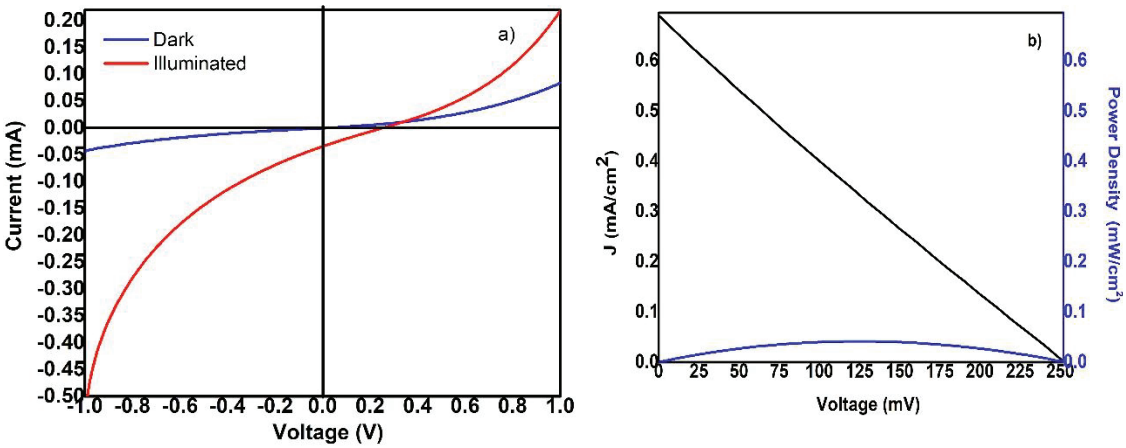

Figure 6.36 a) I-V measurement of the SolarCell-4 where the shift was observed under illumination b) J-V measurement of the SolarCell-4 where the shift was observed under illumination.

Figure 6.36(a) shows the current-voltage characteristics of the SolarCell-4 under dark and illumination. It demonstrates the graph of the electrical measurement of the point where the shift was observed under illumination. The dark and illuminated I-V curves did not overlap, they showed a cross over like SolarCell-3.

The electrical parameters obtained from the J-V graph are open circuit voltage (V_{oc}) 253.0 mV and short circuit current density (J_{sc}) 1.155 mA/cm^2. As a result of photovoltaic calculations with using V_{oc} and J_{sc}, the fill factor of the SolarCell-4 is 28.15% and the efficiency value is 0.12%. Since the J-V curve is very close to linear, shunt and series resistances could not have calculated.

CHAPTER 7

CONCLUSION

In this thesis, a total of four Sb_2Se_3-based solar cells were produced as superstrate and substrate configurations. First of all, structural and optical studies were carried out depending on the thickness, used Ar gas flow rate and post-annealing temperature of the Sb_2Se_3 absorber layer, which will be used for all solar cells. The purpose of this experimental study is to optimize the absorber layer for solar cell application and maximize the performance of the solar cell. The best achieved absorber layer was deposited with constant parameters in all solar cells. Since the absorber layer was stable, efficiency analyses were performed in terms of the different materials used in the buffer layer. The fabricated superstrate Zn(O,S)/ Sb_2Se_3 solar cell has not been studied before in the literature, hence, this study will be the first. The results of the analysis are explained in detail below.

In this thesis, the DC magnetron sputtering method was successfully used to fabricate Sb_2Se_3 thin films for solar cell applications. The effect of the deposition time and, hence, the effect of the thickness on the absorber layer was studied. The results revealed that all the samples deposited at room temperature have amorphous structure. The surface images showed partially granular structure. In addition, this study proved that the absorber layer can be coated from the Sb_2Se_3 target in a good composition with slight excess of Se. On the other hand, this study was also found that the number and intensity of Raman peaks increased as the film deposition time increases. It can be attributed to the increase of the structural regularity with the deposition time. Optical measurements demonstrated that as the film thickness increases the absorption edge shifts to higher wavelengths (red shift) and the value of the band gap energy decreases. However, calculated band gap energy values of Sb_2Se_3 films grown at room temperature are higher than the expected for p-type crystal Sb_2Se_3 because, grown samples have amorphous structure as shown by XRD analysis. Finally, the measurements on samples produced by the DC magnetron sputtering technique showed that the thickness of the amorphous films can be used as an additional control parameter in setting the value of the band gap energy (E_g).

The RF magnetron sputtering technique was also successfully used to fabricate Sb_2Se_3 thin films for solar cell applications, in Chapter 6.2. During the film deposition, the effect of the Ar gas flow rate which varies from 20 to 50 sccm in increments of 5 sccm on the absorber layer was investigated. The results revealed that the variation in sputtering gas flow rate which changes growth rate had a slight effect on the film thickness. It has been observed that all the films have polycrystalline structure, but they have different preferred orientations. From the texture coefficient calculations, the domination of crystallite orientation of each film was determined. The film Sb-25 represented desired crystal orientation for photovoltaic application. As a result of partial decomposition of Sb_2Se_3, the oxide phase (Sb_2O_3) was observed in the XRD analysis of films grown using argon with 40 sccm and above. We demonstrated that the surface morphology of films changed in shape depending on argon flow rate. Depending on the atomic composition of the films, the Sb/Se ratio was obtained above the stoichiometric ratio (Sb/Se>0.66) in the films where the oxide phase is formed, while they generally had a composition rich in selenium. Due to the Sb_2O_3 phase, transmission above 30% in the visible range (400-800 nm) was obtained for the Sb_2Se_3 films deposited using 40, 45 and 50 sccm Ar flows. Acquired results showed that both the existence of Sb_2O_3 as a secondary phase and the amount of Ar flow used during film deposition changed the bandgap energy (E_g) of Sb_2Se_3 films. The results showed that to grow Sb_2Se_3 films with low E_g value to be used as absorber layer in photovoltaic applications, it is convenient to use argon flow below 40 sccm. Finally, the measurements on samples grown by the RF magnetron sputtering technique showed that the argon gas flow rate strongly influence the structural, morphological, and optical properties of Sb_2Se_3 films. Since Sb_2Se_3 film is one of the main layers of solar cells, the results presented here may help us to achieve thin film solar cells with higher efficiencies.

Post annealing effect over Sb_2Se_3 thin films was tested, and the results revealed that the post annealing temperature has a crucial effect on the structural, morphological and optical properties of Sb_2Se_3 thin films. Therefore, annealing is required to change from amorphous structure of as grown film into crystalline Sb_2Se_3. The results inferred that the growth orientation of films had a high relation with the post annealing temperature. As a results of the reorientation of microstructure with temperature, the variation in lattice parameters were detected. Above 300˚C, the average crystallite size through the (211) crystal orientation increased with temperature. However, the average

crystallite size of undesired (120) direction highly increased at temperatures higher than 350 ˚C. According to SEM surface morphology measurements, 350 °C was identified as a critical annealing temperature whereas the pinholes started to occur above this post annealing temperature. EDS analysis presented that all Sb_2Se_3 films have Se-rich composition. Raman spectra of all films exhibited characteristic vibration modes of Sb_2Se_3. Sb-Se vibration mode at 210 cm^{-1} demonstrated the highest shift towards the higher wavenumber region for the film annealed at 450 °C which is the result of structural deformation. The bandgap energy of Sb_2Se_3 films is detected a decrement with respect to increasing heat treatment temperature. All results revealed that physical properties of Sb_2Se_3 films are in a close relation with the post annealing temperature. Moreover, Sb_2Se_3 films annealed at 300 and 350 °C has desired structural and optical properties in terms of photovoltaic applications. Therefore, it is concluded that annealing of Sb_2Se_3 films neither above and nor below these temperatures is not suitable.

Superstrate structure solar cells consist of different buffer layer parameters regarding oxygen ratio. When SolarCell-1 and SolarCell-2 are compared, all layers except the Zn(O,S) buffer layer have been grown at the same parameters. Increasing the oxygen amount from 0.5 sccm to 1.0 sccm while depositing the Zn(O,S) buffer layer, resulted in an increase in the short-circuit current density and a decrease in the open-circuit voltage. We could not calculate the series resistance of our SolarCell-1 and SolarCell-2 solar, but we observed the change depending on the oxygen ratio in the Zn(O,S) buffer layer. Nevertheless, both solar cells have low open circuit voltages and low short circuit currents. These results show that the diffusion lengths and lifetimes of minority carriers are quite low due to excessive recombination. Although we expect diode characteristic at forward bias, we observed a kink-like shape I-V curves of SolarCell-1 and SolarCell-2 under illumination which indicates a strong distortion of the I-V curve. Because of this distortion, short-circuit current density and fill factor (FF) values are low. The presence of a heterojunction barrier at absorber/buffer interface may leads to distortion (Pudov et al. 2005). A secondary barrier caused by the rising positive conduction band discontinuity at the buffer-absorber (Zn(O,S)/Sb_2Se_3) interface causes current limitation (Pudov et al. 2005). The spike between the buffer and the absorber layer creates a secondary barrier. The conduction band offset between Sb_2Se_3 and Zn(O,S), the electron doping density of Zn(O,S) and the band gap energy value of Zn(O,S) are the main factors affecting the barrier height. If the barrier level is high, it can limit electron transportation

correspondingly lead to I–V distortion. Therefore, the barrier height between Sb_2Se_3/Zn(O,S) junction plays an important role in the distortions of the J-V curve (Gharibshahian, Orouji, and Sharbati 2021). Furthermore, the sulfur concentration in the Zn(O,S) buffer layer can affect the performance of Sb_2Se_3/Zn(O,S) solar cell. It is stated that the light/dark J-V distortion depends on the sulfur content in the Zn(O,S) (Gharibshahian, Orouji, and Sharbati 2021). However, until now, there is no experimental study on the Zn(O,S)/Sb_2Se_3 interface in the literature. Hence, the comments made on I-V analyses were based on the results obtained from other solar cells studied.

Two different solar cells were grown with single buffer layer SolarCell-3 (CdS/ Sb_2Se_3) and double buffer layer SolarCell-4 (CdS/ ZnS/ Sb_2Se_3), respectively. Efficiency values obtained 2.19 % and 0.26% for the single buffer layer and double buffer layer cell, respectively. I-V curves measured under dark and illuminated conditions did not overlap, they showed a cross over. There are many reasons for this. One of these reasons is the formation of a Schottky barrier between the back contact metal and the absorber layer, which limits the hole transmission from the back contact metal to the absorber layer. (K. Wang et al. 2011). Another reason is the use of CdS as a buffer layer with the Sb_2Se_3 absorber layer in this solar cell configuration. Considering the literature, it has been observed that the J-V curves measured under illuminated and dark conditions for the solar cells CIGS/CdS and CZTSSe/CdS, show a cross over as a result of photoexcitation in the CdS buffer layer (Meher, Balakrishnan, and Alex 2016). Based on this situation, the photo-doping of the CdS buffer layer is probably the reason of the crossover in Sb_2Se_3-based structures.

The presence of Cd vacancies (V_{Cd}) in the CdS buffer layer causes the illumination dependent deep acceptor-like trap states (Neuschitzer et al. 2015). In dark condition of the solar cell, these acceptors capture the electrons and negatively charged. They partially contribute to n-type doping of CdS because there are no available photo-generated holes in CdS layer to neutralize these acceptor states (Chung et al. 2014). As a result, more negatively charged spaces are created within the CdS buffer layer under equilibrium state. This reduces conduction band bending thus, resulting increment in spike type band alignment (Buffière et al. 2014). Under illumination, the behavior of these deep acceptor-like trap states is different. When the solar cell is illuminated, electron-hole pairs are generated due to the absorption of photons by the CdS buffer layer. Holes are captured and neutralized by these deep acceptor-like trap states. Depending on this, the barrier

height decreases at the interface between the absorber-buffer layers. Barrier height is important in spike-type band alignment because it acts as a barrier to electrons. The presence of photosensitive defects inside the buffer layer causes a cross over in the solar cell's J-V curves due to the variation in spike-type barrier height. In the literature, this is also the case in solar cells in Sb_2Se_3/CdS junction.

Leng et al. found that the cause of the cross over they observed in the J-V curves is either by reason of the sharp conduction band or the electron barrier caused by the high acceptor density in the Sb_2Se_3 surface region, which may be filled during illumination (Leng et al. 2014). If the crossover is observed under the illuminated and dark J-V curves at high voltage values, it explains that the electron barrier formed between CdS/Sb_2Se_3 was reduced. However, in J-V graphs of SolarCell-3 and SolarCell-4, the cross over was observed at every point in the range of 200 to 400 mV. The observation from results is that the electron barrier formed at the CdS/Sb_2Se_3 interface has remained almost constant on the solar cell.

REFERENCES

Aly, S. A., and Alaa A. Akl. 2015. “Influence of Film Thickness on Optical Absorption and Energy Gap of Thermally Evaporated CdS0.1Se0.9 Thin Films.” *Chalcogenide Letters*.

Arshi, Nishat, Junqing Lu, Yun Kon Joo, Chan Gyu Lee, Jae Hong Yoon, and Faheem Ahmed. 2012. “Study on Structural, Morphological and Electrical Properties of Sputtered Titanium Nitride Films under Different Argon Gas Flow.” *Materials Chemistry and Physics*. https://doi.org/10.1016/j.matchemphys.2012.03.078.

Aryanto, D., P. Marwoto, T. Sudiro, A. S. Wismogroho, and S. Sugianto. 2019. “Growth of A-Axis-Oriented Al-Doped ZnO Thin Film on Glass Substrate Using Unbalanced DC Magnetron Sputtering.” In *Journal of Physics: Conference Series*. https://doi.org/10.1088/1742-6596/1191/1/012031.

Babu, Majibul Haque, Bidhan Chandra Dev, and Jiban Podder. 2019. “Texture Coefficient and Band Gap Tailoring of Fe-Doped SnO2 Nanoparticles via Thermal Spray Pyrolysis.” *Rare Metals*. https://doi.org/10.1007/s12598-019-01278-3.

Baines, Tom, Guillaume Zoppi, Leon Bowen, Thomas P. Shalvey, Silvia Mariotti, Ken Durose, and Jonathan D. Major. 2018. “Incorporation of CdSe Layers into CdTe Thin Film Solar Cells.” *Solar Energy Materials and Solar Cells*. https://doi.org/10.1016/j.solmat.2018.03.010.

Bhattacharya, R. N., K. Ramanathan, L. Gedvilas, and B. Keyes. 2005. “Cu(In,Ga)Se2 Thin-Film Solar Cells with ZnS(O,OH), Zn-Cd-S(O,OH), and CdS Buffer Layers.” In *Journal of Physics and Chemistry of Solids*. https://doi.org/10.1016/j.jpcs.2005.09.006.

Browning, Robert, Neal Kuperman, Bill Moon, and Raj Solanki. 2017. “Atomic Layer Growth of InSe and Sb2Se3 Layered Semiconductors and Their Heterostructure.” *Electronics (Switzerland)*. https://doi.org/10.3390/electronics6020027.

Buffière, M., G. Brammertz, S. Oueslati, H. El Anzeery, J. Bekaert, K. Ben Messaoud, C. Köble, S. Khelifi, M. Meuris, and J. Poortmans. 2014. “Spectral Current-Voltage

Analysis of Kesterite Solar Cells." *Journal of Physics D: Applied Physics*. https://doi.org/10.1088/0022-3727/47/17/175101.

Buffière, M., S. Harel, L. Arzel, C. Deudon, N. Barreau, and J. Kessler. 2011. "Fast Chemical Bath Deposition of Zn(O,S) Buffer Layers for Cu(In,Ga)Se 2 Solar Cells." In *Thin Solid Films*. https://doi.org/10.1016/j.tsf.2011.01.104.

Buffière, M., S. Harel, C. Guillot-Deudon, L. Arzel, N. Barreau, and J. Kessler. 2015. "Effect of the Chemical Composition of Co-Sputtered Zn(O,S) Buffer Layers on Cu(In,Ga)Se2 Solar Cell Performance." *Physica Status Solidi (A) Applications and Materials Science*. https://doi.org/10.1002/pssa.201431388.

Buldu, Dilara Gokcen, Ayten Cantas, Fulya Turkoglu, Fatime Gulsah Akca, Ece Meric, Mehtap Ozdemir, Enver Tarhan, Lutfi Ozyuzer, and Gulnur Aygun. 2018. "Influence of Sulfurization Temperature on Cu2ZnSnS4 Absorber Layer on Flexible Titanium Substrates for Thin Film Solar Cells." *Physica Scripta*. https://doi.org/10.1088/1402-4896/aa95eb.

Caglar, Mujdat, Saliha Ilican, Yasemin Caglar, and Fahrettin Yakuphanoglu. 2009. "Electrical Conductivity and Optical Properties of ZnO Nanostructured Thin Film." *Applied Surface Science*. https://doi.org/10.1016/j.apsusc.2008.11.055.

Cantas, A., F. Turkoglu, E. Meric, F. G. Akca, M. Ozdemir, E. Tarhan, L. Ozyuzer, and G. Aygun. 2018. "Importance of CdS Buffer Layer Thickness on Cu2ZnSnS4-Based Solar Cell Efficiency." *Journal of Physics D: Applied Physics*. https://doi.org/10.1088/1361-6463/aac8d3.

Caracas, Razvan, and Xavier Gonze. 2005. "First-Principles Study of the Electronic Properties of A2 B3 Minerals, with A=Bi,Sb and B=S,Se." *Physics and Chemistry of Minerals*. https://doi.org/10.1007/s00269-005-0470-y.

Carlson, D. E., and C. R. Wronski. 1976. "Amorphous Silicon Solar Cell." *Applied Physics Letters*. https://doi.org/10.1063/1.88617.

Chen, Chao, David C. Bobela, Ye Yang, Shuaicheng Lu, Kai Zeng, Cong Ge, Bo Yang, et al. 2017. "Characterization of Basic Physical Properties of Sb2Se3 and Its Relevance for Photovoltaics." *Frontiers of Optoelectronics* 10 (1): 18–30.

https://doi.org/10.1007/s12200-017-0702-z.

Chen, Chao, Weiqi Li, Ying Zhou, Cheng Chen, Miao Luo, Xinsheng Liu, Kai Zeng, et al. 2015. “Optical Properties of Amorphous and Polycrystalline Sb2Se3 Thin Films Prepared by Thermal Evaporation.” *Applied Physics Letters*. https://doi.org/10.1063/1.4927741.

Chen, Chao, Liang Wang, Liang Gao, Dahyun Nam, Dengbing Li, Kanghua Li, Yang Zhao, et al. 2017. “6.5% Certified Efficiency Sb2Se3 Solar Cells Using PbS Colloidal Quantum Dot Film as Hole-Transporting Layer.” *ACS Energy Letters*. https://doi.org/10.1021/acsenergylett.7b00648.

Chen, Haining, Weiping Li, Huicong Liu, and Liqun Zhu. 2010. “A Suitable Deposition Method of CdS for High Performance CdS-Sensitized ZnO Electrodes: Sequential Chemical Bath Deposition.” *Solar Energy*. https://doi.org/10.1016/j.solener.2010.03.026.

Chen, Zhiwen, Xiaohai Guo, Huafei Guo, Changhao Ma, Jianhua Qiu, Ningyi Yuan, and Jianning Ding. 2019. “Fabrication of a Semi-Transparent Thin-Film Sb2Se3 Solar Cell.” *Materials Letters* 236: 503–5. https://doi.org/10.1016/j.matlet.2018.10.173.

Chin, Hui Shun, Kuan Yew Cheong, and Khairunisak Abdul Razak. 2010. “Review on Oxides of Antimony Nanoparticles: Synthesis, Properties, and Applications.” *Journal of Materials Science*. https://doi.org/10.1007/s10853-010-4849-x.

Choi, Yong Chan, Tarak Nath Mandal, Woon Seok Yang, Yong Hui Lee, Sang Hyuk Im, Jun Hong Noh, and Sang Il Seok. 2014. “Sb2Se3-Sensitized Inorganic-Organic-Heterojunction Solar Cells Fabricated Using a Single-Source Precursor.” *Angewandte Chemie - International Edition*. https://doi.org/10.1002/anie.201308331.

Chung, Choong Heui, Brion Bob, Tze Bin Song, and Yang Yang. 2014. “Current-Voltage Characteristics of Fully Solution Processed High Performance CuIn(S,Se)2 Solar Cells: Crossover and Red Kink.” *Solar Energy Materials and Solar Cells*. https://doi.org/10.1016/j.solmat.2013.10.013.

Cui, Hongtao, Chang Yeh Lee, Wei Li, Xiaolei Liu, Xiaoming Wen, and Xiaojing Hao.

2015. “Improving Efficiency of Evaporated Cu2ZnSnS4 Thin Film Solar Cells by a Thin Ag Intermediate Layer between Absorber and Back Contact.” *International Journal of Photoenergy*. https://doi.org/10.1155/2015/170507.

Demirhan, Yasemin, Hasan Koseoglu, Fulya Turkoglu, Zemzem Uyanik, Mehtap Ozdemir, Gulnur Aygun, and Lutfi Ozyuzer. 2020. “The Controllable Deposıtıon of Large Area Roll-to-Roll Sputtered Ito Thın Fılms for Photovoltaıc Applıcatıons.” *Renewable Energy*. https://doi.org/10.1016/j.renene.2019.07.038.

Deulkar, Sundeep H., Jow Lay Huang, and Michael Neumann-Spallart. 2010. “Zinc Oxysulfide Thin Films Grown by Pulsed Laser Deposition.” In *Journal of Electronic Materials*. https://doi.org/10.1007/s11664-009-1069-8.

Efthimiopoulos, Ilias, Jiaming Zhang, Melvin Kucway, Changyong Park, Rodney C. Ewing, and Yuejian Wang. 2013. “Sb2Se3 under Pressure.” *Scientific Reports* 3. https://doi.org/10.1038/srep02665.

Eicke, Axel, Thomas Ciba, Dimitrios Hariskos, Richard Menner, Carsten Tschamber, and Wolfram Witte. 2013. “Depth Profiling with SNMS and SIMS of Zn(O,S) Buffer Layers for Cu(In,Ga)Se2 Thin-Film Solar Cells.” *Surface and Interface Analysis*. https://doi.org/10.1002/sia.5325.

Escorcia-García, J., M. Domínguez-Díaz, A. Hernández-Granados, and H. Martínez. 2018. “Antimony Sulfide Thin Films Obtained by Chemical Bath Deposition Using Tartaric Acid as Complexing Agent.” In *MRS Advances*. https://doi.org/10.1557/adv.2018.551.

Fleck, Nicole, Oliver S. Hutter, Laurie J. Phillips, Huw Shiel, Theodore D.C. Hobson, Vin R. Dhanak, Tim D. Veal, Frank Jäckel, Ken Durose, and Jonathan D. Major. 2020. “How Oxygen Exposure Improves the Back Contact and Performance of Antimony Selenide Solar Cells.” *ACS Applied Materials and Interfaces*. https://doi.org/10.1021/acsami.0c14256.

Friedlmeier, Theresa Magorian, Philip Jackson, Andreas Bauer, Dimitrios Hariskos, Oliver Kiowski, Roland Wuerz, and Michael Powalla. 2015. “Improved Photocurrent in Cu(In,Ga)Se2 Solar Cells: From 20.8% to 21.7% Efficiency with CdS Buffer and 21.0% Cd-Free.” *IEEE Journal of Photovoltaics*.

https://doi.org/10.1109/JPHOTOV.2015.2458039.

Gharibshahian, Iman, Ali A. Orouji, and Samaneh Sharbati. 2021. “Effect of the Junction Barrier on Current–Voltage Distortions in the Sb2Se3/Zn(O,S) Solar Cells.” *Optical Materials*. https://doi.org/10.1016/j.optmat.2021.111098.

Ghasemi Varnamkhasti, Mohsen, Hamid Reza Fallah, Mojtaba Mostajaboddavati, and Ali Hassanzadeh. 2012. “Influence of Ag Thickness on Electrical, Optical and Structural Properties of Nanocrystalline MoO 3/Ag/ITO Multilayer for Optoelectronic Applications.” In *Vacuum*. https://doi.org/10.1016/j.vacuum.2011.12.002.

Green, Martin A., Yoshihiro Hishikawa, Ewan D. Dunlop, Dean H. Levi, Jochen Hohl-Ebinger, and Anita W.Y. Ho-Baillie. 2018. “Solar Cell Efficiency Tables (Version 51).” *Progress in Photovoltaics: Research and Applications*. https://doi.org/10.1002/pip.2978.

Green, Martin A., Yoshihiro Hishikawa, Wilhelm Warta, Ewan D. Dunlop, Dean H. Levi, Jochen Hohl-Ebinger, and Anita W.H. Ho-Baillie. 2017. “Solar Cell Efficiency Tables (Version 50).” *Progress in Photovoltaics: Research and Applications*. https://doi.org/10.1002/pip.2909.

Grimm, A., J. Just, D. Kieven, I. Lauermann, J. Palm, A. Neisser, T. Rissom, and R. Klenk. 2010. “Sputtered Zn(O,S) for Junction Formation in Chalcopyrite-Based Thin Film Solar Cells.” *Physica Status Solidi - Rapid Research Letters*. https://doi.org/10.1002/pssr.201004083.

Grimm, A., D. Kieven, R. Klenk, I. Lauermann, A. Neisser, T. Niesen, and J. Palm. 2011. “Junction Formation in Chalcopyrite Solar Cells by Sputtered Wide Gap Compound Semiconductors.” In *Thin Solid Films*. https://doi.org/10.1016/j.tsf.2011.04.150.

Guchhait, Asim, Zhenghua Su, Ying Fan Tay, Sudhanshu Shukla, Wenjie Li, Shin Woei Leow, Joel Ming Rui Tan, Stener Lie, Oki Gunawan, and Lydia Helena Wong. 2016. “Enhancement of Open-Circuit Voltage of Solution-Processed Cu2ZnSnS4 Solar Cells with 7.2% Efficiency by Incorporation of Silver.” *ACS Energy Letters*. https://doi.org/10.1021/acsenergylett.6b00509.

Guillemoles, J. F. 2002. “The Puzzle of Cu(In,Ga)Se2 (CIGS) Solar Cells Stability.” In *Thin Solid Films*. https://doi.org/10.1016/S0040-6090(01)01519-X.

Harif, Muhammad Najib, Kazi Sajedur Rahman, Hasrul Nisham Rosly, Puvaneswaran Chelvanathan, Camellia Doroody, Halina Misran, and Nowshad Amin. 2020. “An Approach to Alternative Post-Deposition Treatment in CdTe Thin Films for Solar Cell Application.” *Superlattices and Microstructures*. https://doi.org/10.1016/j.spmi.2020.106687.

Hervé, P., and L. K.J. Vandamme. 1994. “General Relation between Refractive Index and Energy Gap in Semiconductors.” *Infrared Physics and Technology*. https://doi.org/10.1016/1350-4495(94)90026-4.

Huang, Chia Hua, Wen Jie Chuang, Chun Ping Lin, Yueh Lin Jan, and Yu Chiu Shih. 2018. “Deposition Technologies of High-Efficiency Cigs Solar Cells: Development of Two-Step and Co-Evaporation Processes.” *Crystals*. https://doi.org/10.3390/cryst8070296.

Jadhavar, Pradeep, Maulikkumar Vaja, Tejas Dhameliya, and Asit Chakraborti. 2015. “Oxazolidinones as Anti-Tubercular Agents: Discovery, Development and Future Perspectives.” *Current Medicinal Chemistry*. https://doi.org/10.2174/0929867323666151106125759.

Jang, Soohwan, Byoung Sam Kang, Fan Ren, N W. Emanetoglu, H Shen, W H. Chang, Brent Gila, M Hlad, and Steve Pearton. 2007. “Comparison of E-Beam and Sputter-Deposited ITO Films for 1.55 Um Metal-Semiconductor-Metal Photo-Detector Applications.” *ECS Transactions*. https://doi.org/10.1149/1.2731172.

Jha, Sunil Kr, Jasmin Bilalovic, Anju Jha, Nilesh Patel, and Han Zhang. 2017. “Renewable Energy: Present Research and Future Scope of Artificial Intelligence.” *Renewable and Sustainable Energy Reviews*. https://doi.org/10.1016/j.rser.2017.04.018.

Ju, Taifeng, Bonkee Koo, Jea Woong Jo, and Min Jae Ko. 2020. “Enhanced Photovoltaic Performance of Solution-Processed Sb2Se3 Thin Film Solar Cells by Optimizing Device Structure.” *Current Applied Physics*. https://doi.org/10.1016/j.cap.2019.11.018.

Kamada, Rui, Takeshi Yagioka, Shunsuke Adachi, Atsushi Handa, Kong Fai Tai, Takuya Kato, and Hiroki Sugimoto. 2017. "New World Record Cu(In,Ga)(Se,S)2 Thin Film Solar Cell Efficiency beyond 22%." In *2017 IEEE 44th Photovoltaic Specialist Conference, PVSC 2017*. https://doi.org/10.1109/PVSC.2017.8366261.

Karim, Soumia, Nadia Machkour, Mourad Zegrari, Abdelhafid Aitelmahjoub, and Zakaria Sabiri. 2018. "Modeling Photovoltaic System Using MATLAB/Simulink." *SSRN Electronic Journal*. https://doi.org/10.2139/ssrn.3185323.

Kartopu, G., B. L. Williams, V. Zardetto, A. K. Gürlek, A. J. Clayton, S. Jones, W. M.M. Kessels, M. Creatore, and S. J.C. Irvine. 2019. "Enhancement of the Photocurrent and Efficiency of CdTe Solar Cells Suppressing the Front Contact Reflection Using a Highly-Resistive ZnO Buffer Layer." *Solar Energy Materials and Solar Cells*. https://doi.org/10.1016/j.solmat.2018.11.002.

Kessler, Friedrich, and Dominik Rudmann. 2004. "Technological Aspects of Flexible CIGS Solar Cells and Modules." *Solar Energy*. https://doi.org/10.1016/j.solener.2004.04.010.

Khojier, Kaykhosrow, Hadi Savaloni, Ebrahim Shokrai, Zohreh Dehghani, and Naser Dehnavi. 2013. "Influence of Argon Gas Flow on Mechanical and Electrical Properties of Sputtered Titanium Nitride Thin Films." *Journal of Theoretical and Applied Physics*. https://doi.org/10.1186/2251-7235-7-37.

Khudayer, Iman H. 2017. "Study of Physical and Optoelectronic Properties of CuInSe2/Si Heterojunction Solar Cells." In *Energy Procedia*. https://doi.org/10.1016/j.egypro.2017.07.062.

Kieven, D., A. Grimm, I. Lauermann, M. Ch Lux-Steiner, J. Palm, T. Niesen, and R. Klenk. 2012. "Band Alignment at Sputtered ZnS x O 1-x/Cu(In,Ga)(Se,S) 2 Heterojunctions." *Physica Status Solidi - Rapid Research Letters*. https://doi.org/10.1002/pssr.201206195.

Kittel, Charles. 2004. "Introduction to Solid State Physics, 8th Edition." *Wiley & Sons, New York, NY*.

Klenk, Reiner, Alexander Steigert, Thorsten Rissom, Dieter Greiner, Christian A.

Kaufmann, Thomas Unold, and Martha Ch Lux-Steiner. 2014. “Junction Formation by Zn(O,S) Sputtering Yields CIGSe-Based Cells with Efficiencies Exceeding 18%.” *Progress in Photovoltaics: Research and Applications*. https://doi.org/10.1002/pip.2445.

Kondrotas, Rokas, Jun Zhang, Chong Wang, and Jiang Tang. 2019. “Growth Mechanism of Sb2Se3 Thin Films for Photovoltaic Application by Vapor Transport Deposition.” *Solar Energy Materials and Solar Cells*. https://doi.org/10.1016/j.solmat.2019.04.024.

Kosarian, Abdolnabi, and Peyman Jelodarian. 2011. “Numerical Evaluation and Characterization of Single Junction Solar Cell Based on Thin-Film a-Si:H/a-SiGe:H Hetero-Structure.” In *2011 19th Iranian Conference on Electrical Engineering, ICEE 2011*.

Kumar, Mukesh, Ashish Dubey, Nirmal Adhikari, Swaminathan Venkatesan, and Qiquan Qiao. 2015. “Strategic Review of Secondary Phases, Defects and Defect-Complexes in Kesterite CZTS-Se Solar Cells.” *Energy and Environmental Science*. https://doi.org/10.1039/c5ee02153g.

Kushiya, Katsumi. 2004. “Development of Cu(InGa)Se2-Based Thin-Film PV Modules with a Zn(O,S,OH)x Buffer Layer.” *Solar Energy*. https://doi.org/10.1016/j.solener.2004.08.027.

Lai, Yanqing, Can Han, Xiaojun Lv, Jia Yang, Fangyang Liu, Jie Li, and Yexiang Liu. 2012. “Electrodeposition of Antimony Selenide Thin Films from Aqueous Acid Solutions.” *Journal of Electroanalytical Chemistry*. https://doi.org/10.1016/j.jelechem.2012.02.018.

Langford, J. I., and A. J. C. Wilson. 1978. “Scherrer after Sixty Years: A Survey and Some New Results in the Determination of Crystallite Size.” *Journal of Applied Crystallography*. https://doi.org/10.1107/s0021889878012844.

Leng, Meiying, Miao Luo, Chao Chen, Sikai Qin, Jie Chen, Jie Zhong, and Jiang Tang. 2014. “Selenization of Sb2Se3 Absorber Layer: An Efficient Step to Improve Device Performance of CdS/Sb2Se3 Solar Cells.” *Applied Physics Letters*. https://doi.org/10.1063/1.4894170.

Li, Gang, Zhiqiang Li, Jingwei Chen, Xu Chen, Shuang Qiao, Shufang Wang, Ying Xu, and Yaohua Mai. 2018. "Self-Powered, High-Speed Sb2Se3/Si Heterojunction Photodetector with Close Spaced Sublimation Processed Sb2Se3 Layer." *Journal of Alloys and Compounds*. https://doi.org/10.1016/j.jallcom.2017.12.039.

Li, Jian V., Darius Kuciauskas, Matthew R. Young, and Ingrid L. Repins. 2013. "Effects of Sodium Incorporation in Co-Evaporated Cu2ZnSnSe 4 Thin-Film Solar Cells." *Applied Physics Letters*. https://doi.org/10.1063/1.4802972.

Li, Kanghua, and Jiang Tang. 2018. "Super-Flexible Sb2Se3 Solar Cell." In *Optics InfoBase Conference Papers*. https://doi.org/10.1364/PFE.2018.PT4B.19.

Li, Zhiqiang, Xu Chen, Hongbing Zhu, Jingwei Chen, Yuting Guo, Chong Zhang, Wen Zhang, Xiaona Niu, and Yaohua Mai. 2017a. "Sb2Se3 Thin Film Solar Cells in Substrate Configuration and the Back Contact Selenization." *Solar Energy Materials and Solar Cells*. https://doi.org/10.1016/j.solmat.2016.11.033.

Li, Zhiqiang, Xiaoyang Liang, Gang Li, Haixu Liu, Huiyu Zhang, Jianxin Guo, Jingwei Chen, et al. 2019. "9.2%-Efficient Core-Shell Structured Antimony Selenide Nanorod Array Solar Cells." *Nature Communications*. https://doi.org/10.1038/s41467-018-07903-6.

Liang, Guang Xing, Zhuang Hao Zheng, Ping Fan, Jing Ting Luo, Ju Guang Hu, Xiang Hua Zhang, Hong Li Ma, Bo Fan, Zhong Kuan Luo, and Dong Ping Zhang. 2018a. "Thermally Induced Structural Evolution and Performance of Sb2Se3 Films and Nanorods Prepared by an Easy Sputtering Method." *Solar Energy Materials and Solar Cells*. https://doi.org/10.1016/j.solmat.2017.09.008.

Liang, Xiaoyang, Xu Chen, Zhiqiang Li, Gang Li, Jingwei Chen, Lin Yang, Kai Shen, Ying Xu, and Yaohua Mai. 2019. "Effect of Deposition Pressure on the Properties of Magnetron Sputtering-Deposited Sb2Se3 Thin-Film Solar Cells." *Applied Physics A: Materials Science and Processing*. https://doi.org/10.1007/s00339-019-2677-7.

Lindahl, Johan, Uwe Zimmermann, Piotr Szaniawski, Tobias Torndahl, Adam Hultqvist, Pedro Salomé, Charlotte Platzer-Björkman, and Marika Edoff. 2013. "Inline Cu(In,Ga)Se2 Co-Evaporation for High-Efficiency Solar Cells and Modules." *IEEE*

Journal of Photovoltaics. https://doi.org/10.1109/JPHOTOV.2013.2256232.

Lisco, F., P. M. Kaminski, A. Abbas, K. Bass, J. W. Bowers, G. Claudio, M. Losurdo, and J. M. Walls. 2015. "The Structural Properties of CdS Deposited by Chemical Bath Deposition and Pulsed Direct Current Magnetron Sputtering." In *Thin Solid Films*. https://doi.org/10.1016/j.tsf.2014.11.062.

Liu, Chunmin, Yafei Yuan, Ling Cheng, Jing Su, Xingtong Zhang, Xiangxiang Li, Hao Zhang, Min Xu, and Jing Li. 2019. "A Study on Optical Properties of Sb 2 Se 3 Thin Films and Resistive Switching Behavior in Ag/Sb 2 Se 3 /W Heterojunctions." *Results in Physics* 13 (December 2018): 102228. https://doi.org/10.1016/j.rinp.2019.102228.

Liu, Jinyang, Mingling Li, Mengyu Liu, Hongbing Cai, Yue Lin, Yuhan Zhou, Zhigao Huang, and Fachun Lai. 2020. "The High Anisotropy of the Epitaxial Growth of the Well-Aligned Sb2Se3 Nanoribbons on Mica." *ACS Applied Materials and Interfaces*. https://doi.org/10.1021/acsami.9b20142.

Liu, Xinsheng, Xun Xiao, Ye Yang, Ding Jiang Xue, Deng Bing Li, Chao Chen, Shuaicheng Lu, et al. 2017. "Enhanced Sb2Se3 Solar Cell Performance through Theory-Guided Defect Control." *Progress in Photovoltaics: Research and Applications*. https://doi.org/10.1002/pip.2900.

Locmelis, S., C. Brünig, M. Binnewies, A. Börger, K. D. Becker, T. Homann, and T. Bredow. 2007. "Optical Band Gap in the System ZnO1-XSx. An Experimental and Quantum Chemical Study." In *Journal of Materials Science*. https://doi.org/10.1007/s10853-006-0415-y.

Meher, S. R., L. Balakrishnan, and Z. C. Alex. 2016. "Analysis of Cu2ZnSnS4/CdS Based Photovoltaic Cell: A Numerical Simulation Approach." *Superlattices and Microstructures*. https://doi.org/10.1016/j.spmi.2016.10.028.

Meier, Daniel L., Vinodh Chandrasekaran, Atul Gupta, Vijay Yelundur, and Ajeet Rohatgi. 2013. "Silver Contact Grid: Inferred Contact Resistivity and Cost Minimization in 19% Silicon Solar Cells." *IEEE Journal of Photovoltaics*. https://doi.org/10.1109/JPHOTOV.2012.2217939.

Messina, Sarah, M. T. S. Nair, and P. K. Nair. 2009. “Antimony Selenide Absorber Thin Films in All-Chemically Deposited Solar Cells.” *Journal of The Electrochemical Society*. https://doi.org/10.1149/1.3089358.

Meyer, B. K., A. Polity, B. Farangis, Y. He, D. Hasselkamp, Th Krämer, and C. Wang. 2004. “Structural Properties and Bandgap Bowing of ZnO1-x Sx Thin Films Deposited by Reactive Sputtering.” *Applied Physics Letters*. https://doi.org/10.1063/1.1825053.

Muffler, Hans J., Marcus Bär, Christian H. Fischer, Robert Gay, Franz Karg, and Martha C. Lux-Steiner. 2000. “Ilgar Technology. VIII. Sulfidic Buffer Layers for Cu(InGa)(S,Se)2 Solar Cells Prepared by Ion Layer Gas Reaction (ILGAR).” In *Conference Record of the IEEE Photovoltaic Specialists Conference*. https://doi.org/10.1109/PVSC.2000.915916.

Nagata, Kiyofumi, Katsunori Ishibashi, and Yasuhiko Miyamoto. 1981. “Raman and Infrared Spectra of Rhombohedral Selenium.” *Japanese Journal of Applied Physics* 20 (3): 463–69. https://doi.org/10.1143/JJAP.20.463.

Nakada, Tokio, and Masayuki Mizutani. 2000. “Improved Efficiency of Cu(In,Ga)Se2 Thin Film Solar Cells with Chemically Deposited ZnS Buffer Layers by Air-Annealing-Formation of Homojunction by Solid Phase Diffusion.” In *Conference Record of the IEEE Photovoltaic Specialists Conference*. https://doi.org/10.1109/PVSC.2000.915889.

Nakamura, Kyotaro, Masahiro Gotoh, Toshihiko Fujihara, Toshihiko Toyama, and Hiroaki Okamoto. 2003. “Influence of CdS Window Layer on 2-Mm Thick CdS/CdTe Thin Film Solar Cells.” *Solar Energy Materials and Solar Cells*. https://doi.org/10.1016/S0927-0248(02)00154-X.

Nakamura, Motoshi, Yamaguchi Kouji, Yoshiyuki Chiba, Hideki Hakuma, Taizo Kobayashi, and Tokio Nakada. 2013. “Achievement of 19.7% Efficiency with a Small-Sized Cu(InGa)(SeS) 2 Solar Cells Prepared by Sulfurization after Selenizaion Process with Zn-Based Buffer.” In *Conference Record of the IEEE Photovoltaic Specialists Conference*. https://doi.org/10.1109/PVSC.2013.6744278.

Nelson, Jenny. 2003. *The Physics of Solar Cells*. *The Physics of Solar Cells*.

https://doi.org/10.1142/p276.

Neuschitzer, Markus, Yudania Sanchez, Simon Lõpez-Marino, Haibing Xie, Andrew Fairbrother, Marcel Placidi, Stefan Haass, Victor Izquierdo-Roca, Alejandro Perez-Rodriguez, and Edgardo Saucedo. 2015. "Optimization of CdS Buffer Layer for High-Performance Cu2ZnSnSe4 Solar Cells and the Effects of Light Soaking: Elimination of Crossover and Red Kink." *Progress in Photovoltaics: Research and Applications*. https://doi.org/10.1002/pip.2589.

Oluwaleye, O., M. Madhuku, B. Mwakikunga, and S. J. Moloi. 2019. "Studies of Lattice Structure, Electrical Properties, Thermal and Chemical Stability of Cobalt Ion Implanted Indium Tin Oxide (ITO) Thin Films on Polymer Substrates." *Nuclear Instruments and Methods in Physics Research, Section B: Beam Interactions with Materials and Atoms*. https://doi.org/10.1016/j.nimb.2018.10.014.

Ovshinsky, Stanford R., and David Adler. 1978. "Local Structure, Bonding, and Electronic Properties of Covalent Amorphous Semiconductors." *Contemporary Physics*. https://doi.org/10.1080/00107517808210876.

Pan, H. L., T. Yang, B. Yao, R. Deng, R. Y. Sui, L. L. Gao, and D. Z. Shen. 2010. "Characterization and Properties of ZnO 1-x S x Alloy Films Fabricated by Radio-Frequency Magnetron Sputtering." *Applied Surface Science*. https://doi.org/10.1016/j.apsusc.2010.02.061.

Pandey, Shiv K., Shipra Pandey, Avinash C. Pandey, and G. K. Mehrotra. 2013. "Zinc Oxysulfide Ternary Alloy Nanocrystals: A Bandgap Modulated Photocatalyst." *Applied Physics Letters*. https://doi.org/10.1063/1.4810910.

Pandey, Shiv K., Shipra Pandey, Vyom Parashar, Raghvendra S. Yadav, G. K. Mehrotra, and Avinash C. Pandey. 2014. "Bandgap Engineering of Colloidal Zinc Oxysulfide via Lattice Substitution with Sulfur." *Nanoscale*. https://doi.org/10.1039/c3nr04457b.

Platzer-Björkman, C., J. Lu, J. Kessler, and L. Stolt. 2003. "Interface Study of CuInSe2/ZnO and Cu(In,Ga)Se2/ZnO Devices Using ALD ZnO Buffer Layers." In *Thin Solid Films*. https://doi.org/10.1016/S0040-6090(03)00229-3.

Platzer-Björkman, C., T. Törndahl, D. Abou-Ras, J. Malmström, J. Kessler, and L. Stolt. 2006. “Zn(O, S) Buffer Layers by Atomic Layer Deposition in Cu(In, Ga)Se 2 Based Thin Film Solar Cells: Band Alignment and Sulfur Gradient.” *Journal of Applied Physics*. https://doi.org/10.1063/1.2222067.

Powalla, Michael, Stefan Paetel, Erik Ahlswede, Roland Wuerz, Cordula D. Wessendorf, and Theresa Magorian Friedlmeier. 2018. “Thin-Film Solar Cells Exceeding 22% Solar Cell Efficiency: An Overview on CdTe-, Cu(In,Ga)Se 2 -, and Perovskite-Based Materials.” *Applied Physics Reviews*. https://doi.org/10.1063/1.5061809.

Pudov, A. O., A. Kanevce, H. A. Al-Thani, J. R. Sites, and F. S. Hasoon. 2005. “Secondary Barriers in CdS- CuIn1-x Gax Se2 Solar Cells.” *Journal of Applied Physics*. https://doi.org/10.1063/1.1850604.

Rabeh, M. Ben, N. Khedmi, M. A. Fodha, and M. Kanzari. 2014. “The Effect of Thickness on Optical Band Gap and N-Type Conductivity of CuInS2 Thin Films Annealed in Air Atmosphere.” In *Energy Procedia*. https://doi.org/10.1016/j.egypro.2013.12.009.

Ramanujam, Jeyakumar, and Udai P. Singh. 2017. “Copper Indium Gallium Selenide Based Solar Cells - A Review.” *Energy and Environmental Science*. https://doi.org/10.1039/c7ee00826k.

Ren, Donglou, Xue Luo, Shuo Chen, Zhuanghao Zheng, Michel Cathelinaud, Guangxing Liang, Hongli Ma, Xvsheng Qiao, Xianping Fan, and Xianghua Zhang. 2020. “Structure, Morphology, and Photoelectric Performances of Te-Sb2se3 Thin Film Prepared via Magnetron Sputtering.” *Nanomaterials*. https://doi.org/10.3390/nano10071358.

Romeo, N., A. Bosio, and A. Romeo. 2010. “An Innovative Process Suitable to Produce High-Efficiency CdTe/CdS Thin-Film Modules.” *Solar Energy Materials and Solar Cells*. https://doi.org/10.1016/j.solmat.2009.06.001.

Sabbagh, Harold A. 1977. “Calculation of Electroacoustic Sensitivity of Radially Polarized Ferroelectric Cylinders by Normal-Mode Methods.” *Journal of the Acoustical Society of America*. https://doi.org/10.1121/1.381412.

Sáez-Araoz, R., A. Ennaoui, T. Kropp, E. Veryaeva, T. P. Niesen, and M. Ch Lux-Steiner. 2008. “Use of Different Zn Precursors for the Deposition of Zn(S,O) Buffer Layers by Chemical Bath for Chalcopyrite Based Cd-Free Thin-Film Solar Cells.” *Physica Status Solidi (A) Applications and Materials Science*. https://doi.org/10.1002/pssa.200779421.

Sanders, B. W., and A. Kitai. 1992. “Zinc Oxysulfide Thin Films Grown by Atomic Layer Deposition.” *Chemistry of Materials*. https://doi.org/10.1021/cm00023a015.

Scherrer, P. 1918. “Determination of the Internal Structure and Size of Colloid Particles by X-Rays.” *Göttinger Nachrichten Gesell*.

Shen, Kai, Chizhu Ou, Tailang Huang, Hongbing Zhu, Jianjun Li, Zhiqiang Li, and Yaohua Mai. 2018. “Mechanisms and Modification of Nonlinear Shunt Leakage in Sb2Se3 Thin Film Solar Cells.” *Solar Energy Materials and Solar Cells*. https://doi.org/10.1016/j.solmat.2018.06.022.

Shiel, Huw, Oliver S. Hutter, Laurie J. Phillips, Mohammed Al Turkestani, Vin R. Dhanak, Tim D. Veal, Ken Durose, and Jonathan D. Major. 2019. “Chemical Etching of Sb2Se3 Solar Cells: Surface Chemistry and Back Contact Behaviour.” *JPhys Energy*. https://doi.org/10.1088/2515-7655/ab3c98.

Shockley, William, Hans Queisser, and Hans J Queisser. 1961. “The Shockley-Queisser Limit.” *Journal of Applied Physics*.

Shongalova, A., M. R. Correia, J. P. Teixeira, J. P. Leitão, J. C. González, S. Ranjbar, S. Garud, et al. 2018. “Growth of Sb2Se3 Thin Films by Selenization of RF Sputtered Binary Precursors.” *Solar Energy Materials and Solar Cells* 187 (October): 219–26. https://doi.org/10.1016/j.solmat.2018.08.003.

Shongalova, A., M. R. Correia, B. Vermang, J. M.V. Cunha, P. M.P. Salomé, and P. A. Fernandes. 2018. “On the Identification of Sb2Se3 Using Raman Scattering.” *MRS Communications* 8 (3): 865–70. https://doi.org/10.1557/mrc.2018.94.

Sinsermsuksakul, Prasert, Katy Hartman, Sang Bok Kim, Jaeyeong Heo, Leizhi Sun, Helen Hejin Park, Rupak Chakraborty, Tonio Buonassisi, and Roy G. Gordon. 2013. “Enhancing the Efficiency of SnS Solar Cells via Band-Offset Engineering with a

Zinc Oxysulfide Buffer Layer." *Applied Physics Letters*. https://doi.org/10.1063/1.4789855.

Socol, Marcela, Nicoleta Preda, Oana Rasoga, Andreea Costas, Anca Stanculescu, Carmen Breazu, Florin Gherendi, and Gabriel Socol. 2019. "Pulsed Laser Deposition of Indium Tin Oxide Thin Films on Nanopatterned Glass Substrates." *Coatings*. https://doi.org/10.3390/coatings9010019.

Song, Chunyan, Nan Zhang, Jie Lin, Xiaoyang Guo, and Xingyuan Liu. 2017. "Sb2O3/Ag/Sb2O3 Multilayer Transparent Conducting Films for Ultraviolet Organic Light-Emitting Diode." *Scientific Reports*. https://doi.org/10.1038/srep41250.

Sönmezolu, Savaş, Aysun Arslan, Tülay Serin, and Necmi Serin. 2011. "The Effects of Film Thickness on the Optical Properties of TiO 2-SnO2 Compound Thin Films." *Physica Scripta*. https://doi.org/10.1088/0031-8949/84/06/065602.

Srikant, V., and D. R. Clarke. 1998. "On the Optical Band Gap of Zinc Oxide." *Journal of Applied Physics*. https://doi.org/10.1063/1.367375.

Sun, Leizhi, Richard Haight, Prasert Sinsermsuksakul, Sang Bok Kim, Helen H. Park, and Roy G. Gordon. 2013. "Band Alignment of SnS/Zn(O,S) Heterojunctions in SnS Thin Film Solar Cells." *Applied Physics Letters*. https://doi.org/10.1063/1.4821433.

Sze, S.M., and Kwok K. Ng. 2006. *Physics of Semiconductor Devices*. *Physics of Semiconductor Devices*. https://doi.org/10.1002/0470068329.

Tajima, Shin, Mitsutaro Umehara, Masaki Hasegawa, Takahiro Mise, and Tadayoshi Itoh. 2017. "Cu2ZnSnS4 Photovoltaic Cell with Improved Efficiency Fabricated by High-Temperature Annealing after CdS Buffer-Layer Deposition." *Progress in Photovoltaics: Research and Applications*. https://doi.org/10.1002/pip.2837.

Tang, Rong, Zhuang Hao Zheng, Zheng Hua Su, Xue Jin Li, Ya Dong Wei, Xiang Hua Zhang, Yong Qing Fu, Jing Ting Luo, Ping Fan, and Guang Xing Liang. 2019. "Highly Efficient and Stable Planar Heterojunction Solar Cell Based on Sputtered and Post-Selenized Sb2Se3 Thin Film." *Nano Energy* 64 (June): 103929. https://doi.org/10.1016/j.nanoen.2019.103929.

Tao, Jiahua, Xiaobo Hu, Yixin Guo, Jin Hong, Kanghua Li, Jinchun Jiang, Shaoqiang Chen, et al. 2019. “Solution-Processed SnO 2 Interfacial Layer for Highly Efficient Sb 2 Se 3 Thin Film Solar Cells.” *Nano Energy* 60 (February): 802–9. https://doi.org/10.1016/j.nanoen.2019.04.019.

Tao, Jiahua, Xiaobo Hu, Juanjuan Xue, Youyang Wang, Guoen Weng, Shaoqiang Chen, Ziqiang Zhu, and Junhao Chu. 2019. “Investigation of Electronic Transport Mechanisms in Sb 2 Se 3 Thin-Film Solar Cells.” *Solar Energy Materials and Solar Cells* 197 (February): 1–6. https://doi.org/10.1016/j.solmat.2019.04.003.

Tideswell, N. W., and J. D. McCullough. 1957. “The Dissociation Constants of Some Dihalides of Dimethyl Sulfide and Dimethyl Selenide in Carbon Tetrachloride Solution.” *Journal of the American Chemical Society*. https://doi.org/10.1021/ja01562a005.

Tuna, Ocal, Yusuf Selamet, Gulnur Aygun, and Lutfi Ozyuzer. 2010. “High Quality ITO Thin Films Grown by Dc and RF Sputtering without Oxygen.” *Journal of Physics D: Applied Physics* 43 (5). https://doi.org/10.1088/0022-3727/43/5/055402.

Turkoglu, Fulya, Hasan Koseoglu, Ayten Cantas, Fatime G. Akca, Ece Meric, Dilara G. Buldu, Mehtap Ozdemir, Enver Tarhan, Lutfi Ozyuzer, and Gulnur Aygun. 2019. “Effect of Defects and Secondary Phases in Cu2ZnSnS4 Absorber Material on the Performance of Zn(O,S) Buffered Devices.” *Thin Solid Films*. https://doi.org/10.1016/j.tsf.2018.12.001.

Ul-Hamid, Anwar. 2020. “The Effect of Deposition Conditions on the Properties of Zr-Carbide, Zr-Nitride and Zr-Carbonitride Coatings – a Review.” *Materials Advances*. https://doi.org/10.1039/d0ma00232a.

Usseinov, A. B., E. A. Kotomin, A. T. Akilbekov, Yu F. Zhukovskii, and J. Purans. 2014. “Hydrogen Induced Metallization of ZnO (11Ì...00) Surface: Ab Initio Study.” In *Thin Solid Films*. https://doi.org/10.1016/j.tsf.2013.11.021.

Uvarov, Vladimir, and Inna Popov. 2013. “Metrological Characterization of X-Ray Diffraction Methods at Different Acquisition Geometries for Determination of Crystallite Size in Nano-Scale Materials.” *Materials Characterization*. https://doi.org/10.1016/j.matchar.2013.09.002.

Voutsas, G. P., A. G. Papazoglou, P. J. Rentzeperis, and D. Siapkas. 1985. “The Crystal Structure of Antimony Selenide, Sb2Se3.” *Zeitschrift Fur Kristallographie - New Crystal Structures*. https://doi.org/10.1524/zkri.1985.171.3-4.261.

Wang, Chong, Shuaicheng Lu, Sen Li, Siyu Wang, Xuetian Lin, Jun Zhang, Rokas Kondrotas, Kanghua Li, Chao Chen, and Jiang Tang. 2020. “Efficiency Improvement of Flexible Sb2Se3 Solar Cells with Non-Toxic Buffer Layer via Interface Engineering.” *Nano Energy* 71: 104577. https://doi.org/10.1016/j.nanoen.2020.104577.

Wang, Congcong, Shiyou Chen, Ji Hui Yang, Li Lang, Hong Jun Xiang, Xin Gao Gong, Aron Walsh, and Su Huai Wei. 2014. “Design of I2-II-IV-VI4 Semiconductors through Element Substitution: The Thermodynamic Stability Limit and Chemical Trend.” *Chemistry of Materials*. https://doi.org/10.1021/cm500598x.

Wang, Kejia, Byungha Shin, Kathleen B Reuter, Teodor Todorov, David B Mitzi, and Supratik Guha. 2011. “Structural and Elemental Characterization of High Efficiency Cu2ZnSnS4 Solar Cells Structural and Elemental Characterization of High Efficiency Cu 2 ZnSnS 4 Solar Cells.” *Citation: Appl. Phys. Lett. Appl. Phys. Lett. Additional Information on Appl. Phys. Lett. Journal Homepage*.

Wang, Liang, Deng Bing Li, Kanghua Li, Chao Chen, Hui Xiong Deng, Liang Gao, Yang Zhao, et al. 2017. “Stable 6%-Efficient Sb2Se3 Solar Cells with a ZnO Buffer Layer.” *Nature Energy*. https://doi.org/10.1038/nenergy.2017.46.

Wang, Wei, Mark T. Winkler, Oki Gunawan, Tayfun Gokmen, Teodor K. Todorov, Yu Zhu, and David B. Mitzi. 2014. “Device Characteristics of CZTSSe Thin-Film Solar Cells with 12.6% Efficiency.” *Advanced Energy Materials*. https://doi.org/10.1002/aenm.201301465.

Wen, Xixing, Chao Chen, Shuaicheng Lu, Kanghua Li, Rokas Kondrotas, Yang Zhao, Wenhao Chen, et al. 2018. “Vapor Transport Deposition of Antimony Selenide Thin Film Solar Cells with 7.6% Efficiency.” *Nature Communications*. https://doi.org/10.1038/s41467-018-04634-6.

Wen, Xixing, Zonghuan Lu, Gwo Ching Wang, Morris A. Washington, and Toh Ming Lu. 2021. “Efficient and Stable Flexible Sb2Se3 Thin Film Solar Cells Enabled by

an Epitaxial CdS Buffer Layer." *Nano Energy* 85 (February): 106019. https://doi.org/10.1016/j.nanoen.2021.106019.

Wenham, S. R., M. A. Green, M. E. Watt, R. P. Corkish, and A. B. Sproul. 2013. *Applied Photovoltaics, Third Edition*. *Applied Photovoltaics, Third Edition*. https://doi.org/10.4324/9781849776981.

Witte, Wolfram, Daniel Abou-Ras, and Dimitrios Hariskos. 2013. "Chemical Bath Deposition of Zn(O,S) and CdS Buffers: Influence of Cu(In,Ga)Se2 Grain Orientation." *Applied Physics Letters*. https://doi.org/10.1063/1.4788717.

Wohlmuth, Walter, and Ilesanmi Adesida. 2005. "Properties of R.F. Magnetron Sputtered Cadmium-Tin-Oxide and Indium-Tin-Oxide Thin Films." *Thin Solid Films*. https://doi.org/10.1016/j.tsf.2004.11.186.

Yazici, Sebnem, Mehmet Ali Olgar, Fatime Gulsah Akca, Ayten Cantas, Metin Kurt, Gulnur Aygun, Enver Tarhan, Ekrem Yanmaz, and Lutfi Ozyuzer. 2015. "Growth of Cu2ZnSnS4 Absorber Layer on Flexible Metallic Substrates for Thin Film Solar Cell Applications." *Thin Solid Films*. https://doi.org/10.1016/j.tsf.2015.06.028.

Yoo, Young Zo, Zheng Wu Jin, T. Chikyow, T. Fukumura, M. Kawasaki, and H. Koinuma. 2002. "S Doping in ZnO Film by Supplying ZnS Species with Pulsed-Laser-Deposition Method." *Applied Physics Letters*. https://doi.org/10.1063/1.1521577.

Yousfi, El Bekkaye, Jacques Fouache, and Daniel Lincot. 2000. "Study of Atomic Layer Epitaxy of Zinc Oxide by In-Situ Quartz Crystal Microgravimetry." *Applied Surface Science*. https://doi.org/10.1016/S0169-4332(99)00330-X.

Yu, Hak Ki, and Jong Lam Lee. 2014. "Effect of Ion Beam Assisted Deposition on the Growth of Indium Tin Oxide (ITO) Nanowires." *CrystEngComm*. https://doi.org/10.1039/c4ce00237g.

Yuan, Chenchen, Xin Jin, Guoshun Jiang, Weifeng Liu, and Changfei Zhu. 2016. "Sb2Se3 Solar Cells Prepared with Selenized Dc-Sputtered Metallic Precursors." *Journal of Materials Science: Materials in Electronics*. https://doi.org/10.1007/s10854-016-4917-3.

Yuan, Chenchen, Lijian Zhang, Weifeng Liu, and Changfei Zhu. 2016. “Rapid Thermal Process to Fabricate Sb2Se3 Thin Film for Solar Cell Application.” *Solar Energy*. https://doi.org/10.1016/j.solener.2016.08.020.

Zeng, Kai, Ding Jiang Xue, and Jiang Tang. 2016. “Antimony Selenide Thin-Film Solar Cells.” *Semiconductor Science and Technology*. https://doi.org/10.1088/0268-1242/31/6/063001.

Zhang, Chong, Zhiqiang Li, Yuting Guo, Xiaona Niu, Xiaoyang Liang, Dong Zhou, Hongbing Zhu, Jingwei Chen, and Yaohua Mai. 2017. “Controllable Synthesis and Properties of Sb2Se3 Nanorods Synthesized by Hot-Injection Method.” *Journal of Nanoscience and Nanotechnology*. https://doi.org/10.1166/jnn.2017.12770.

Zhang, Jianwang, Weitao Lian, Yiwei Yin, Xiaomin Wang, Rongfeng Tang, Chen Qian, Xiaojing Hao, Changfei Zhu, and Tao Chen. 2020. “All Antimony Chalcogenide Tandem Solar Cell.” *Solar RRL*. https://doi.org/10.1002/solr.202000048.

Zhang, Zaoli, Lin Guo, and Wendong Wang. 2001. “Synthesis and Characterization of Antimony Oxide Nanoparticles.” *Journal of Materials Research*. https://doi.org/10.1557/JMR.2001.0096.

Zhao, Yanyuan, Kun Ting Eddie Chua, Chee Kwan Gan, Jun Zhang, Bo Peng, Zeping Peng, and Qihua Xiong. 2011. “Phonons in Bi2S3 Nanostructures: Raman Scattering and First-Principles Studies.” *Physical Review B - Condensed Matter and Materials Physics*. https://doi.org/10.1103/PhysRevB.84.205330.

Zhao, Yun, Le Chang, Xiao Fei Dong, Hui Xia Zhang, Yan Li, and Jian Biao Chen. 2020. “Effect of Ag Doping on the Performance of Cu2SnS3 Thin-Film Solar Cells.” *Solar Energy*. https://doi.org/10.1016/j.solener.2020.03.006.

Zhou, Ying, Meiying Leng, Zhe Xia, Jie Zhong, Huaibing Song, Xinsheng Liu, Bo Yang, et al. 2014. “Solution-Processed Antimony Selenide Heterojunction Solar Cells.” *Advanced Energy Materials*. https://doi.org/10.1002/aenm.201301846.

Zhou, Ying, Liang Wang, Shiyou Chen, Sikai Qin, Xinsheng Liu, Jie Chen, Ding Jiang Xue, et al. 2015. “Thin-Film Sb2Se3 Photovoltaics with Oriented One-Dimensional Ribbons and Benign Grain Boundaries.” *Nature Photonics*.

https://doi.org/10.1038/nphoton.2015.78.

Zhu, Xinghua, Qingshuang Xie, H. Tian, Ming Zhang, Zongyan Gou, S. He, Peng Gu, Haihua Wu, J. Li, and Dingyu Yang. 2019. “High Photoresponse Sensitivity of Lithium-Doped ZnO (LZO) Thin Films for Weak Ultraviolet Signal Photodetector.” *Journal of Alloys and Compounds*. https://doi.org/10.1016/j.jallcom.2019.07.074.

Zimmermann, Uwe, Marta Ruth, and Marika Edoff. 2006. “Cadmium-Free CIGS Min-Modules with ALD-Grown Zn(O,S)-Based Buffer Layers.” In *21st European Photovoltaic Solar Energy Conference*.